Luminescent Light Harvesting Metal-Organic Molecular Complex and Extended Frameworks for Colour Tunability and Sensing Applications

A Thesis Submitted for the Degree of

Master of Science

as a part of the

Integrated Ph.D. Programme

(Chemical Science)

by

Komal Prasad

New Chemistry Unit (NCU)

Jawaharlal Nehru Centre for Advanced Scientific Research

(A Deemed University)

Bangalore – 560064

Dedicated

to

My Family

DECLARATION

I hereby declare that the matter embodied in the thesis entitled "**Luminescent Light Harvesting Metal-Organic Molecular Complex and Extended Frameworks for Colour Tunability and Sensing Applications**" is the result of investigations carried out by me at the New Chemistry Unit, Jawaharlal Nehru Centre for Advanced Scientific Research, India under the supervision of Prof. Tapas Kumar Maji and that it has not been submitted elsewhere for the award of any degree or diploma.

In keeping with the general practice in reporting the scientific observations, due acknowledgement has been made whenever the work described is based on the findings of other investigators. Any omission that might have occurred due to oversight or error in judgement is regretted.

Komal Prasad

CERTIFICATE

I hereby certify that the work described in this thesis entitled "**Luminescent Light Harvesting Metal-Organic Molecular Complex and Extended Frameworks for Colour Tunability and Sensing Applications**" has been carried out by Komal Prasad under my supervision at the New Chemistry Unit, Jawaharlal Nehru Centre for Advanced Scientific Research, India and that it has not been submitted elsewhere for the award of any degree or diploma.

Prof. Tapas Kumar Maji

JNCASR

(Research Supervisor)

D

ACKNOWLEDGEMENTS

I would like to express my deep gratitude to my research supervisor, Prof. Tapas Kumar Maji, for his patient guidance, enthusiastic encouragement, invaluable suggestions and useful criticism throughout the course of investigations. I am also grateful to him for allowing me to work on my own area of interest.

I am grateful to Prof. C. N. R. Rao, FRS who has always been a constant source of inspiration, with all his extraordinary enthusiasm and energy. It is really a great opportunity to be in the same institute and listen to his wonderful motivating speeches.

I sincerely thank Dr. Ranjani Viswanatha and Mr. Avijit Saha for fluorescence lifetime measurements.

I acknowledge the chairman of NCU (Prof. C. N. R. Rao) for allowing me to use the facilities of the centre.

I extend my thanks to the faculty members of JNCASR and Indian Institute of Science (IISc) for the wonderful courses as it was great pleasure learning new things. It was beneficial for my research investigations also. In particular, I would like to thank Prof. S. Balasubramanian, Prof. H. Ila, Prof. Aloknath Chakraborty, Prof. M. Eswaramoorthy, Prof. Tapas Kumar Maji, Dr. Jayanta Haldar, Dr. Sridhar Rajaram, Dr. Subi Jacob George, Prof. A. Sunderesan, Dr. T. Govindaraju, Dr. Ranjani Viswanatha, Prof. Chandrabhas Narayana, Dr. Sebastian C. Peter and Dr. Ujjal Gautam for their courses.

I wish to acknowledge the help provided by the technical staffs namely Mr. Anil, Mr. Vasu, Mr. Mahesh, Mr. Srinivas, Mr. Shiva and Mrs. Bhavya during various experiments.

I thank JNCASR Library, Complab, Hostel, Health Centre, Academics and Administration staff for providing and maintaining all the wonderful facilities.

I am grateful to my labmates Mr. Ritesh Haldar, Mr. Arpan Hazra, Ms. Anindita Chakraborty, Mr. Venkata Suresh, Ms. Nivedita Sikdar, Mr. Syamantak Roy, Ms. Papri Sutar, Ms. Sohini Bhattacharyya and past labmates Dr. Prakash Kanoo, Dr. Sudip Mohapatra and Dr. Kolleboyina Jayaramulu.

With great joy I thank all the Integrated Ph. D. students of CPMU and NCU. It has been really nice and a lot of fun to be part of the Integrated Ph. D. family. My sincere thanks to all my seniors, for sharing their knowledge with me and being very friendly.I sincerely acknowledge my batchmates for the wonderful times we have had in the past 3 years. I am thankful to all my juniors for being really nice.

I am honoured to thank all my school and college teachers for building my academic career at initial stage and also nourish the moral character.

My family has been the greatest strength for me. Words are indeed insufficient to thank my parents and my brother, who have always been very supportive. I always have been fortunate enough to have my family with me with all their care and love.

Last but not the least, I thank God almighty for providing me a truly blessed life.

PREFACE

This thesis consists of five chapters which describes design and luminescent properties of some supramolecular coordination frameworks manifesting their various applications.

Chapter 1 gives a brief overview of coordination polymers including their classification, development and applications. Importance of non-covalent interactions is discussed through supramolecular coordination polymers. Applications related to luminescent coordination polymers are discussed in detail.

Chapter 2 describes the crystal engineering approach for the construction of a porous luminescent 3D supramolecular framework from a 2D supramolecular structure. This is done through addition of an aromatic linker to the 2D structure which manipulated the structure. This 3D framework shows bright pyrene excimer emission which can be exploited for light harvesting application through dye inclusion.

Chapter 3 deals with the RGB (red-green-blue) concept of white light emission. Two new isomorphous flexible supramolecular Eu^{3+} and Tb^{3+} based 3D frameworks, $\{[Eu(L)(DMF)(H_2O)]\cdot 3H_2O\}_n$ (**1**) and $\{[Tb(L)(DMF)(H_2O)]\cdot 3H_2O\}_n$ (**2**) are synthesized using a tricarboxylic acid linker H_3L (4,4′,4″-[1,3,5-phenyl-tri(methoxy)]-tris-benzoic acid) having blue emission. They are porous and shows selective adsorption of CO_2 over CH_4 at 195 K. Mixing of Tb^{3+} and Eu^{3+} in $\{[Tb_{1-x}Eu_x(L)(DMF)(H_2O)]\cdot 3H_2O\}_n$ in different stoichiometric ratio shows different emission colours (green, pink, orange, red). It is also shown that proper mixing can lead to white light emission.

Chapter 4 outlines colour tuning in two novel isomorphous 3D supramolecular structures through dye inclusion in different percentages. $\{[Zn(bpdc)(bpy)]\cdot DMF\}_n$ (**1**) and $\{[Zn(bpdc)(o\text{-phen})]\cdot DMF\}_n$ (**2**) (bpdc = biphenyl-4,4′-dicarboxylic acid ; bpy = 2,2′-bipyridine ; *o*-phen = ortho-phenanthroline) are synthesized with biphenyl luminescent core. Partial energy transfer process is observed from framework (donor) to the included dye (acceptor) and hence emission colours are tuned.

Chapter 5 introduces a new tetrameric complex, $\{[Zn_4(adc)_3(bpz)_6(NO_3)_2]\cdot 2H_2O\}$ (**1**) (bpz = bipyridophenazine; adc = anthracene dicarboxylic acid). It forms a 3D supramolecular

framework through π···π and C-H···π interactions. Anthracene:bpz exciplex formation leads to bright red emission from the complex. Efficient energy transfer phenomenon is observed between anthracene (donor) and exciplex (acceptor) formed. This complex shows blue shifted cyan emission in presence of very low concentration of Al^{3+} (10 nM) but does not show any change for other metal ions. Hence this molecular complex can be used for the ratiometric detection of biologically toxic Al^{3+}.

Table of Contents

Chapter: 1

Introduction

1.1 Coordination Polymers (CPs): An Overview

The phrase, "coordination polymers" appeared in early 1960's. Infinitely extended coordination compounds with backbones constructed from metal ions as connectors and organic ligands as linkers are called "coordination polymers". These polymers can extend in one, two or three dimensions and can be porous. The three dimensional polymers are also known as Metal-organic frameworks (MOFs). In the past decade, there is a rapid growth in the research of coordination polymers because of its easy tailorability and wide applications.[1] Due to the presence of inorganic part this material shows high thermal and mechanical stability like zeolites. On the other hand organic linkers provide structural tunability based on different network topologies and functionalities by modifying size, shape and functional groups.[2]

Transition metal ions are widely used as connectors and depending upon their oxidation state and coordination number they give rise to various structures. The geometries formed by them include linear, T- or Y-shaped, tetrahedral, square-planar, square pyramidal, trigonal-bipyramidal, octahedral, trigonal-prismatic, pentagonal-bipyramidal and their distorted forms (Figure 1). The geometries formed also depend on reaction conditions, solvents, counter anions and organic ligands.[3] Other than transition metal ion; lanthanide ions (rare earth elements) also act as connectors and provide comparatively large coordination number from 7 to 10 to give new and unusual network topologies.[4] In some cases, metalloligand connectors are also used to construct CPs.[5a-5b] Metal-porphyrin connectors are the most well-known among them and these provide functionally and topologically versatile structures.[5c-5e]

Different types of functionalized ligands offer a wide variety of linking sites with different binding strength and directionality (Figure 1). Halides (F, Cl, Br and I) are the smallest and simplest of all linkers which are inorganic ligands.[6] Bridging ability of CN^- and SCN^- is similar to halide linkers. Other types of linker include neutral, anionic and cationic organic ligands. Cyanometallate anions show various geometries which include linear, as in $[M(CN)_2]^-$ (M=Au and Ag), trigonal, as in $[Cu(CN)_3]^{2-}$, tetrahedral, as in $[Cd(CN)_4]^{2-}$, square planar, as in $[M(CN)_4]^{2-}$, (M=Ni, Pd, and Pt), octahedral, as in $[M(CN)_6]^{3-}$(M=Fe, Co, Cr, and Mn), and pentagonal bipyramidal, as in $[Mo(CN)_7]^{4-}$.[7] The octacyanometallates $[M(CN)_8]^{n-}$ (M=Mo and W) show various coordination geometries like square-antiprism, dodecahedron, or bicapped trigonal-prism. Di/tri or tetra-carboxylic acid based linkers are most well studied anionic linkers in PCPs.[8] Terepthalic

acid, a ditopic anionic linker is used for MOF-5 and extending this linker length several isoreticular PCPs have been reported. Pyrazine, 4,4′-bipyridine and other bipyridyl analogues are the most commonly used ditopic neutral organic ligands.[9] Conformation can also be widely varied by keeping similar coordinating sites (e.g. pyridine) and varying the linker length. A list of all varieties of linkers used in CPs is listed in figure 2.

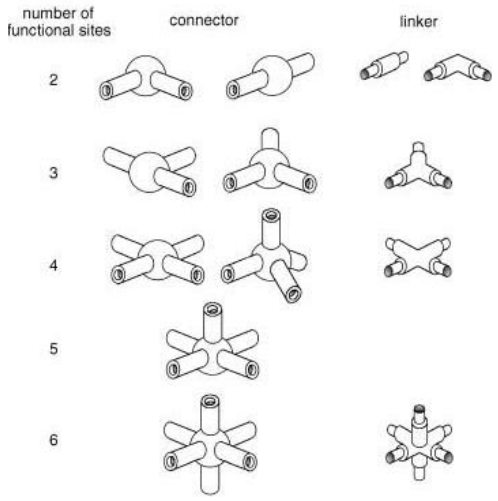

Figure 1: Components of coordination polymers with different number of functional sites. This figure has been reproduced with permission from reference no. 1e.

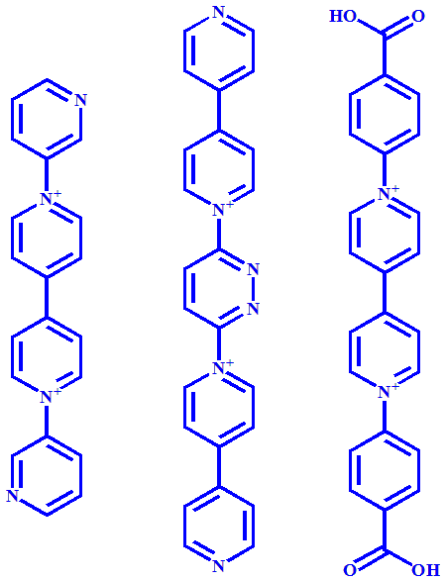

Cationic organic ligands

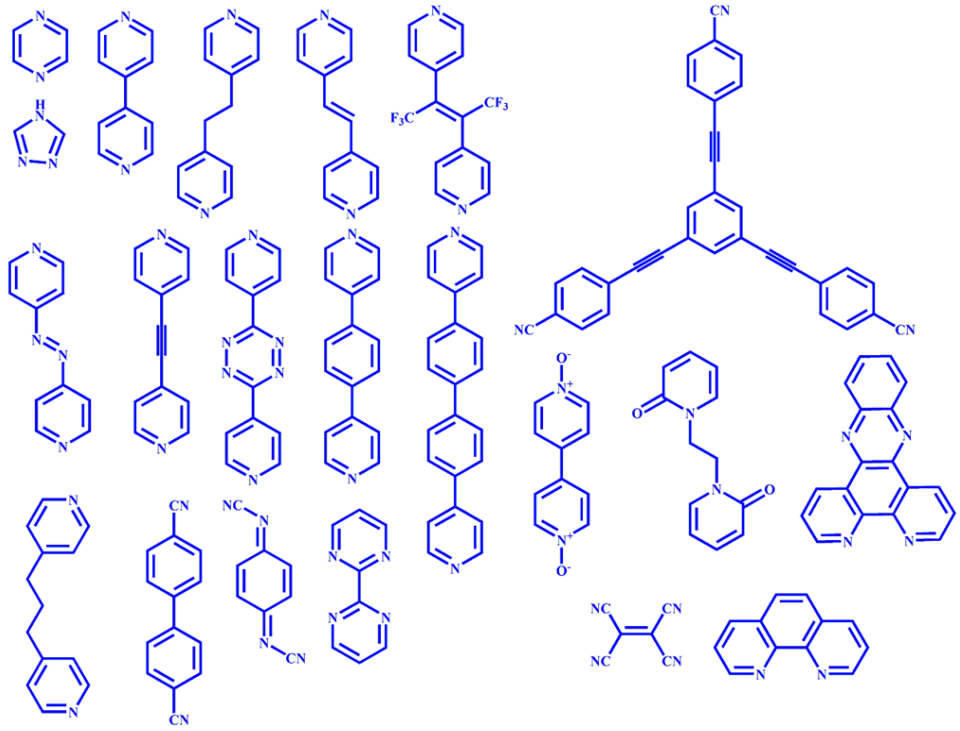

Neutral organic ligands

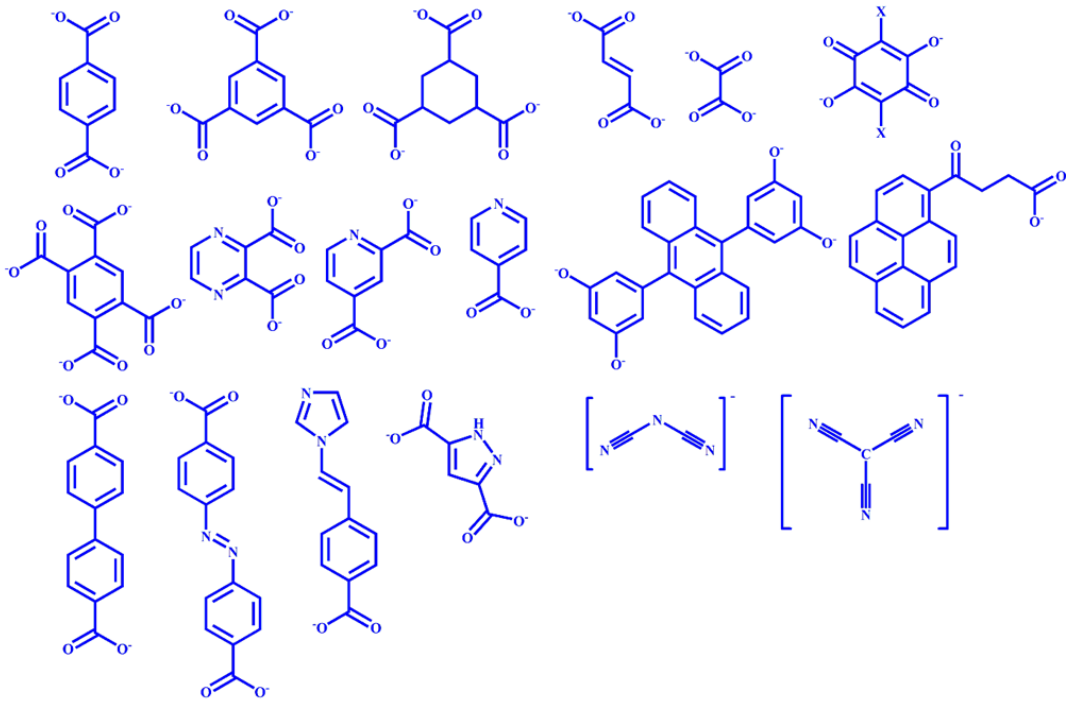

Anionic organic ligands

Figure 2: List of cationic, neutral and anionic linkers used for construction of coordination polymers.

Apart from simple metal connectors and metalloligand, *in situ* generated metal-oxygen clusters, also known as secondary building unit (SBU) can direct the final structure.[10a] Depending upon the reaction conditions, ligand functionality and metal ion, various kind of SBUs can be obtained. Paddle-wheel, $Zn_4(O)(COO)_6$, μ-oxo-bridged and trinuclear SBUs are most common among several SBUs reported so far in PCPs.[10b] Figure 3 shows all such possible inorganic SBUs that are reported till date in MOFs.

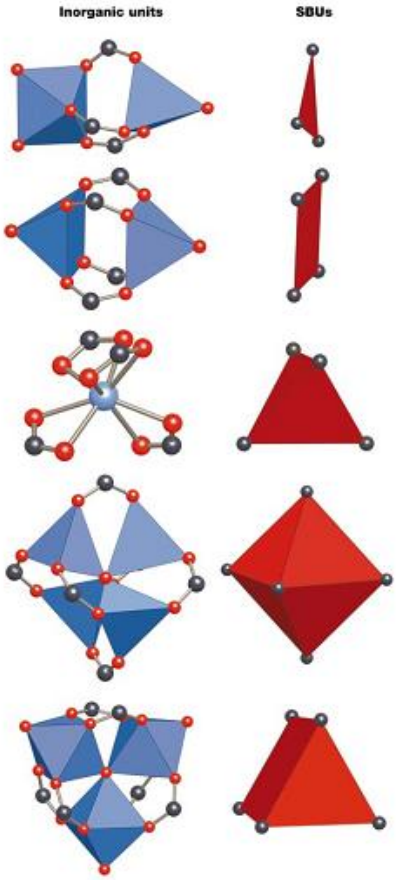

Figure 3: Examples of SBUs from carboxylate PCPs. O, red; N, green; C, black. In inorganic units metal-oxygen polyhedra are blue, and the polygon or polyhedron defined by carboxylate carbon atoms (SBUs) are red. This figure has been reproduced with permission from reference no. 14a.

1.2 Classification and Developments of PCPs

In 1998, porous coordination compounds were classified in three categories by Kitagawa *et. al.* (Figure 4).[11] The first generation compounds include microporous frameworks, which are sustained only with guest molecules and show irreversible framework collapse upon removal of guest molecules. The collapse occurs due to the

force of close packing. The second generation compounds have stable and robust frameworks, which show permanent porosity even after the removal of guest molecule. Prediction of properties of a rigid framework is easier as compared to a flexible one. They are highly periodic with open channels, welcoming a wide range of guest molecules and sometime, due to their rigid nature they are not selective. Second generation compounds can show properties like anion exchange, catalysis, gas adsorption *etc*.[12] The third generation compounds have flexible and dynamic frameworks, which respond to external stimuli, such as light, electric field, guest molecules, and change their channels or pores reversibly. Third generation compounds show typical sorption behaviour which include selective, stepwise and hysteretic adsorption. Flexibility can be combined with functional surface for an effective selectivity facilitating gas separation. This generation compounds have properties for various potential applications such as gas storage, separation, sensing, and drug delivery *etc*.[13]

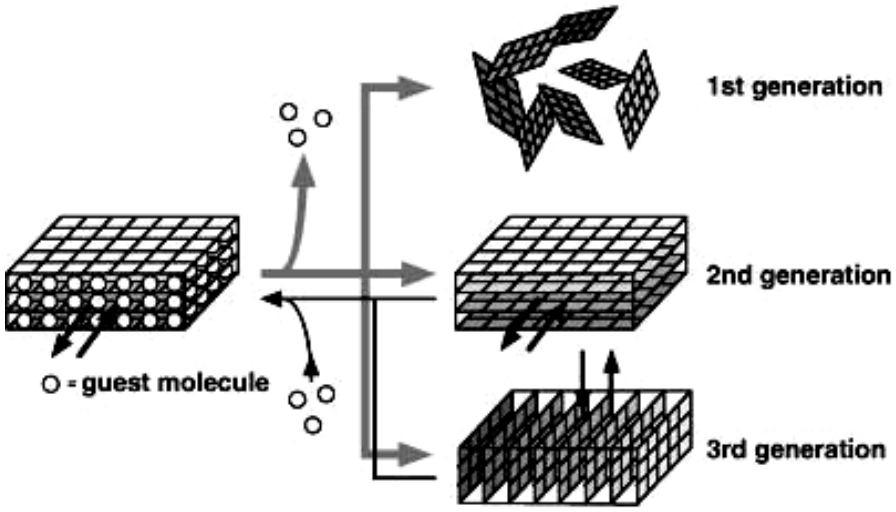

Figure 4: Classification of porous coordination polymers (PCPs). This figure has been reproduced with permission from reference no. 1e.

The earliest most famous examples of PCPs are IRMOF (Iso-Reticular Metal-organic framework) series,[14a-14c] HKUST (Hong Kong University of Science and Technology),[14d] ZIFs (Zeolitic Imidazolate Frameworks)[14e-14f] and MILs (Materials of Institut Lavoisier).[14g-14h] Synthesis of PCPs using reticular chemistry has been a very well accepted method and thus highly periodic IRMOFs with enhanced porosity were obtained. Among IRMOFs MOF-5 has been the most well studied one.[14a]

$\{Zn_4(O)(COO)_6\}$ SBUs are linked by the benzene dicarboxylate (BDC) linker and form a periodic cubic framework of MOF-5. It has exceptional porosity, with Langmuir surface area of 3000 m^2g^{-1}. ZIF, another class of PCP, contains Zn(II) or Co(II) metal ions in combination with imidazolate or functionalized imidazolate anions.[14e] These exhibit permanent porosity and high thermal and chemical stability, which make them useful for various applications such as the capture of CO_2 and its selective separation from industrially relevant gas mixtures. For example, Yaghi *et. al.* studied selective carbon dioxide capture properties of isoreticular ZIFs. The high stability of ZIFs has enabled them to show organic transformations on its crystals and yet its topology, crystallinity and porosity remain intact throughout the process. Crystalline ZIF-9 was used as an efficient heterogeneous catalyst for the Knoevenagel catalysis between benzaldehyde and malononitrile to form benzylidene malononitrile as the principal product.[14f] Another very well-known porous framework is HKUST-1, $[Cu_3(btc)_2(H_2O)_3]$ which was first reported by Williams and co-workers and then studied by numerous research groups. It is composed of $\{Cu_2(CO_2)_4\}$ paddlewheel SBU linked by benzene-1,3,5-tricarboxylate and has very large cavities with window diameter of ~ 6 Å. The most interesting feature of this material is the presence of unsaturated metal sites (UMSs) in the walls of the material after desolvation. Most of the studies are focussed on its gas adsorption properties because of its high surface area along with the capability of gas separation and catalysis. MIL PCPs, extensively studied by Férey's group, are examples of PCPs that exhibit global flexibility i.e. shows breathing behaviour (third generation PCPs). PCPs consisting of pillared layer structures have also been widely studied as a route to get rationally designed architectures. Simple modification of the pillars can control size and shape of the channel. Even the chemical functionality of the material can be tuned.

1.3 Supramolecular Frameworks: Importance of Non-covalent Interactions

Supramolecular interactions such as C-H$\cdots\pi$, $\pi\cdots\pi$ or hydrogen bonding interactions are imperative in crystal engineering approach. These interactions are primarily observed in organic co-crystals and also play very crucial role in organic self-assembly.[15] Aromatic organic ligands in lower (0D or 1D) compounds through directional non-covalent interactions (like H-bonding, $\pi\cdots\pi$ interactions) can form highly ordered higher dimensional (2D or 3D) supramolecular framework with potential applications in molecular recognition, gas storage and catalysis. As the super-structure is built by the

non-covalent interactions, such supramolecular frameworks would be much more dynamic and flexible compared to the framework shaped solely by covalent bonds.

In some cases, due to the ligand characteristics (monotopic, pendent -OH/-COOH/-SO_3H/-NH_2 groups, large aromatic π surface *etc*) the coordination network does not grow in 3D rather restricts to 1D or 2D form.[16] Presence of the hydrogen bonding sites or possibility of C-H···π or π···π interactions lead the structure to higher dimensionalities. Figure 5 shows possible pathways of non-covalent interactions in CPs.

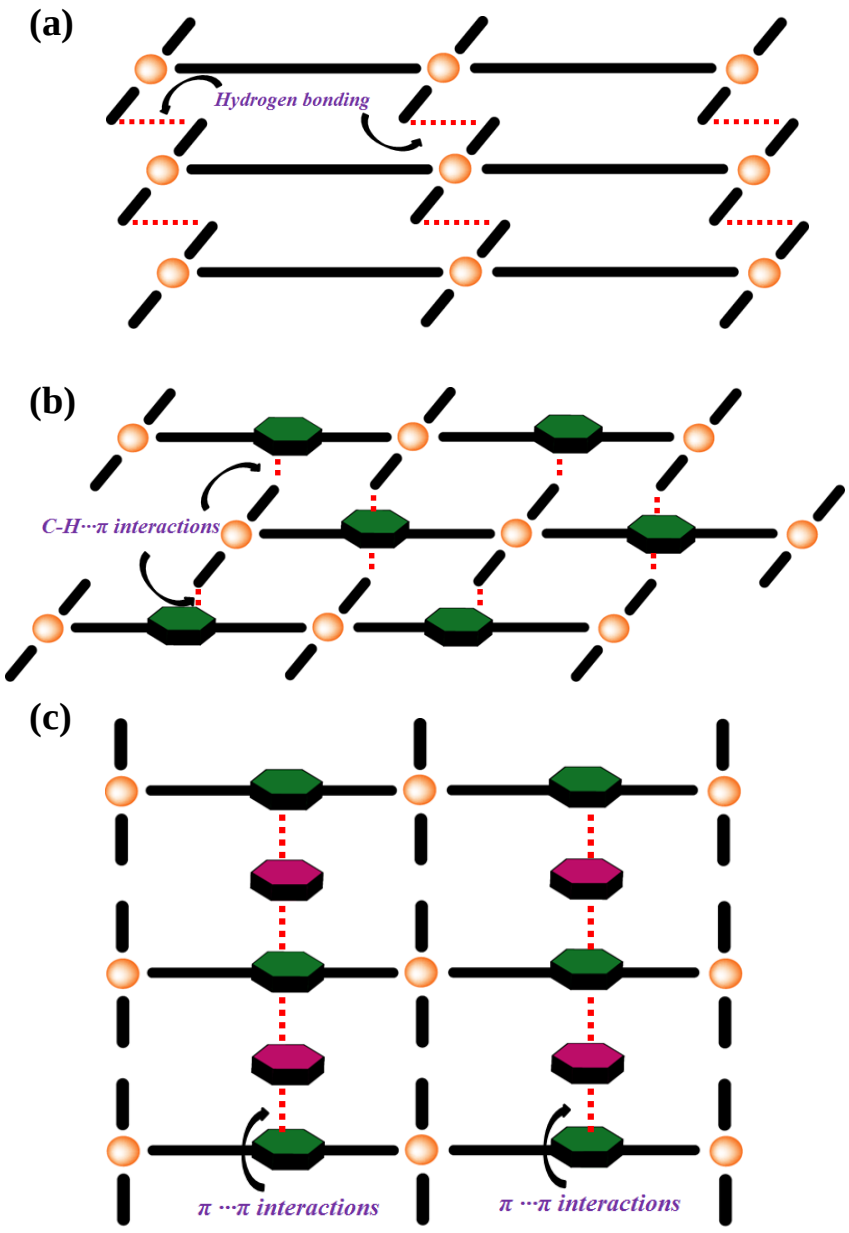

Figure 5: Schematic of possible modes of non-covalent interactions in 1D or 2D CPs.

As anticipated, these non-covalent interactions do not give sufficient thermal stability which can be obtained by coordination bonds/covalent bonds. But presence of these supramolecular interactions can originate porosity, structural flexibility and interesting photophysical properties. For example, Maji *et. al.* have reported five supramolecular PCPs (MOCPs), $\{[Ni(bipy)(H_2O)_4](2,6\text{-nds})_3\cdot 4H_2O\}$, $\{[Ni(bipy)(H_2O)_4](2,6\text{-nds})_3\cdot 2H_2O\}$, $\{[Ni(bipy)(H_2O)_4](2,6\text{-nds})\}$, $\{[Ni(bipy)(H_2O)_4](2,6\text{-nds})\}$, $\{[Cu(bipy)(H_2O)_4](2,6\text{-nds})\}$ (bipy=4,4′-bipyridine; 2,6-nds=2,6-naphthalenedisulphonate) and characterized them.[17a] $[M(bipy)(H_2O)_4]^{2+}$ is the basic building unit for all the MOCPs and 2,6-nds act as a counter anion. 2,6-nds interact with water and bipy molecules through strong hydrogen-bonding and π···π interactions to form 3D supramolecular structures. Zaworotko *et. al.* have synthesized Zn(II)-4,4′-bipyridine (Zn-bipy) based frameworks containing pyrene intercalated between adjacent layers and aromatic solvent molecules incorporated within the framework cavities.[17b] The type of structure obtained depends on the nature of the enclathrated solvent molecule. 1-D ladder architecture was obtained in the case of benzene, toluene, *p*-xylene and chlorobenzene whereas *o*-dichlorobenzene gives 2D square grid architecture. The photophysical properties of these coordination polymers were also studied. Same group have reported a coordination polymer $\{[Zn(bipy)_{1.5}(NO_3)_2]\cdot 0.5pyrene\cdot MeOH\}_n$, which contains T-shaped Zn^{2+} nodes and, 4,4′-bipyridine and pyrene as organic components.[17c] Here, pyrene molecules are intercalated between 4,4′-bipyridine forming 2:1 bipy:pyrene exciplex through π···π interactions. In another example, Zeng *et. al.* reported two supramolecular coordination polymers, $[HgI_2\ (L^1)\cdot 0.5H_2O]_\infty$ (**1**) and $[HgI_2(L^2)\cdot 0.4CH_3OH]_\infty$ (**2**) (L^1 = bis[4-(4-pyridylmethyleneamino)phenyl]ether) and L^2 = *N*,*N*′-bis(3-pyridylmethyl)-diphthalicdiimide).[17d] **1** forms an interestingly infinite cross-linked double helical structure through weak hydrogen bonding (C–H···I), whereas the other forms the one-dimensional *zigzag* chains, which are parallel with each other. Different structures can be attributed to the flexibility of ligands. Helical structures have always received attention in coordination chemistry because helicity is an essential element of life and is also important in various applications such as asymmetric catalysis and optical devices. Five neutral infinite Cu(II) dicarboxylate coordination polymers, $[Cu(ipa)(2,2'\text{-bpy})]_n\cdot 2nH_2O$, $[Cu_2(ipa)_2(phen)_2H_2O]_n$, $[Cu(oba)(phen)]_n$, $[Cu(oba)(2,2'\text{-bpy})]_n$ and $[Cu(eoba)(phen)]_n$ was synthesized using three V-shaped dicarboxylates (isophthalate (ipa), 4,4′-oxybis(benzoate) (oba) and ethylenedi(4-oxybenzoate) (eoba))

and aromatic chelating ligands.[17e] The bridging ligation of the simple V-shaped dicarboxylate ligands lead to helical chain structures. And interestingly, these helical chains are paired through π···π stacking and hydrogen bonding interactions into double-stranded helices or molecular zippers.

1.4 Applications of CPs

1.4.1 Gas Storage and Separation, Catalysis, Magnetism and Drug Delivery

One of the most extensively studied properties of PCPs is gas adsorption. Their large internal surface area, modular nature, tunable structures make them good candidates for gas adsorption and separation. The confined nano channels of PCPs can accommodate the guest molecules in high concentration. Till date there are many PCPs that have reported very high surface area compared to the other contemporaries. The highest surface area reported in PCPs till date is 7140 m^2g^{-1} for NU-110 (NU- North Western University).[18a] Other landmark examples in this respect are MOF-177 (surface area, 5640 m^2g^{-1}), MIL-101 (surface area, 5900 m^2g^{-1}), UMCM-2 (surface area, 6000 m^2g^{-1}) and MOF-210 (surface area, 6240 m^2g^{-1}).[18b-18e] PCPs are potential candidates as H_2, CH_4 and C_2H_2 storage materials. For example, mesoporous NU-110 reported by Hupp *et. al*. shows hydrogen storage capacity of 9.05 wt% at 77 K and 56 bar.[19a] PCN-14, reported by Zhou *et. al.*, shows a methane uptake of 230 v/v STP at 290 K and 35 bar, which is 28 % higher than the DOE target and highest value reported till date.[19b] For acetylene storage, Co_2(DHTP) was found to exhibit an uptake of 230 cm^3 (STP)/cm^3 at 298 K, 1 atm.[19c]

Other than storage of gases, sequestration of CO_2, a greenhouse gas is another aspect of PCP research. The rising level of atmospheric carbon dioxide from anthropogenic emissions is one of the greatest environmental threats of today. Carbon capture and sequestration (CCS) is the requirement of present scenario. The CCS process involves the selective removal of CO_2 from gas mixture, the compression of pure CO_2 to a supercritical fluid, transportation to an injection site, and finally permanent subterranean or submarine storage. Development of solid adsorbents that can selectively adsorb CO_2 at partial pressures applicable to CCS is the area of significant interest. MOFs are highly tunable which offer greater functionality and has reduced adsorbent mass and volume compared to traditional solid adsorbents. For example, at 35 bar, the volumetric CO_2 adsorption capacity for MOF-177 (Langmuir surface area, 5640 m^2g^{-1}) reaches a storage

density of 320 cm^3 (STP)g^{-1}.[20a] It is approximately 9 times higher than the quantity stored at this pressure in a container without the MOF and also higher than conventional materials, namely, zeolite 13X and MAXSORB. But at low pressure (1 atm) Mg-MOF-74 shows highest storage capacity of 27.5 wt% at 298 K.[20b]

Heterogeneous catalysts have an advantage of easy recoverability and hence they are important for industrial applications. Because of the presence of well defined pores and channels which can be easily functionalized PCPs have the potential for size and shape selective heterogeneous catalysis. Their porosity provides internal surface areas that are relatively large, thereby facilitating their catalytic reactivity and the uniformity of their pore and channel sizes account catalytic selectivity. They are robust because of the presence of inorganic part and are therefore well suited for catalysis under extreme conditions. Among the earliest reports of PCP-based catalysis, in 1994 Fujita and co-workers worked on the cyanosilylation of aldehydes by a 2D PCP (layered square grids) of formula $Cd(4,4'\text{-bpy})_2(NO_3)_2$, (bpy = 4,4′-bipyridine).[21a] This work was mainly on size and shape selective clathration. The porous-framework material $[Cu_3(btc)_2(H_2O)_3]$, also known as HKUST-110 and as MOF-199,[21b] contains large cavities having pore dimensions of diameter ~ 6 Å . The Cu^{2+} possesses open sites after the removal of water molecules coordinated to it. Kaskel and co-workers have showed that these Lewis acid sites could catalyze the cyanosilylation of benzaldehyde or acetone.[21c] The anhydrous version of HKUST-1 behaves as an acid catalyst was shown by Alaerts *et. al.*[21d]

Incorporation of magnetic moment carriers such as paramagnetic metals or open shell organic ligands or both can impart magnetic properties in PCPs. Since magnetism is a cooperative phenomenon, some kind of exchange between the moment carriers is required for material to be magnetic. Introduction of magnetic guests in the framework also convey magnetism to PCPs. From zero to three dimensions, all sorts of CPs have been exploited for magnetic studies.[22]

Better techniques of drug administration are always in demand and continuous efforts are being applied by researchers to fulfil the growing demands. PCPs are hybrid materials which combine advantage of organic groups with the inorganic elements to get ordered framework with greater porosity for high drug loading capacity and controlled release. By employing different functional groups in the PCPs, the functionality of the framework and pore size can be tuned to suite different applications. Hence, PCPs show great hope for the development of new therapeutic and diagnostic applications. MIL-88A,

MIL-88B_4CH_3 and MIL-100 passed toxicological studies in rats (upto 220 $mgkg^{-1}$) both in vitro and in vivo. They are iron carboxylate based PCPs.[23a] M-CPO-27 or MIL 100 have shown their dissolution and persistence under simulated physiological conditions (eg. Phosphate buffered saline, PBS and bovine serum albumin, BSA) for days to upto three weeks depending on the structure, composition, particle size and formulation.[23b] Another example of drug delivery by PCP is demonstrated by the cationic zinc adeninate PCP for the administration of procainamide (a cationic drug).[23c]

1.4.2 Luminescence: Molecular Sensing, Tunable Emission and Light Harvesting

PCPs are very attractive material for applications in molecular sensing, modular emission characteristic and other optical properties. Primary criterion for such application is to obtain luminescence in PCP structure. The possible approaches to obtain luminescence in PCPs are as following:

a) **Metal-based luminescence**: Lanthanide ions (Eu, Tb, Sm *etc*) can be used as nodes

b) **Ligand based emission**: Linkers with luminescent cores (pyrene, anthracene, naphthalene); MLCT (metal-to-ligand charge transfer) or LMCT (ligand-to-metal charge transfer)

c) **Exciplex or excimer emission**: Presence of donor/acceptor pairs in the structure might lead to red shifted bright emission characteristic

d) **Guest induced emission**: Inclusion of luminescent guest molecules such as pyrene, perylene, anthracene *etc*

In presence of any of the above mentioned possibilities PCPs can show emission characteristics and these features can be exploited for versatile applications as discussed in the next sections.

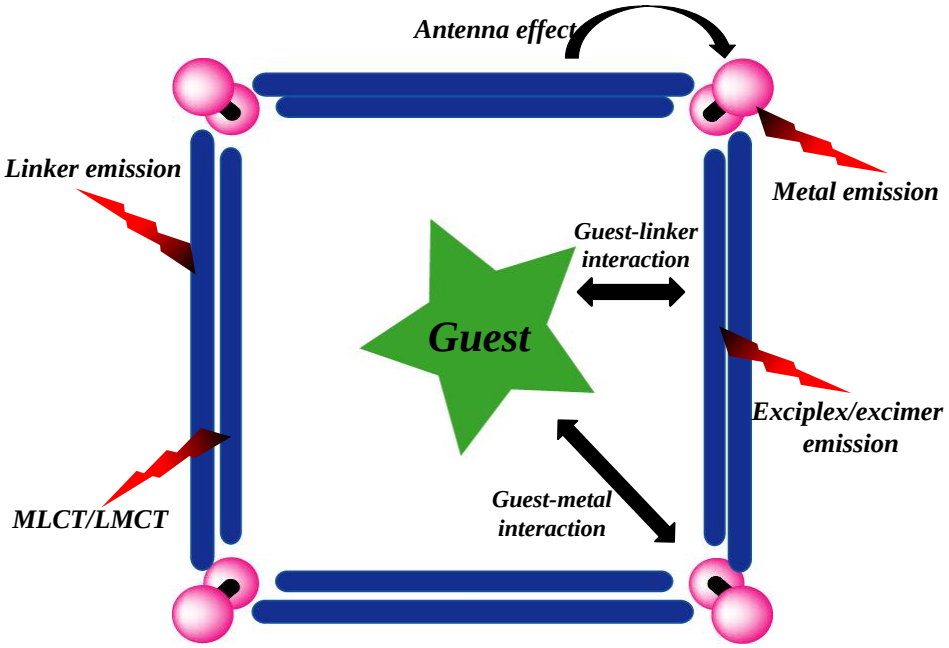

Figure 6: Possible luminescence pathways in a PCP.

1.4.2.1 Molecular Sensing

A sensor is a material that shows a significant change in electrical, electronic, magnetic or optical signal when it binds to a specific guest chemically or interacts physically. Any sensing material should possess following characteristics:

- It should exhibit some change in response to an interaction with the analyte
- The change should have some analyte specificity
- It is desirable that the response should be reversible
- The change in response to the analyte should be detectable

Molecular recognition or sensing is generally based on weak interactions between receptors and substrates. There has been extensive research on designing synthetic receptors to meet the challenge of selective recognition of specific molecules. PCPs are ideal for molecular recognition due to its porous nature and high degree of structural tunability. Due to a defined pore size and shape, selective recognition is viable; further according to the analyte nature PCPs can be functionalized easily. Figure 7 shows the possible sensing mechanism that operates in CPs.

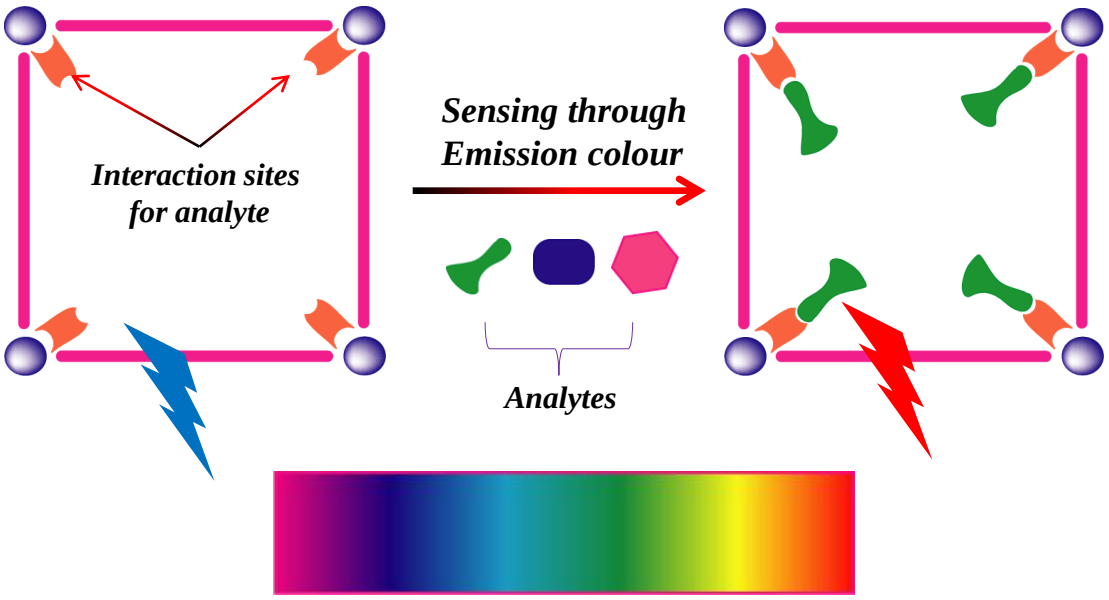

Figure 7: Scheme showing the possible mechanism of sensing through emission property.

PCP based sensory materials can be divided in two primary categories; lanthanide based PCPs and other PCPs which show linker based emission. Lanthanide based PCPs are comparatively less in the literature primarily because they are less advantageous as porous materials. Its high atomic weight and high coordination number generally leads to condensed non-porous structure but these are very attractive as luminescent material. Lanthanide ions are deprived of high absorption coefficient and hence they require an efficient antenna chromophore which can funnel the energy to the core electrons of the lanthanide centers. Hence, to see the emission characteristics of lanthanide metal a proper host material is required. With a proper antenna linker they show sharp emission with high life time and quantum yield. These emission characteristics and high coordination number have been exploited for sensing applications. Banglin Chen and co-workers have reported excellent sensing materials based on lanthanide PCPs. A {Tb(BTC)·*x*Solvent} (BTC = 1,3,5-benzene tricarboxylate) framework was used as fluoride anion sensor using hydrogen bonding interactions inside the pore surface (Figure 8).[24] Analogous {Eu(BTC)·*x*Solvent} PCP showed solvent responsive emission characteristics, particularly a very small amount of acetone can be easily detected by its luminescence quenching. This is due to the presence of unsaturated Eu^{3+} coordination sites which is available for solvent molecule coordination. In another example, a porous CP {Eu(PDC)DMF} was used for Cu^{2+} sensing applications. Here Cu^{2+} binds to the available pyridyl nitrogen center and thus quenches the Eu^{3+} emission.

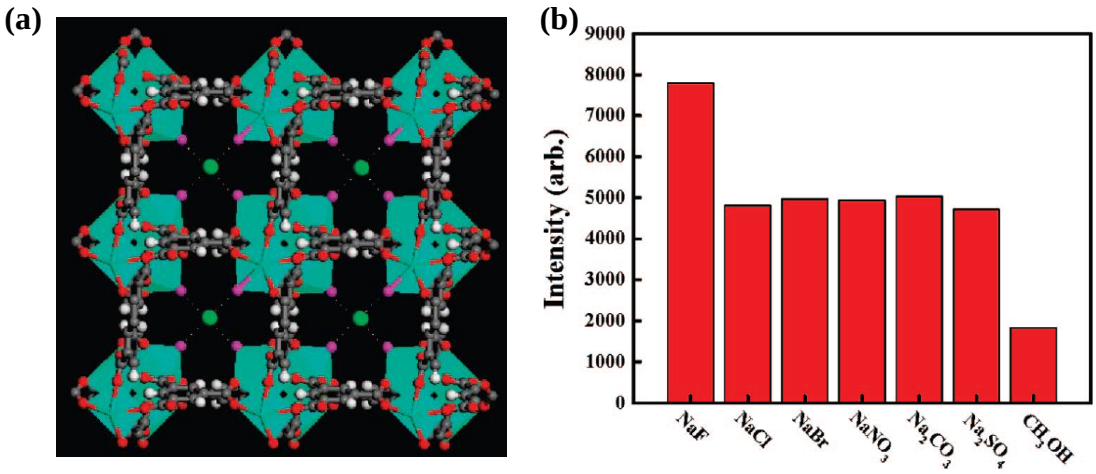

Figure 8: (a) Single crystal structure of Tb(BTC) PCP showing the position of F^- anion inside the pore and hydrogen bonding interaction between methanol and F^-; (b) $^5D_4 \rightarrow {}^7F_5$ transition intensities of activated Tb(BTC) in different types of 10^{-2} NaX and Na_2X methanol solution (λ_{ex} = 353 nm, λ_{mon} = 548 nm). These figures have been reproduced with permission from reference no. 24.

Based on linker centered emission several PCPs are reported that show excellent molecular recognition properties. A pyrene linker based luminescent PCP, $[In_2(OH)_2(TBAPy)]\cdot$(guests) was reported by Rosseinsky *et. al.* which showed guest responsive luminescence property.[25a] Pyrene is a good fluorescent probe as its emission is sensitive to its local environment. The monomer and excimer emissions depend on the relative proximity between pyrene moieties. The pyrene core showed long lived life time and presence of various solvents modulate its emission characteristics. Introduction of luminescent guest molecules in a porous PCP is another way of generating luminescence and in that course complex photophysical processes such as exciplex, excimer or even electron transfer processes are reported. One of the most well-known example is reported by Kitagawa *et. al.*, $[Zn_2(bdc)_2(dpNDI)]_n$, { bdc = 1,4 benzene dicarboxylate, dpNDI = N,N′-di(4-pyridyl)-(1,4,5.8-naphthalene diimide)} which contains redox active dpNDI linker and inclusion of various aromatic guests showed different emission colours due to formation of guest:dpNDI exciplex with charge transfer characteristics (Figure 9).[25b] This feature of the PCP is explained as molecular decoding. Another PCP $\{Mg(DHT)(DMF)_2\}_n$, (DHT = 2,5-dihydroxy terepthalic acid) which shows ESIPT (excited state intramolecular proton transfer) phenomenon due to presence of ESIPT active DHT, was used for ammonia sensing in vapour phase.[25c]

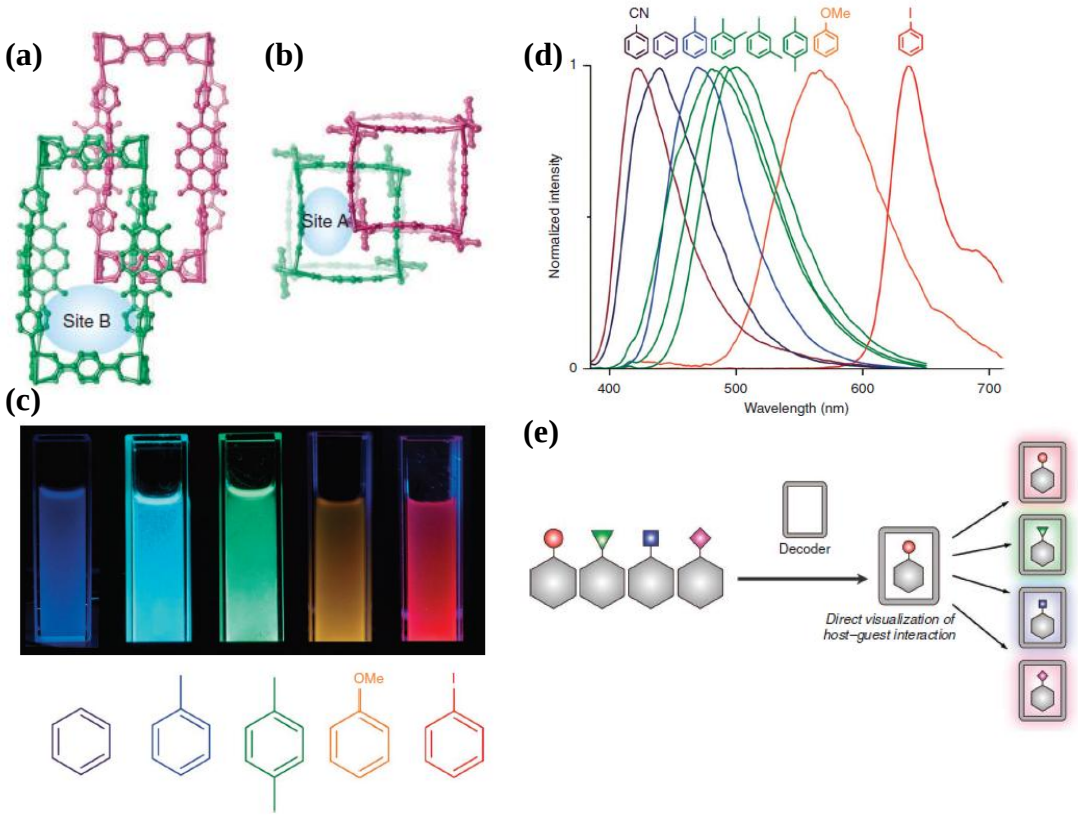

Figure 9: (a, b) View of two different sites in two-fold entangled structure of $[Zn_2(bdc)_2(dpNDI)]_n$, (c) Emission of different VOCs included framework under UV light, (d) Emission spectra of framework with different VOCs incorporated, (e) Schematic of molecular decoding phenomenon. These figures have been reproduced with permission from reference no. 25b.

Apart from these PCPs, metal-organic complexes also show sensing/recognition properties. In 2007, a 2D coordination compound, $\{[Cu_2(HL)(N_3)]\cdot ClO_4\}_\infty$ (**1**) (H_3L= 2,6-bis(hydroxyethyliminoethyl)-4-methyl phenol) was synthesized by Banerjee *et. al.*.[25d] Each $[Cu(HL)(N_3)]^+$ species is connected to its adjacent unit by a bridging alkoxide oxygen atom of the ligand to form a helical propagation along the crystallographic *a* axis. These helices are connected by ligand alcoholic oxygen atom along crystallographic *b* axis to form pleated 2D sheets. The framework dissociates in solution to produce $[Cu_2(HL)_2(H_3L)]\cdot 2H_2O$ (**2**), which act as a metalloligand. Approximately 19–fold Zn^{2+} selective chelation-enhanced fluorescence is observed in HEPES buffer (pH 7.4). Hence, **1** can act as Zn^{2+} selective fluorescent probe for biological applications.

1.4.2.2 Tunable Emission

Development of solid state light emitting materials is important for display and lighting technology. Tuning the emission colour and controlling the relative amount of monochromatic emissions in a material can lead to white light emission which is imperative for display devices. Full colour capability in a single material greatly simplifies the fabrication process of such white light emitting devices. Crystalline PCPs are excellent candidates for such light emitting devices as multi-colour emitting sites can be impeded in the same matrix. Only organic or only inorganic components can cover a part of the visible spectrum. This drawback is overcome by PCPs possessing both organic and inorganic constituents. A variety of PCPs with tuneable emission properties and white light emission have been investigated for this purpose.

Lanthanide (Ln) metal containing materials have attracted considerable interest in this field. The red (Eu^{3+}, Pr^{3+} and Sm^{3+}), green (Tb^{3+} and Er^{3+}) and blue (Tm^{3+}, Ce^{3+} and Dy^{3+}) emitting ions when combined judiciously with proper organic ligand or doped in a host, the material can emit across the entire visible spectrum. For example, a family of multifunctional desolvated Ln PCPs, LnL (Ln = Y, La-Yb except Pm) was synthesized using ligand (H_3L = 4,4′-((2-((4-carboxyphenoxy)methyl)-2-methylpropane-1,3-diyl)bis(oxy))dibenzoic acid).[26a] White light emission was successfully realized by co-doping Dy/Eu or Dy/Sm into analogous Gd compound. Another example include synthesis of two isostructural Ln-Zn (Ln=Eu,Tb) heterometallic frameworks of Eu^{3+} and Tb^{3+} using 4-(1H-tetrazol-5-yl)-biphenyl-3-carboxylic acid as ligand.[26b] Different percentage of Eu^{3+} has been doped in the Tb^{3+} PCPs which showed colour tunability leading to nearly white light emissions. CIE coordinate of (0.331, 0.328) is achieved in the presence of 0.5% Eu^{3+} ions.

Encapsulation of functional species in a PCP can also show colour tunability. A mesoporous blue emitting anionic PCP, $[(CH_3)_2NH_2]_{15}[(Cd_2Cl)_3(TATPT)_4]\cdot 12DMF\cdot 18H_2O$ {TATPT= 2,4,6-tris(2,5-dicarboxylphenylamino)-1,3,5triazine} has been synthesized by Li *et. al.* which contained two types of pore with dimensions of ~ 2 and 3 nm.[26c] Different concentrations of yellow emissive, $[Ir(ppy)_2(bpy)]^+$ complex is successfully incorporated inside the pores of this framework. 3.5 wt% of the complex in the PCP resulted in white light emitting material with CIE coordinates (0.31, 0.33) (Figure 10). Maji *et. al.* have reported a new phenomenon in PCP known as excited state intramolecular proton transfer using di-

hydroxy terepthalic acid as a linker. The $\{Mg(DHT)(DMF)_2\}_n$ PCP shows tunable emission colour in presence of solvents like DMF, methanol, water due to the presence of ESIPT process.

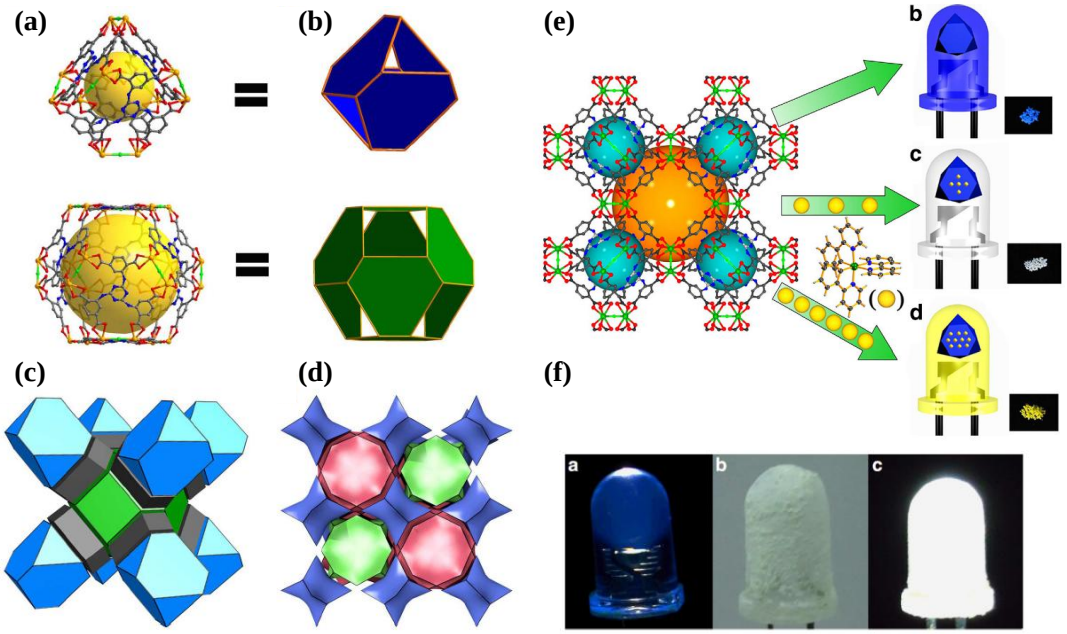

Figure 10: Structural details of $[(CH_3)_2NH_2]_{15}[(Cd_2Cl)_3(TATPT)_4]\cdot 12DMF\cdot 18H_2O$ (**1**) : (a) Truncated tetrahedral and octahedral cages; (b) polyhedra of cages; (c) 3D polyhedral structure; (d) 3,4-connected augmented net; (e) 3D structure , the orange and dark cyan spheres represent the void inside the cages; (f) Photographs of the LEDs, (a) An illuminating 3mm reference ultraviolet LED (turned-on emission has a blue tinge). (b) The same LED coated with a thin layer of sample of 3.5 wt% $[Ir(ppy)_2(bpy)]^+$@**1** (not turned on). (c) The coated LED was turned on and illuminates bright white light. These figures have been reproduced with permission from reference no. 26c.

Apart from PCPs, luminescent metal-organic complexes have also attracted attention of researchers. Su *et. al.* have demonstrated the synthesis of 4d-4f heterometallic Ag-Ln complexes; $\{[EuAg_3(3\text{-}TPyMNTB)_2(H_2O)(MeCN)](ClO_4)_6\cdot 4MeCN\}$ (**2-Eu-Ag**) and $\{[GdAg_3(3\text{-}TPyMNTB)_2(H_2O)(MeCN)](ClO_4)_6\cdot 4MeCN\}$ (**2-Gd-Ag**), (3-TPyMNTB) = tris((pyridin-3-lmethyl)benzoimidazol-2-ylmethyl)amine) through stepwise self assembly of predesigned Ln^{3+} monomeric complexes { $[Eu(3\text{-}TPyMNTB)_2](ClO_4)_3\cdot 2.5MeCN$ and $[Gd(3\text{-}PyMNTB)_2]\text{-}(ClO_4)_3\cdot 2MeCN\cdot 2CHCl_3$}, respectively with the Ag^+ ions.[26d] In **2-Eu-Ag**, the ligand centered emission is resensitized by Ag^+ to generate dual emission (the metal-centered f−f emission characteristic of Eu^{3+} ion and ligand-centered excimer emission sensitized by Ag^+ ion) leading to white light emission from single crystal. The complexation of metal ions by conjugated organic

molecules can improve structural rigidity which can help in sustaining many excitation-emission cycles. As a result metal-organic complexes can exhibit enhanced fluorescence and can find application in optoelectronic devices. In 2009, Roh *et. al.* studied several green-emitting Zn(II) complexes with benzothiazole and its derivatives to produce white-light emission.[26e] They reported a high luminance (1 cdm^{-2} at 3.5 V, 10400 cdm^{-2} at 14 V) in multilayer electroluminescent devices for one of the fluorenyl-substituted Zn(II) complex.

1.4.2.3 Light Harvesting

The concept of light harvesting or energy transfer is inspired by the process of natural photosynthesis. Resonance energy transfer (RET) is a process in which the excited molecule (donor) transfers its energy very rapidly to adjacent molecule (acceptor) through a non-radiative pathway such that the lifetime of the donor excited state is shortened. This forms the basis of light harvesting. Theodor Förster suggested the mechanism of RET and the phenomenon is called Förster resonance energy transfer (FRET). This energy transfer occurs via coupling of the multipolar transition moments of the donor and acceptor molecules through coulombic (electrostatic) interaction. The extent of energy transfer is determined by the distance between the donor and acceptor and the extent of spectral overlap. The typical distance between chromophores for FRET to occur is about 30-100 Å.

Studies of artificial and natural light harvesting systems have suggested that the energy transfer and antenna behaviour are most effectively accomplished by assembling ordered networks of chromophores. This type of long range organization and order can be achieved in MOFs and hence they can function as light harvesters. There are two possible pathways to achieve so: a) linker-to-linker or strut-to-strut energy transfer; b) host to guest energy transfer. A strut-to-strut energy transfer process was reported by Hupp *et. al.* in a PCP, containing porphyrin as primary chromophore and pyridine functionalized boron dipyrromethane (bodipy) as antenna.[27a] Bodipy has high fluorescence quantum yield, large molar absorption coefficient, low rate of intersystem crossing, long excited state lifetime and also excellent photo stability. It act as antenna chromophore and excites porphyrine struts collecting most of the light across the visible spectrum through efficient and rapid energy transfer. But porphyrin based MOFs have the drawback of limited coverage of the visible spectrum for light harvesting applications. Hence, Hupp *et. al.*

reported porphyrin based PCPs functionalized with CdSe/ZnS core/shell quantum dots (QDs) for the enhancement of light harvesting efficiency (>80%) through energy transfer from QDs to the PCPs.[27b] Nanocrystalline PCPs are also explored as light harvesting materials. In this case the chromophores are densely embedded within the framework which can increase cross section for light absorption and also the solution based behaviour of nanocrystals provide potential for further applications. One such example was reported by Uvdal *et. al*.[27c] They synthesized highly crystalline Ln-PCP nanoparticles with efficient light harvesting properties.

In another example light harvesting phenomenon was demonstrated in a metal organic complex. In 2004, Holten *et. al.* synthesized a triad composed of two porphyrins and an intervening bis(dipyrrinato) zinc complex.[27d] The zinc dipyrrin moiety absorbs light between the absorption of porphyrin (near UV) and visible region and transfers excited state energy to the porphyrins in ~ 2 ps with 99% yield. Hence, the Zn complex in such triads not only self assembles the linker but also act as an accessory pigment. The excited state characteristics of the complex can be altered by simple substitution for better properties. Maji *et. al*. reported a pyrene based metal-organic complex, {[Mg(*o*-phen)(H_2O)$_4$]·2(PBA)·(H_2O)} (PBA = pyrene butyric acid, *o*-phen = ortho-phenanthroline) based on the self-assembly through π-π stacking, H-bonding and C-H···π interactions (Figure 11).[27e] There are two types of PBA in the framework (PBA1 and PBA2). Spatial disposition of the chromophores renders unique surrounding which lead to an exciplex (PBA1:*o*-phen) emission. Emission corresponding to pyrene monomer (PBA2) is quenched in this compound suggesting the occurrence of energy transfer phenomenon from pyrene monomer to the exciplex formed. The perfect spectral overlap of the excitation spectrum of the compound with the emission of PBA monomer further confirms this process.

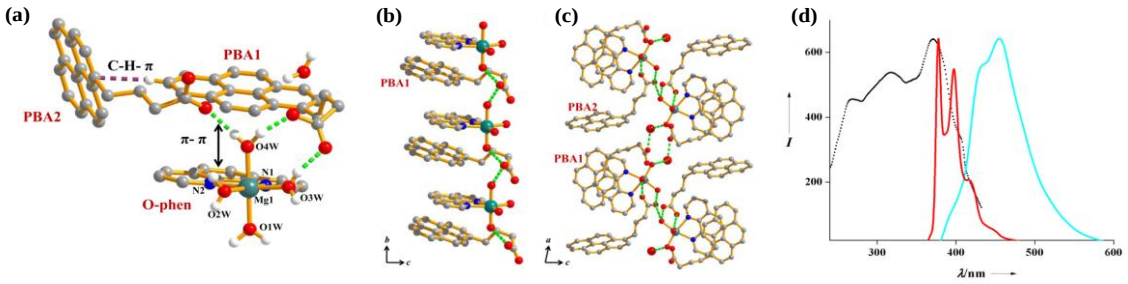

Figure 11: Structural details of {[Mg(o-phen)(H_2O)$_4$]·2(PBA)·(H_2O)}: (a) View of the asymmetric unit showing the orientation and assembly of PBA1, PBA2, and *o*-phen (dotted lines indicate H bonds); (b) 1D chain formed by p–p stacking of PBA1 and *o*-phen along the *b*-axis. The chain is supported by H-bonding interactions of the pyrene carboxylate groups with the coordinated water molecules; (c) Top view of the PBA1–*o*-phen π-stacked columns, which are separated by orthogonally oriented PBA2 molecules. The guest water molecules and PBA2 help the 1D chain to grow to higher dimension (d) Excitation spectra (monitored at 452 nm, dotted lines) and emission spectra ($\mathbf{l}_{ex}$=345 nm) of the crystals. These figures have been reproduced with permission from reference no. 27e.

1.5 Outlook

In the recent years, PCPs have attracted a lot of attention due to all its above discussed applications such as gas storage, separation, catalysis and sensing. Although construction and design of porous PCPs for the targeted applications are many, very few describes the self-assembly process involves in it. Use of non-covalent interactions can also be an interesting prospect for PCPs. Hence, we aim primarily to involve such organic chromophore systems that can undergo versatile non-covalent interactions such as π···π, C-H···π or hydrogen bonding. Organic chromophores such as anthracene, phenanthroline, naphthalene or even larger π surface area systems can also be employed for PCP construction as these chromophores act as charge donor/acceptor system. Additionally, these would also originate versatile structural topologies which are not studied in great details. Use of luminophore aromatic systems in PCPs can give rise to versatile applications such as solid state lighting, light harvesting etc. Use of supramolecular encapsulation method in PCPs is known but these are hardly exploited for light harvesting or multiple colour emission properties of such systems. Apart from organic luminophores lanthanide metal ions can also be exploited for sensing/recognition or multicolour emission properties.

1.6 References

1 (a) J. J. Perry IV, J. A. Perman and M. J. Zaworotko, *Chem. Soc. Rev.*, 2009, **38**, 1400; (b) J.-R. Li, R. J. Kuppler and H.-C. Zhou, *Chem. Soc. Rev.*, 2009, **38**, 1477; (c) Y. Cui, Y. Yue, G. Qian and B. Chen, *Chem. Rev.*, 2012, **112**, 1126; (d) J. Li, J. Sculley and H. Zhou, *Chem. Rev.*, 2012, **112**, 869; (e) S. Kitagawa, R. Kitaura and S. Noro, *Angew. Chem. Int. Ed.*, 2004, **43**, 2334.

2 (a) D. Farrusseng, S. Aguado and C. Pinel, *Angew. Chem. Int. Ed.*, 2009, **48**, 7502; (b) C. Wu, A. Hu, L. Zhang and W. Lin, *J. Am. Chem. Soc.,* 2005, **127**, 8940.

3 (a) O. M. Yaghi and H. Li, *J. Am. Chem. Soc.*,1996, **118**, 295; (b) T. R. Whitfield, X. Wang, L. Liu, A. J. Jacobson, *Solid State Sciences*, 2005, **7**, 1096.

4 (a) T. Devic, C. Serre, N. Audebrand, J. Marrot and G. Férey, *J. Am. Chem. Soc.,* 2005, **127**, 12788; (b) X. Guo, G. Zhu, Z. Li, F. Sun, Z. Yangb and S. Qiu, *Chem. Commun.*, 2006, 3172.

5 (a) M. C. Das, S. Xiang, Z. Zhang and B. Chen, *Angew. Chem. Int. Ed*., 2011, **50**, 10510; (b) V. Chandrasekhar, C. Mohapatra and R. J. Butcher, *Cryst. Growth Des*., 2012, **12**, 3285; (c) R. W. Larsen, L. Wojtas, J. Perman, R. L. Musselman, M. J. Zaworotko and C. M. Vetromile, *J. Am. Chem. Soc.*, 2011, **133**, 10356; (d) H. Son, S. Jin, S. Patwardhan, S. J. Wezenberg, N. C. Jeong, M. So, C. E. Wilmer, A. A. Sarjeant, G. C. Schatz, R. Q. Snurr, O. K. Farha, G. P. Wiederrecht and J. T. Hupp, *J. Am. Chem. Soc*., 2013, **135**, 862; (e) A. A. Sinelshchikova, S. E. Nefedov, Y. Y. Enakieva, Y. G. Gorbunova, A. Y. Tsivadze, K. M. Kadish, P. Chen, A. Bessmertnykh-Lemeune, C. Stern and R. Guilard, *Inorg. Chem.*, 2013, **52**, 999.

6 (a) R. Yang, L. Li, Y. Xiong, J. Li, H. Zhou and C. Su, *Chem. Asian J*., 2010, **5**, 2358; (b) J. Cheng, S. Zheng and G. Yang, *Inorg. Chem*., 2007, **46**, 10261; (c) S. Noro, Y. Hijikata, M. Inukai, T. Fukushima, S. Horike, M. Higuchi, S. Kitagawa, T. Akutagawa and T. Nakamura, *Inorg. Chem*., 2013, **52**, 280.

7 (a) T. K. Maji, S. Pal, K. L Gurunatha, A. Govindaraj and C. N. R. Rao, *Dalton Trans.*, 2009, 4426; (b) A. Chakraborty and T. K. Maji, *Proceedings of the National Academy of Sciences, Indian Section A :Physical Sciences. ,* 2014, (J. No. 40010; Article No. 119).

8 (a) F. Chang, H. Sun, H. Kou and S. Gao, *Inorg. Chem. Comm.*, 2002, **5**, 660; (b) H. Zhao, A. J. Brown, A. V. Prosvirin and K. R. Dunbar, *Polyhedron*, 2013, **64**, 321; (c) B. Sieklucka, R. Podgajny, T. Korzeniak, P. Przychodzen and R. Kania, *C. R. Chimie*, 2002, **5**, 639.

9 (a) O. Z. Yesxilel, G. Günay, C. Darcan, M. S. Soylu, S. Keskind and S. W. Ng, *CrystEngComm.*, 2012, **14**, 2817; (b) T. K. Maji, S. Pal, K. L Gurunatha, A. Govindaraj and C. N. R. Rao, *Dalton Trans.*, 2009, 4426.

10 (a) D. J. Tranchemontagne, J. L. Mendoza-Cortés, M. O'Keeffe and O. M. Yaghi, *Chem. Soc. Rev.*, 2009, **38**, 1257; (b) Y.-W. Li, J.-P. Zhao, L.-F. Wanga and X.-H. Bu, *CrystEngComm*, 2011, **13**, 6002; (c) Q. Yue, Q. Sun, A. Cheng and E. Gao, *Cryst. Growth. Des.*, 2010, **10**, 44; (d) R. Haldar, S. K. Reddy, V. M. Suresh, S. Mohapatra, S. Balasubramanian and T. K. Maji, *Chem. Eur. J.*, 2014, **20**, 1; (e) X. Wang, Y. Zhang, X. Cheng and X. Chen, *CrystEngComm*, 2008, **10**, 753.

11 S. Kitagawa, R. Kitaura and S. Noro, *Angew. Chem. Int. Ed*., 2004, **43**, 2334.

12 (a) S. Mohapatra, H. Sato, R. Matsuda, S. Kitagawa and T. K. Maji, *CrystEngComm*, 2012, **14**, 4153; (b) Y. Chen, T. Hoang and S. Ma, *Inorg. Chem.*, 2012, **51**, 12600; (c) B. Chen, L. Wang, F. Zapata, G. Qian and E. B. Lobkovsky, *J. Am. Chem. Soc*., 2008, **130**, 6718.

13 (a) R. Grünker, I. Senkovska, R. Biedermann, N. Klein, M. R. Lohe, P. Müller and S. Kaskel, *Chem. Commun.*, 2011, **47**, 490; (b) S. Sanda, S. Parshamoni, and S. Konar, *Inorg. Chem.*, 2013, **52**, 12866; (c) P. Kanoo, A. C. Ghosh, S. T. Cyriac and T. K. Maji, *Chem. Eur. J.*, 2012, **18**, 237; (d) P. Horcajada, C. Serre, G. Maurin, N. A. Ramsahye, F. Balas, M. Vallet-Regí, M. Sebban, F. Taulelle and G. Férey, *J. Am. Chem. Soc*., 2008, **130**, 6774.

14 (a) O. M. Yaghi, M. Keeffe, N. W. Ockwig, H. K. Chae, M. Eddaoudi and J. Kim, *Nature*, 2003, **423**, 705; (b) M. Eddaoudi, J. Kim, N. Rosi, D. Vodak, J. Wachter, M. O'Keeffe and O. M. Yaghi, *Science*, 2002, **295,** 469; (c) H. K. Chae, D. Y. Siberio-Perez, J. Kim, Y. Go, M. Eddaoudi, A. J. Matzger, M. O'Keeffe and O. M. Yaghi, *Nature*, 2004, **427**, 523; (d) S. Y. Chui, S. Lo, J. P. H. Charmant, A. Orpen and I. D. Williams, *Science*, 1999, **283**, 1148; (e) A. Phan, C. Doonan, F. Uribe-Romo, C. B. Knobler, M. Keefee and O. M. Yaghi, *Acc. Chem.. Res*., 2010, **43**, 58; (f) L. T. L. Nguyen, K. K. A. Le, H. X. Truong and N. T. S. Phan, *Catal. Sci. Technol.*, 2012, **2**, 521; (g) G. Férey, C. Mellot-Draznieks, C. Serre, F. Millange, J. Dutour, S. Surblé and I. Margiolaki, *Science*, 2005, **309**, 2040; (h) G. Férey, C. Serre, C. Mellot-Draznieks, F. Millange, S. Surblé, J. Dutour and I. Margiolaki, *Angew. Chem. Int. Ed.*, 2004, **43**, 6296.

15 (a) S. Horiuchi, F. Ishii, R. Kumai, Y. Okimoto, H. Tachibana, N. Nagaosa and Y. Tokura, *Nat. Mater*., 2005, **4**, 163; (b) D. Yan, A. Delori, G. O. Lloyd, T. Friŝĉić, G. M.

Day, W. Jones, J. Lu, M. Wei, D. G. Evans and X. Duan, *Angew. Chem. Int. Ed*., 2011, **50**, 12483.

16 (a) W. Fujita, K. Awaga, R. Kondo and S. Kagoshima, *J. Am. Chem. Soc*., 2006, **128**, 6016; (b) Y. Wang, B. Bredenkötter, B. Riegera and D. Volkmer, *Dalton Trans.*, 2007, 689.

17 (a) P. Kanoo, K. L. Gurunatha and T. K. Maji, *Cryst. Growth Des.*, 2009, **9**, 4147; (b) G. J. McManus, J. J. Perry IV, M. Perry, B. D. Wagner and M. J. Zaworotko, *J. Am. Chem. Soc*., 2007, **129**, 9094; (c) B. D. Wagner, G. J. McManus, B. Moulton and M. J. Zaworotko, *Chem. Commun.*, 2002, 2176; (d) X. Li, X. Fan and Q. Zeng, *Int. J. Mol. Sci*., 2007, **8**, 29; (e) X. Chen and G. Liu, *Chem. Eur. J.*, 2002, **8**, 4811.

18 (a) O. K. Farha, I. Eryazici, N. C. Jeong, B. G. Hauser, C. E. Wilmer, A. A. Sarjeant, Q. Snurr, S. T. Nguyen, A. Ö. Yazaydın and J. T. Hupp, *J. Am. Chem. Soc*. 2012, **134**, 15016; (b) H. K. Chae, D. Y. Siberio-Perez, J. Kim, Y. Go, M. Eddaoudi, A. J. Matzger, M. O'Keeffe and O. M. Yaghi, *Nature* 2004, **427**, 523; (c) G. Férey, C. Mellot-Draznieks, C. Serre, F. Millange, J. Dutour, S. Surble and I. Margiolaki, *Science*, 2005, **309**, 2040; (d) K. Koh, A. G. Wong-Foy and A. J. Matzger, *J. Am. Chem. Soc.*, 2009, **131**, 4184; (e) H. Furukawa, N. Ko, Y. B. Go, N. Aratani, S. B. Choi, E. Choi, A. O. Yazaydin, R. Q. Snurr, M. O'Keeffe, J. Kim and O. M. Yaghi, *Science*, 2010, **329**, 424.

19 (a) O. K. Farha, A. Ö. Yaza -ydın, I. Eryazici, C. D. Malliakas, B. G. Hauser, M. G. Kanatzidis, S. T. Nguyen, R. Q. Snurr and J. T. Hupp, *Nat. Chem*., 2010, **2**, 944; (b) S. Q. Ma, D. F. Sun, J. M. Simmons, C. D. Collier, D. Q. Yuan and H.-C. Zhou, *J. Am. Chem. Soc*., 2008, **130**, 1012; (c) S.-C. Xiang, W. Zhou, Z.-J. Zhang, M. A Green, Y. Liu and B. Chen, *Angew. Chem., Int. Ed*., 2010, **49**, 4615.

20 (a) A. R. Millward, O. M Yaghi, *J. Am. Chem. Soc*., 2005, **127**, 17998; (b) A. G. Wong-Foy, A. J. Matzger and O. M. Yaghi, *J. Am. Chem. Soc*., 2006, **128**, 3494.

21 (a) M. Fujita, Y. J. Kwon, S. Washizu and K. Ogura, *J. Am. Chem. Soc*., 1994, **116**, 1151; (b) S. S. Chui, S. M. Lo, J. P. Charmant, A. G. Orpen and I. D. Williams, *Science*, 1999, **283**, 1148; (c) L. Alaerts, E. Séguin, H. Poelman, F. Thibault-Starzyk, P. A. Jacobs and D. E. D. Vos, *Chem.–Eur. J*., 2006, **12**, 7353.

22 (a) M. Kurmoo, *Chem. Soc. Rev.*, 2009, **38**, 1353; (b) K. Zou, J. Zhao, C. Liu, Z. Wang and Z. Li, *Eur. J. Inorg. Chem.* 2013, 293; (c) T. Aharen, F. Habib, I. Korobkov, T. J. Burchell, R. Guillet-Nicolas, F. Kleizb and M. Murugesu, *Dalton Trans*., 2013, **42**, 7795.

23 (a) P. Horcajada, T. Chalati, C. Serre, B. Gillet, C. Sebrie, T. Baati, J. F. Eubank, E. Heurtaux, P. Clayette, C. Kreuz, J.-S. Chang, Y. K. Hwang, V. Marsaud, P.-N. Bories, L. Cynober, S. Gil, G. Férey, P. Couvreur and R. Gref, *Nat. Mater*., 2010, **9**, 172; (b) N. J. Hinks, A. C. McKinlay, B. Xiao, P. S. Wheatley and R. E. Morris, *Microporous Mesoporous Mater.*, 2010, **129**, 330; (c) J. An, S. J. Geib and N. L. Rosi, *J. Am. Chem. Soc*., 2009, **131**, 8376.

24 B. Chen, L. Wang, F. Zapata, G. Qian and E. B. Lobkovsky, *J. Am. Chem. Soc*., 2008, **130**, 6718.

25 (a) K. C. Stylianou, R. Heck, S. Y. Chong, J. Bacsa, J. T. A. Jones, Y. Z. Khimyak, D. Bradshaw and M. J. Rosseinsky, *J. Am. Chem. Soc*., 2010, **132**, 4119; (b) Y. Takashima, V. M. Martínez, S. Furukawa, M. Kondo, S. Shimomura, H. Uehara1, M. Nakahama, K. Sugimoto and S. Kitagawa, *Nat. Commun*., 2011, **2**, 168; (c) K. Jayaramulu, R. P. Narayanan, S. J. George and T. K. Maji, *Inorg. Chem.*, 2012, **51**, 10089; (d) K. Dhara, S. Karan, J. Ratha, P. Roy, G. Chandra, M. Manassero, B. Mallik and P. Banerjee, *Chem. Asian J*., 2007, **2**, 1091.

26 (a) S. Dang, J. Zhang and Z. Sun, *J. Mater. Chem.*, 2012, **22**, 8868; (b) Z. Liu, M. Wu, S. Wang, F. Zheng, G. E. Wang, J. Chen, Y. Xiao, A. Wu, G. Guo and J. Huang, *J. Mater. Chem. C*, 2013, **1**, 4634; (c) C. Sun, X. Wang, X. Zhang, C. Qin, P. Li, Z. Su, D. Zhu, G. Shan, K. Shao, H. Wu and J. Li, *Nat. Commun*., 2013, **4**, 2717; (d) Y. Liu, M. Pan, Q. Y. Yang, L. Fu, K. Li, S. Wei and C. Su, *Chem. Mater*., 2012, **24**, 1954; (e) S. Roh, Y. Kim, K. D. Seo, D. H. Lee, H. K. Kim, Y. Park, J. Park and J. Lee, *Adv. Funct. Mater.*, 2009, **19**, 1663.

27 (a) C. Y. Lee, O. K. Farha, B. J. Hong, A. A. Sarjeant, S. T. Nguyen and J. T. Hupp, *J. Am. Chem. Soc.*, 2011, **133**, 15858; (b) S. Jin, H. Son, O. K. Farha, G. P. Wiederrecht and J. T. Hupp, *J. Am. Chem. Soc*., 2013, **135**, 955; (c) X. Zhang, M. A. Ballem, Z. Hu, P. Bergman and K. Uvdal, *Angew. Chem. Int. Ed*., 2011, **50**, 5729; (d) I. V. Sazanovich, C. Kirmaier, E. Hindin, L. Yu, D. F. Bocian, J. S. Lindsey and D. Holten, *J. Am. Chem. Soc*., 2004, **126**, 2664; (e) R. Haldar, K. V. Rao, S. J. George and T. K. Maji, *Chem. Eur. J*., 2012, **18**, 5848.

Chapter: 2

Strategic design of flexible supramolecular non-porous to porous host based on a pyrene core: Excimer emission and light harvesting

A manuscript based on this chapter has been submitted for publication.

Summary

In this chapter, crystal engineering concept is adopted to construct a porous luminescent supramolecular framework by changing the spatial arrangement of aromatic linker directed by ligand coordination. $\{Cd(oxo\text{-}pba)_2(H_2O)_2\}_n$ (**1**), a metal-organic complex is synthesized using a functionalized pyrene linker, 1-pyrene-γ-oxo-butyric acid (oxo-pba). Through π···π and C-H···π interactions this structure is extended to form a 2D supramolecular structure. Substitution of two *cis* water molecules by an aromatic chelator 2,2′-bipyridine (bpy) led to the formation of a new metal-organic complex $\{[Zn(oxo\text{-}pba)_2(bpy)]\cdot 4H_2O]\}_n$ (**2**), which extends to a porous 3D supramolecular structure *via* non-covalent interactions. Gas and solvent vapour adsorption studies indicate presence of both hydrophobic and-philic sites on the pore surfaces. Both the compounds show bright pyrene excimer emission. Furthermore light harvesting applications has been studied in compound **2** based on non-covalent encapsulation of a suitable acceptor dye acridine orange (AO). Efficient energy transfer from framework is realized by loading only 0.08 molecules of AO per formula of the compound **2**.

2.1 Introduction

The macroscopic properties of a metal-organic solid depend on the molecular ordering in the crystal lattice. Therefore the spatial organization of the constituent metal ion and ligand molecules in a metal-organic compound based on their structure and the metal ion geometry is crucial for designing magnetic and optoelectronic materials and also for their nonlinear activity, solid state reactivity and zeolite-like porous properties.[1] Recently, there has been an increased interest in the design of various excimer or exciplex based optoelectronic materials for the development of sensors and light emitting diodes.[2] But such studies based on inorganic-organic hybrid systems like in metal-organic coordination compounds are relatively unexplored area.[3] The coordination driven spatial organization of various organic chromophores appears to be beneficial, as it renders the different donor-acceptor pairing in a close proximity and enables efficient intermolecular charge transfer or energy transfer. Further metal coordination can positively restrict molecular rotation of the fluorophores, which block the non-radiative decay channels and hence enhances their fluorescence efficiencies.[4] Therefore, the fluorescence properties of such hybrid systems may be modulated based on wavelength shifts, intensity changes or even new emission with the increase in lifetimes as well as the quantum efficiencies. Among the different organic fluorophores pyrene and its derivatives have been extensively studied in the area of OLEDS due to its high fluoroscence quantum yield and life time.[5] The large aromatic π surface of pyrene can form strong π···π/C-H···π association with other molecules resulting in a bright red shifted excimer or exciplex emission.[6] On the other hand use of such high quantum yield chromophores as antenna in light harvesting is also exciting and such studies are very few in metal-organic system.[7] In this work, we have chosen a functionalized pyrene linker, 1-pyrene-γ-oxo-butyric acid (oxo-pba) and Cd^{2+} as precursors to synthesize a 2D supramolecular structure, $\{Cd(oxo\text{-}pba)_2(H_2O)_2\}_n$ (**1**). This 2D structure is held by π···π and C-H···π interactions and shows pyrene excimer emission. By manipulating the ligand coordination (inclusion of 2,2′-bipyridine (bpy) replacing the coordinated water) we could able to synthesize $\{[Zn(oxo\text{-}pba)_2(bpy)]\cdot 4H_2O]\}_n$ (**2**), which is a 3D supramolecular framework with permanent porosity (Scheme 1). Framework **2** also shows bright pyrene excimer emission. Further, presence of porosity and luminescence in **2** is exploited for light harvesting application by encapsulating a suitable acceptor dye, acridine orange (AO).

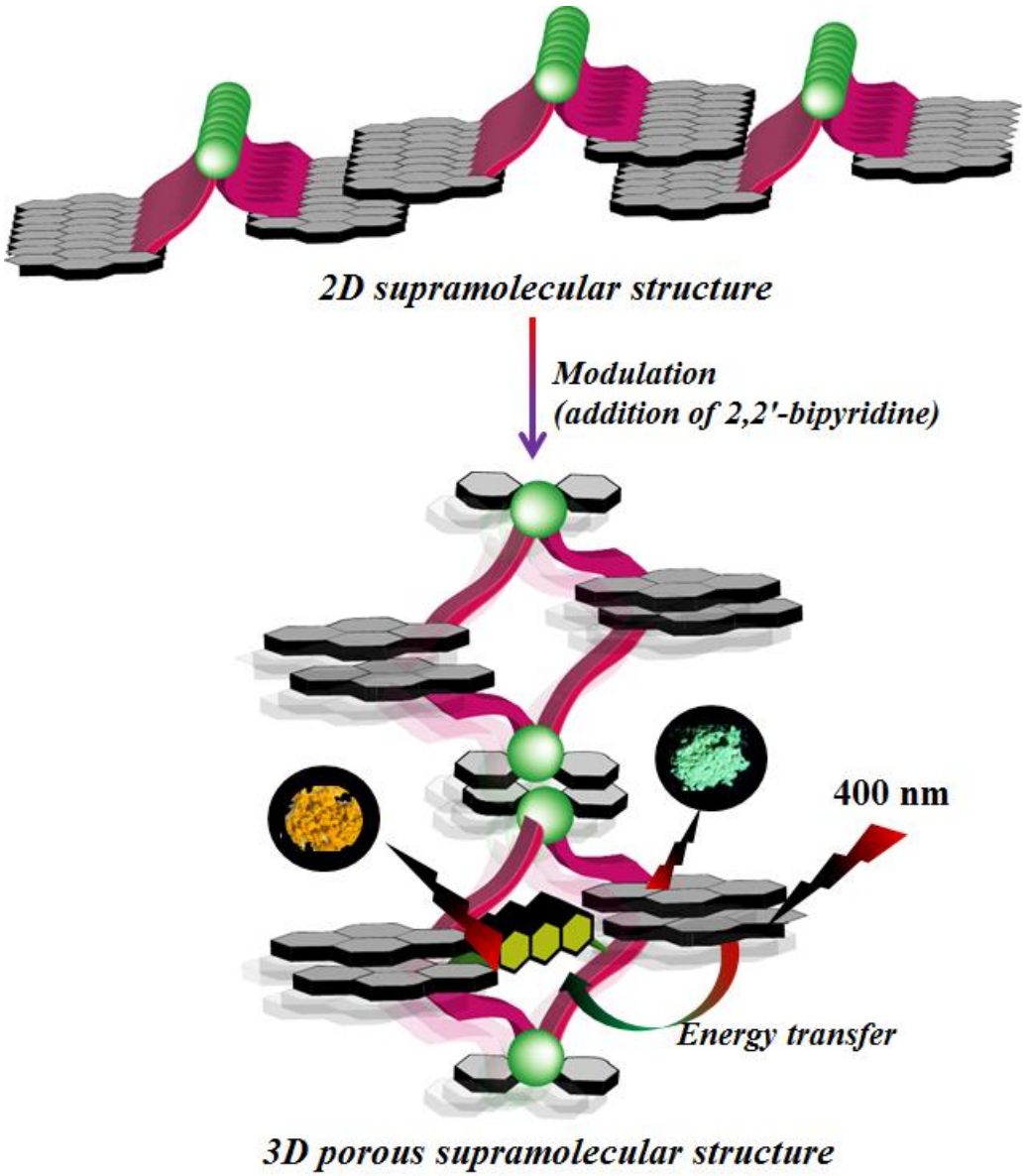

Scheme 1: Schematic of a crystal engineering approach to design porous 3D supramolecular structure from non-porous 2D structure.

2.2 Experimental Section

2.2.1 Materials

All the reagents were commercially available and used as provided without further purification. Metal salts were obtained from SDFCL, 1-pyrene-γ-oxo-butyric acid (oxo-pba) and 2,2′-bipyridine (bpy) were obtained from Sigma Aldrich chemicals. Acridine orange hydrochloride hydrate was purchased from Acros Organics.

2.2.2 Physical Measurements

Elemental analyses were carried out using a Thermo Fischer Flash 2000 Elemental Analyzer. FT-IR spectra were recorded on a Bruker IFS 66v/S spectrophotometer using KBr pellets in the region 4000–400 cm^{-1}. Thermogravimetric analysis (TGA) was carried out (Metler Toledo) in nitrogen atmosphere (flow rate = 50 $mLmin^{-1}$) in the temperature range 30–700 °C (heating rate = 3 °C min^{-1}). Powder X-ray diffraction (PXRD) pattern of the products were recorded on a Bruker D8 Discover instrument using Cu−Kα radiation. Electronic absorption spectra were recorded on a Perkin Elmer Lambda 900 UV-VIS-NIR Spectrometer and PL spectra were taken with Perkin-Elmer model LS 55 luminescence spectrometer. NMR spectrum was obtained with a Bruker AVANCE 400 (400 MHz) Fourier transform NMR spectrometer with chemical shifts reported in parts per million (ppm). Lifetime measurements were carried out at room temperature using Edinburgh Instrument FLSP920 spectrometer.

2.2.3 X-ray Crystallography

X-ray single crystal structural data of **1** and **2** were collected on a Bruker Smart-CCD diffractometer equipped with a normal focus, 2.4 kW sealed tube X-ray source with graphite monochromated Mo-Kα radiation (λ = 0.71073 Å) operating at 50 kV and 30 mA. The program SAINT[8] was used for integration of diffraction profiles and absorption correction was made with SADABS[9] program. All the structures were solved by SIR 92[10] and refined by the full matrix least-squares method using SHELXL-97.[11] All the hydrogen atoms were fixed by HFIX and placed in ideal positions. Potential solvent accessible area or void space was calculated using the PLATON multipurpose crystallographic software.[12] All crystallographic and structure refinement data of **1** and **2** are summarized in Table 1. Selected bond lengths and angles for **1** and **2** are given in Tables 2-5. All calculations were carried out using PLATON and WinGX system, Ver 1.70.01.[13]

2.2.4 Adsorption Measurements

Adsorption isotherms of N_2 (77 K and 195 K) and CO_2 (195 K) were recorded using the desolvated sample of **2** by using a QUANTACHROME QUADRASORB-SI analyzer. In the sample tube, the adsorbent sample (~ 100−150 mg) was placed which had been prepared at 80 °C under a 1×10^{-1} Pa vacuum for about 12 h prior to measurement of the isotherms. Helium gas (99.999% purity) at a certain pressure was introduced in the gas chamber and allowed to diffuse into the sample chamber by opening

the valve. The amount of gas adsorbed was calculated from the pressure difference ($P_{cal} - P_e$), where P_{cal} is the calculated pressure with no gas adsorption and P_e is the observed equilibrium pressure. All the operations were computer controlled and automatic.

The adsorption isotherm of different solvents (MeOH, at 293 K and water, at 298 K) for **2** was measured in the vapour state by using a BELSORP-aqua volumetric adsorption instrument from BEL, Japan. A sample of about ~ 100−150 mg was prepared by heating at 80 °C for about 12 h under a vacuum (1×10^{-1} Pa) prior to measurement of the isotherms. The solvent molecules used to generate the vapour were degassed fully by repeated evacuation. Dead volume was measured with helium gas. The adsorbate was placed into the sample tube, then the change of the pressure was monitored, and the degree of adsorption was determined by the decrease in pressure at the equilibrium state. All operations were computer controlled and automatic.

2.2.5 Syntheses

2.2.5.1 Synthesis of $\{Cd(oxo\text{-}pba)_2(H_2O)_2\}_n$ (1)

A 10 mL aqueous solution of oxo-pba (0.120 g, 0.4 mmol) was prepared using 0.1 M KOH solution in a glass vial. 10 mL methanolic solution of $Cd(NO_3)_2 \cdot 4H_2O$ (0.062 g, 0.2 mmol) was added to the ligand solution before it was sealed and kept in the oven at 80 °C. Good quality single crystals were obtained after 24 hours. Yield: 79%. Anal.calcd. for $C_{40}H_{30}O_8Cd$: C, 63.96; H, 3.99. Found C, 64.01; H, 4.23.

2.2.5.2 Synthesis of $\{[Zn(oxo\text{-}pba)_2(bpy)] \cdot 4H_2O\}_n$ (2)

A 10 mL aqueous solution of oxo-pba (0.120 g, 0.4 mmol) prepared using 0.1 M KOH and 10 mL methanolic bpy (0.031 g, 0.2 mmol) solution were mixed together and stirred for 30 minutes. $Zn(NO_3)_2 \cdot 6H_2O$ (0.059 g, 0.2 mmol) was dissolved in 10 mL water. 2 mL of this Zn(II) solution was slowly and carefully layered above the mixed ligand solution using 1 mL buffer (2:1 of water and methanol) solution. Good quality yellow coloured crystals were obtained after 15 days. The crystals were separated and washed with water/methanol (1:1) mixture and air dried. Yield: 81%. Anal.cald. for $C_{50}H_{42}N_2O_{10}Zn$: C, 67.55; H, 4.73; N, 3.15. Found C, 68.13; H, 4.27; N, 3.03. FT-IR (KBr pellet, 4000−400 cm^{-1}): 3450 (b), 3071 (m), 3038 (s), 2968 (s), 2920 (w), 2900 (s), 1672 (s), 1605 (m), 1593 (s), 1565 (s), 1540 (w), 1508 (s), 1490 (s), 1473 (s), 1441 (s), 1406 (b), 1383 (s), 1372 (m), 1345 (s), 1313 (s), 1298 (m), 1251 (s), 1232 (s), 1210 (s), 1192 (s), 1178 (s), 1166 (w), 1158 (s), 1141 (m), 1120 (s), 1078 (s), 1058 (s), 1041 (m),

1025 (s), 1015 (w), 992 (s), 972 (w), 959 (w), 954 (s), 917 (m), 880 (s), 845 (s), 820 (w), 802 (s), 776 (s), 736 (s), 720 (s), 694 (w), 682 (s), 652 (s), 632 (s), 600 (s), 555 (s), 547 (m), 518 (b), 504 (s), 421 (s). Bulk amount of the compound was synthesized in powder form by the direct mixing of the corresponding ligand solution with aqueous solution of Zn^{2+}.

2.2.5.3 Synthesis of Acridine Orange (AO) included 2 (2@AO)

0.03 g of desolvated compound **2** was dipped in 10^{-1} mM methanol solution of acridine orange (AO) dye. The mixture was then stirred for 48 hours, filtered, washed with fresh methanol and dried to obtain **2@AO** containing 0.08 molecule of AO dye per formula. Anal.cald. for $C_{51.36}H_{35.52}N_{2.24}O_6Zn$: C, 75.22; H, 4.34; N, 3.83. Found C, 75.97; H, 4.11; N, 3.61. FT-IR (KBr pellet, 4000−400 cm^{-1}): 3450 (b), 3071 (m), 3038 (s), 2968 (s), 2920 (w), 2900 (s), 2851 (w), 1672 (s), 1604 (w), 1594 (s), 1566 (m), 1540 (w), 1506 (s), 1489 (s), 1472 (s), 1441 (s), 1419 (s), 1384 (s), 1373 (m), 1346 (s), 1312 (m), 1298 (m), 1253 (s), 1232 (s), 1210 (s), 1191 (w), 1180 (s), 1157 (s), 1141 (m), 1123 (s), 1076 (s), 1058 (s), 1042 (w), 1026 (s), 1015 (w), 995 (s), 978 (w), 956 (s), 885 (s), 846 (s), 820 (w), 801 (s), 777 (s), 737 (s), 718 (s), 696 (m), 683 (s), 654 (s), 633 (s), 600 (m), 553 (m), 545 (m), 521 (w), 502 (m), 487 (w), 448 (m), 420 (w), 413 (m).

2.3 Results and Discussion

2.3.1 Structural Description of $\{Cd(oxo\text{-}pba)_2(H_2O)_2\}_n$ (1)

Compound **1**, synthesized in a solvothermal reaction of $Cd(NO_3)_2{\cdot}6H_2O$ and oxo-pba crystallizes in monoclinic *C*2/*c* space group. The asymmetric unit consists of one hexa-coordinated Cd^{2+} center, two oxo-pba and two coordinated water molecules (Figure 1a and Table 1-3). Four carboxylate oxygen atoms (O1, O1*, O2 and O2*) from two oxo-pba coordinates the Cd^{2+} center and the other two coordination sites are occupied by water molecules (O4 and O4*). The two oxo-pba act as two side arms of **1**, and extend as 1D column along *a*-direction through slightly off-set face-to-face π···π interaction (3.496 Å)

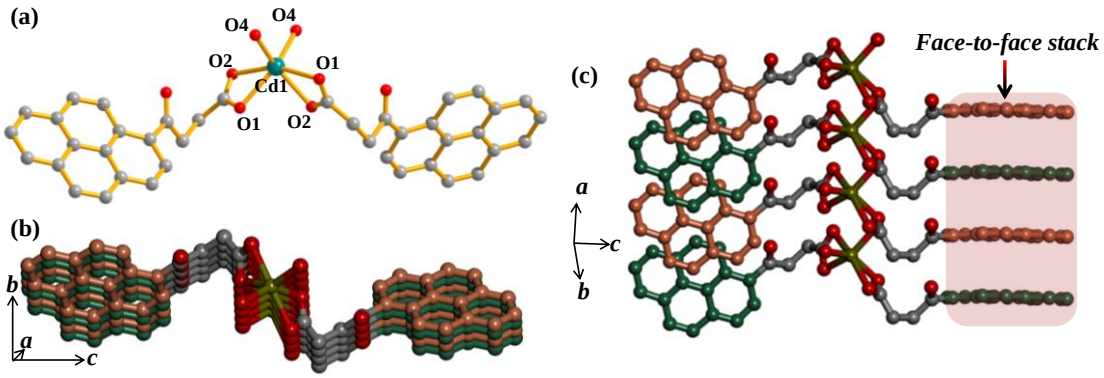

Figure 1: (a) Molecular complex of **1**; (b) 1D column like stacking in **1**; (c) Off-set face-to-face stacking in 1D column of **1**.

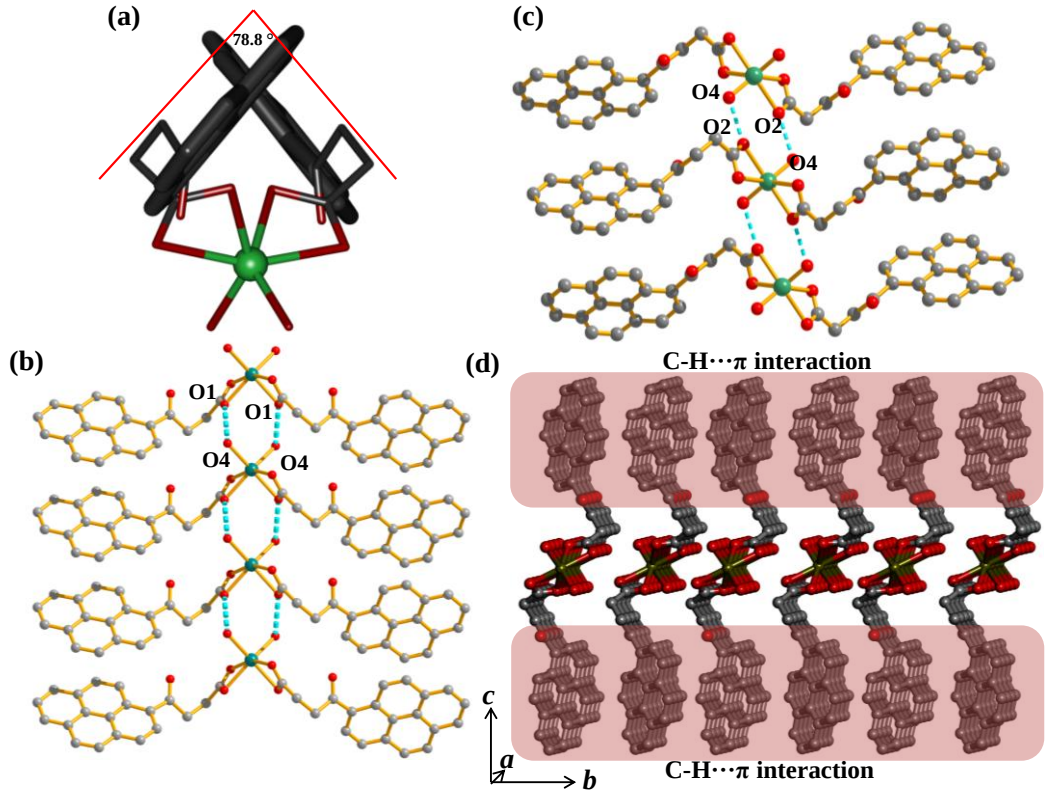

Figure 2: (a) Spatial disposition of pyrene rings in **1**; (b, c) Hydrogen bonding (cyan dotted lines) between O4-H···O1 and O4-H···O2 in **1**;(d) View of the C-H···π stacking to form a 2D layer like structure.

between the pyrene rings (Figure 1b-1c). The dihedral angle between two pyrene rings is 78.8 ° (Figure 2a). This is reinforced by H-bonding between coordinated waters (O4 and O4*) and carboxylate oxygens (O1 and O1*, respectively) (2.651 Å) (Figure 2b). This 1D

column is extended to 2D along *b*-axis by another H-bonding between coordinated water molecule (O4) and carboxylate oxygen (O2) (2.657 Å) (Figure 2c). Additionally, face-to-edge (~ 3.609 Å) interaction between pyrene rings of neighbouring 1D chains support strong packing (Figure 2d). But this 2D structure does not extend further along *c*-direction.

2.3.2 Modulation of Structure: Structural Description of $\{[Zn(oxo\text{-}pba)_2(bpy)]\cdot 4H_2O\}_n$ (2)

We envisage the replacement of two *cis*-oriented coordinated water molecules (O5 and O6) by a chelating ligand bpy which has similar coordination angle for further modification in the structure. This crystal engineering approach was unsuccessful for Cd^{2+} as suitable single crystal was not formed. But in a similar attempt with Zn^{2+} we could able to synthesize $\{[Zn(oxo\text{-}pba)_2(bpy)]\cdot 4H_2O\}_n$ (**2**). **2** crystallizes in monoclinic *C*2/*c* space group and it contains a hexa-coordinated Zn^{2+}; six coordination sites are occupied by four oxygen atoms (O1, O1_a, O2 and O2_a) of two carboxylate groups of two oxo-pba and two nitrogen atoms (N1, N1_a) from one bpy (Figure 3a and Table 1). The molecular structure roughly resembles **1**, but the pyrene spatial positions have significant change (spatial tilting angle is 59.1°) (Figure 3b). Two of such complexes meet each other in such a way that bpy stacks in a face-to-face fashion (3.635 Å) and the two arms of complex (oxo-pba) stack in face-to-edge fashion (3.601 Å) (Figure 4a-4b). This leads to 1D column (along *c*-direction) that has four arms directing in *ab* plane. These columns along four arms are interdigitated by off-set face-to-face π-π stacking (cg···cg ~ 3.498 Å) between oxo-pba to form a 3D supramolecular framework structure with 1D distorted rectangular shaped channels (6.2 × 6.2 $Å^2$) along *c*-direction (Figure 4c-e).[14] These channels are filled with guest water molecule (O1W) which are hydrogen bonded to the carboxylate oxygen O1 (O1w···O1 = 2.748-3.052 Å) (Figure 5a). Removal of all the solvent molecules create a void space of 15.7% of total cell volume.[14] Interestingly, the pore surface is decorated with the oxygen atoms from the carboxylate groups (hydrophilic) and also aromatic pyrene rings (hydrophobic) (Figure 5b).

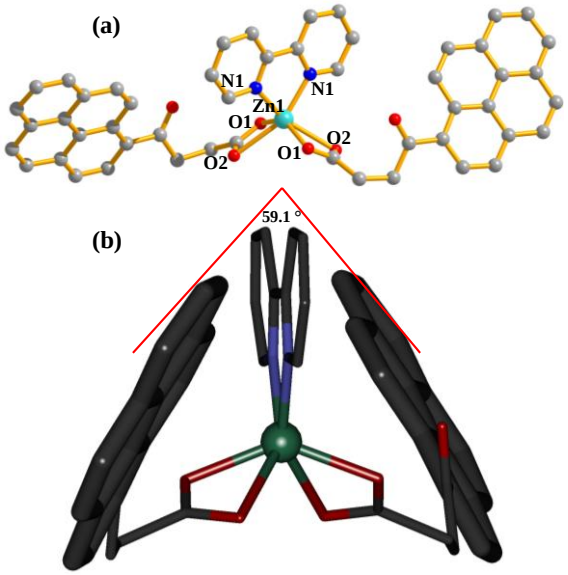

Figure 3: (a) Molecular complex of **2**; (b) Spatial disposition of pyrene rings in **2** with a dihedral angle of 59.1°.

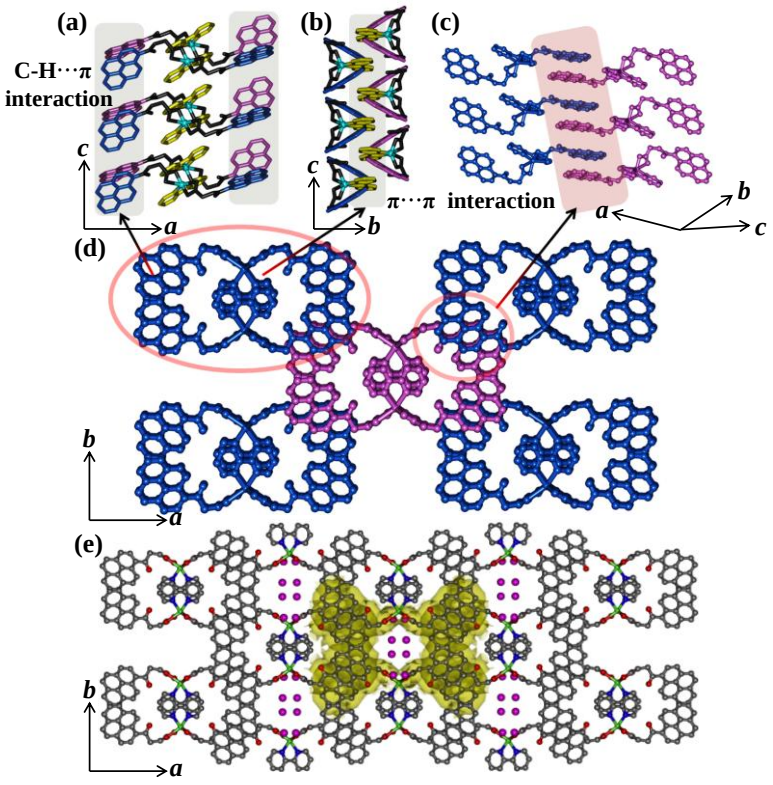

Figure 4: (a) Face-to-edge stacking of oxo-pba along *c*-axis in **2**; (b) Face-to-face stacking of bpy along *c*-axis in **2**; (c) Face-to-face stacking of oxo-pba; (d) View along *c*-direction showing the 1D columnar stack in different colours; (e) View of the 1D pore filled with guest water molecules.

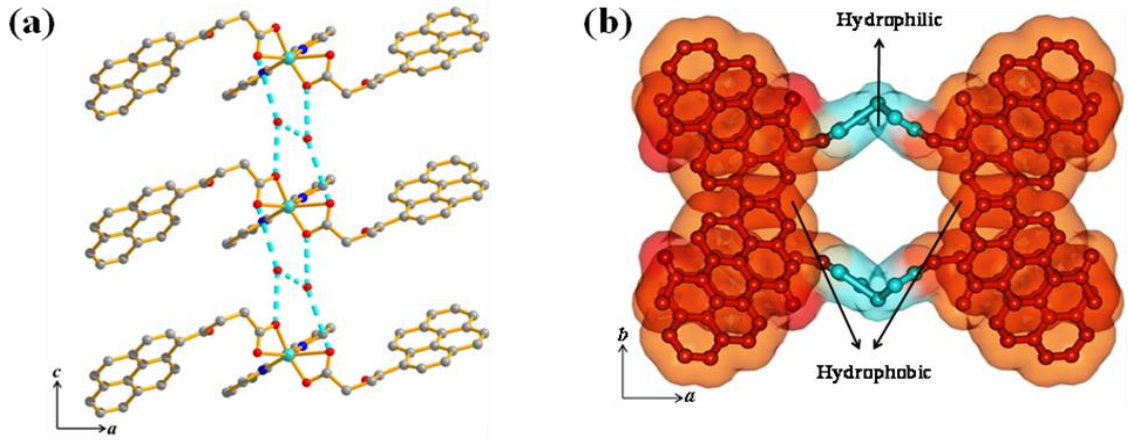

Figure 5: View of H-bonded water molecules in **2** (cyan dotted lines show H-bonds); (b) Hydrophobic and philic sites in pore of **2**.

Table 1: Crystal data and structure refinement parameters of **1** and **2**.

Parameters	**1**	**2**
Empirical formula	$C_{40}H_{30}O_8Cd$	$C_{50}H_{42}N_2O_{10}Zn$
Formula weight	751.05	888.18
Crystal system	Monoclinic	Monoclinic
Space group	*C*2/*c*	*C*2/*c*
a, Å	53.310(5)	30.904(5)
b, Å	5.4433(5)	16.245(5)
c, Å	11.0524(9)	8.387(5)
β, deg	97.600(6)	90.170(5)
V, Å^3	3179.0(5)	4211(3)
Z	4	4
T, K	293	293
μ,mm^{-1}	0.745	0.648
D_{calcd},g/cm^3	1.569	1.401
F (000)	1528	1832
Reflections [$I>2\sigma(I)$]	2791	2529
Unique reflections	3811	5111
Total reflections	15293	24178
R_{int}	0.097	0.090
GOF on F^2	1.02	0.85
$R_1[I>2\sigma(I)]^a$	0.0661	0.0571
R_w[all data]^b	0.2170	0.1680
$\Delta\rho$ max/min [e Å^{-3}]	2.39, -2.30	0.93, -0.38

$^aR_1 = \sum||F_o|-|F_c||/\sum|F_o|$; $^bR_w = [\sum\{w(F_o^2-F_c^2)^2\}/\sum\{w(F_o^2)^2\}]^{1/2}$

Table 2: Selected bond distances (Å) for **1**

Cd1-O1	2.321(4)	Cd1-O2	2.355(4)
Cd1-O4	2.220(4)	Cd1-O2_a	2.355(4)
Cd1-O1_a	2.321(4)	Cd1-O4_a	2.220(4)

a= 2-x,y,1/2-z

Table 3: Selected bond angles (°) for **1**

O1-Cd1-O2	55.59(13)	O1-Cd1-O4	144.98(12)
O1-Cd1-O2_a	107.55(14)	O1-Cd1-O1_a	84.61(14)
O2-Cd1-O2_a	159.48(15)	O1-Cd1-O4_a	97.47(15)
O1_a -Cd1-O4	97.47(15)	O2-Cd1-O4	91.07(14)
O4-Cd1-O4_a	100.18(16)	O1_a-Cd1-O2	107.55(14)
O2_a-Cd1-O4	102.12(15)	O2-Cd1-O4_a	102.12(15)
O1_a-Cd1-O2_a	55.59(13)	O1_a-Cd1-O4_a	144.98(12)
O2_a-Cd1-O4_a	91.07(14)		

Table 4: Selected bond distances (Å) for **2**

Zn1-O1	1.973(3)	Zn1-O2	2.501(3)
Zn1-N1	2.093(3)	Zn1-O1_a	1.973(3)
Zn1-O2_a	2.501(3)	Zn1-N1_a	2.093(3)

a= -x,y,1/2-z

Table 5: Selected bond angles (°) for **2**

O1-Zn1-O2	57.28(9)	O1-Zn1-N1	103.94(10)
O1-Zn1-O1_a	138.08(11)	O1-Zn1-O2_a	97.63(10)
O1-Zn1-N1_a	108.18(10)	O2-Zn1-N1	153.44(9)
O1_a-Zn1-O2	97.63(10)	O2-Zn1-O2_a	110.51(10)
O2-Zn1-N1_a	89.21(10)	O1_a-Zn1-N1	108.18(10)
O2_a-Zn1-N1	89.21(10)	N1-Zn1-N1_a	78.81(11)
O1_a-Zn1-O2_a	57.28(9)	O1_a-Zn1-N1_a	103.94(10)
O2_a-Zn1-N1_a	153.44(9)		

a= -x,y,1/2-z

2.3.3 PXRD Analysis and Thermal Stability

To verify the thermal stability of **2** TG analysis was carried out and it shows release of guest water molecules at RT only and the desolvated phase is stable upto 200 °C (Figure 6a). This high thermal stability indicates very strong intermolecular association. The desolvated framework was prepared at 80 °C under reduced pressure (10^{-1} Pa) and PXRD pattern of the same shows subtle changes compared to that of as-synthesized pattern (Figure 6b). Such change suggests structural rearrangement and this can be attributed to the presence of van der Waals forces which is comparatively weaker than coordination bonds.

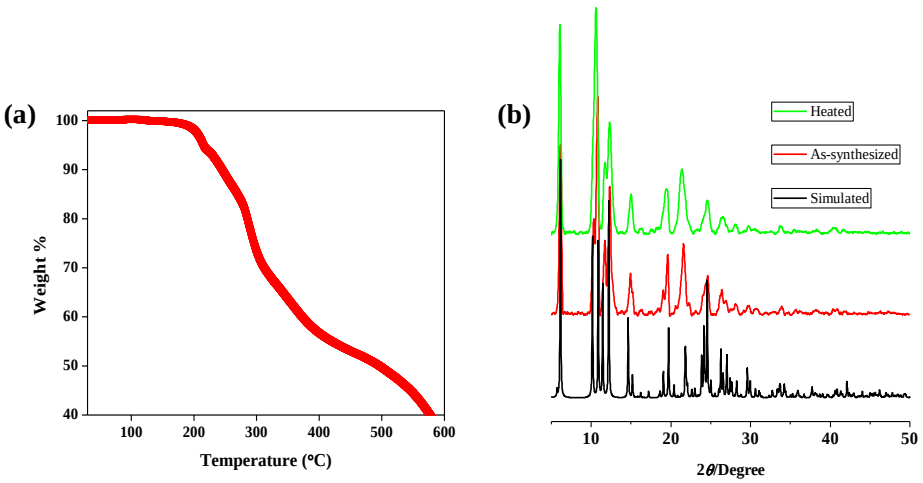

Figure 6: (a) TG analysis curve of **2**; (b) PXRD patterns of different phases of compound **2**: simulated, as-synthesized and desolvated at 80 °C.

2.3.4 Gas and Solvent Vapour Adsorption Studies

To measure the porosity of **2** we have carried out N_2 adsorption of the desolvated **2** at 77 K and recorded a type-II adsorption profile (Figure 7a). Interestingly, CO_2 adsorption profile at 195 K shows stepwise uptake and saturates at ~ 28 mLg^{-1} (Figure 7a). At P/P_0 ~ 0.1 a sudden rise in the uptake profile (step) indicates a structural rearrangement and this sort of CO_2 adsorption characteristics are found in flexible frameworks.[15] Such structural transformations with large quadrupolar CO_2 molecules can be attributed to specific interactions of CO_2 with the pore surface decorated with carboxylate oxygen as well as aromatic π electron cloud. We also carried out solvent vapour adsorption of **2** to realize any such flexibility or structural change (Figure 7b). Water and methanol vapour adsorption profiles at 298 and 293 K showed stepwise uptake profiles. Water vapour uptake increases slowly at low pressure but at P/P_0 ~ 0.7 shows a distinct step to reach the final uptake amount of ~ 3.7 molecules/formula. Desorption profile takes a different route leading to a large hysteresis. In case of methanol vapour initial uptake is very low but a step appears at P/P_0 ~ 0.24 with uptake amount of 0.55 molecules/formula. The second step appears at P/P_0 ~ 0.68 and the uptake amount is 2 molecules/formula. Finally it adsorbs 2.6 molecules/formula. This behaviour indicates presence of hydrophobic and-philic sites on the pore surface. Initially the water vapour interacts with pyrene decorated hydrophobic sites and in higher pressure region it increases sharply due to the interaction with carboxylate oxygens (hydrophilic). In case of methanol, the initial uptake is even lower due to increased molecular size and hydrophobic interaction. But the step appears at comparatively lower pressure to that of water as methanol is less hydrophilic compared to water.

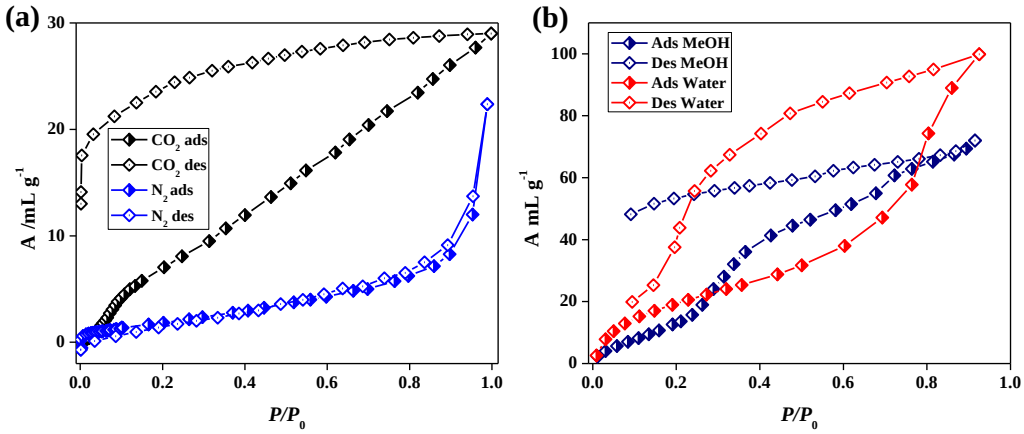

Figure 7: (a) CO_2 (195 K) and N_2 (77 K) adsorption profiles for **2**; (b) H_2O and MeOH vapour adsorption profiles of **2** at 298 and 293 K, respectively.

2.3.5 Excimer Emission and Light Harvesting

Both **1** and **2** contain pyrene as a chromophore and hence an intense emission characteristic was anticipated. Upon excitation at 400 nm **1** shows a broad emission with maxima at 500 nm (Figure 8a-8b). Such huge red shift compared to that of oxo-pba monomer indicates formation of a pyrene excimer and this is also clear from the crystal structure of **1** where two pyrene moieties from two neighbouring complexes are in close proximity (Figure 8c).

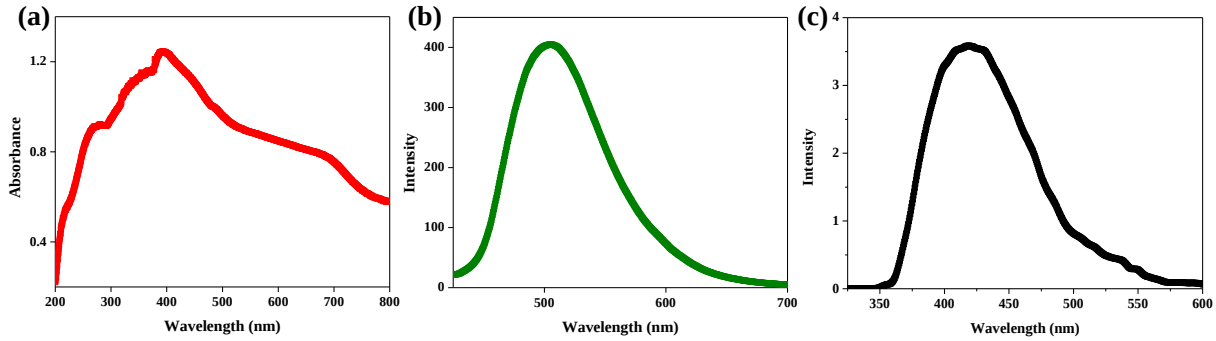

Figure 8: (a) Absorbance spectrum of **1** in solid state; (b) Emission spectrum of **1** in solid state upon excitation at 400 nm; (c) Emission spectrum of oxo-pba in methanol upon excitation at 310 nm.

Similar to **1**, emission spectrum of **2** also shows a broad featureless band with a maxima at 490 nm (λ_{ex} = 400 nm) (Figure 9a-9b). Thus this cyan emission can be attributed to the intermolecular pyrene excimer formation. From crystal structure it is evident that the pyrene rings, aligned in close proximity, are in appropriate spatial disposition to make such excited state dimer (excimer).

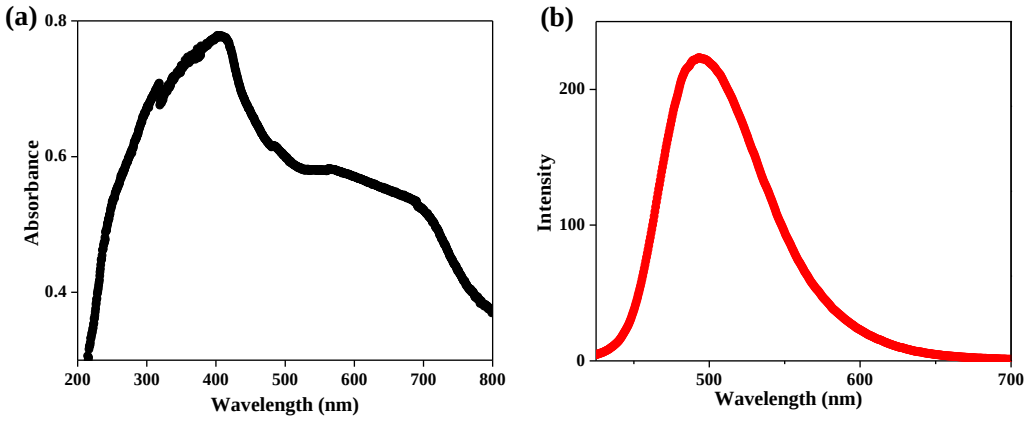

Figure 9: (a) Absorbance spectrum of **2** in solid state; (b) Emission spectrum of **2** upon excitation at 400 nm.

The structural flexibility, porosity and bright cyan colour excimer emission of compound **2** incited us to explore the light harvesting properties by encapsulating a suitable acceptor dye non-covalently. We selected acridine orange (AO) dye as a guest as the absorbance maximum of acridine orange (AO) dye (λ_{max} = 490 nm) overlaps with the emission spectrum of **2** and the molecular dimensions of AO matches well with the pore size of **2** (Figure 10a-10b). PXRD pattern of **2@AO** is almost similar with **2** shows change of Bragg intensity and slight shifting of some peaks compared to desolvated **2**, suggesting structural reorganization after encapsulation of AO (Figure 11). ^{1}H-NMR of **2@AO** after disintegrating in DCl shows the presence of AO and elemental analysis suggests that 0.08 molecules of AO is included per formula of **2** (Figure 12). The presence of four –CH_3 groups and large aromatic core of AO would help facile inclusion in the hydrophobic pore of **2**.

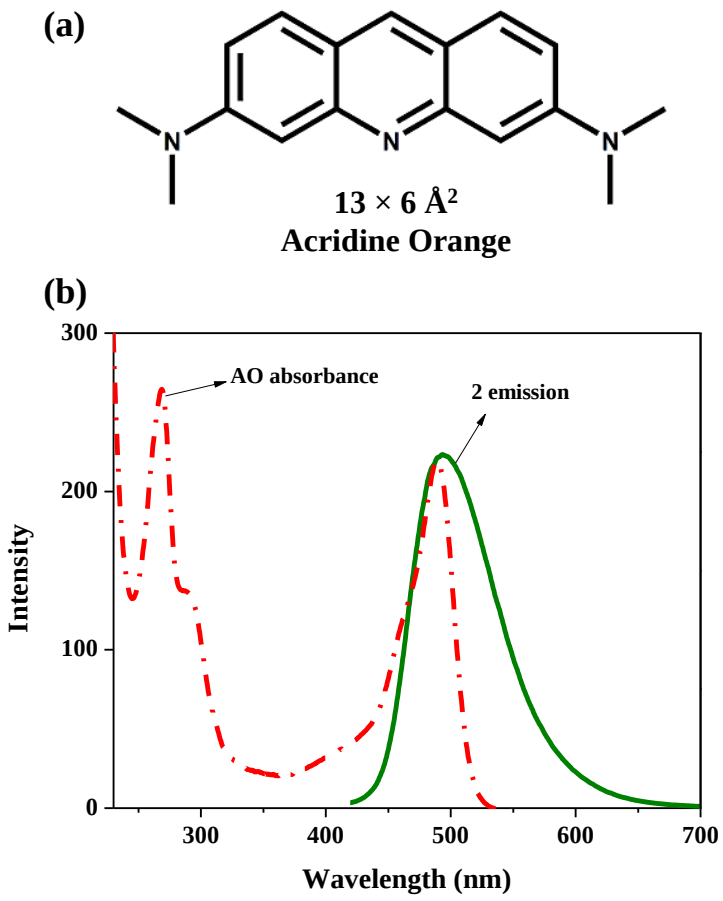

Figure 10: (a) Molecular dimension of acridine orange (AO); (b) Overlap of emission spectrum of **2** and absorbance spectrum of AO dye in methanol.

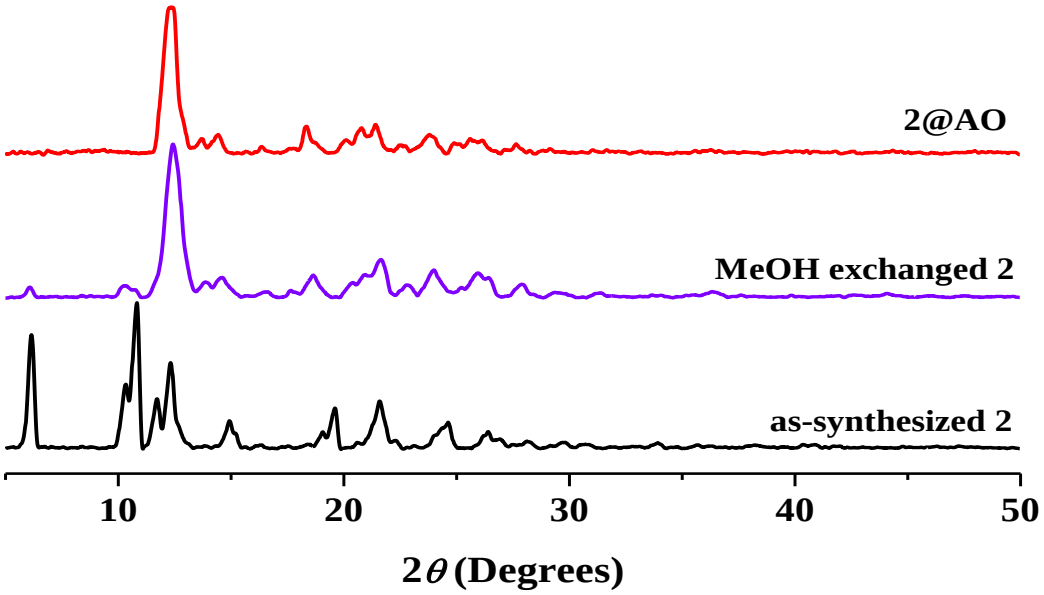

Figure 11: PXRD patterns of as-synthesized **2**, MeOH exchanged **2** and **2@AO**.

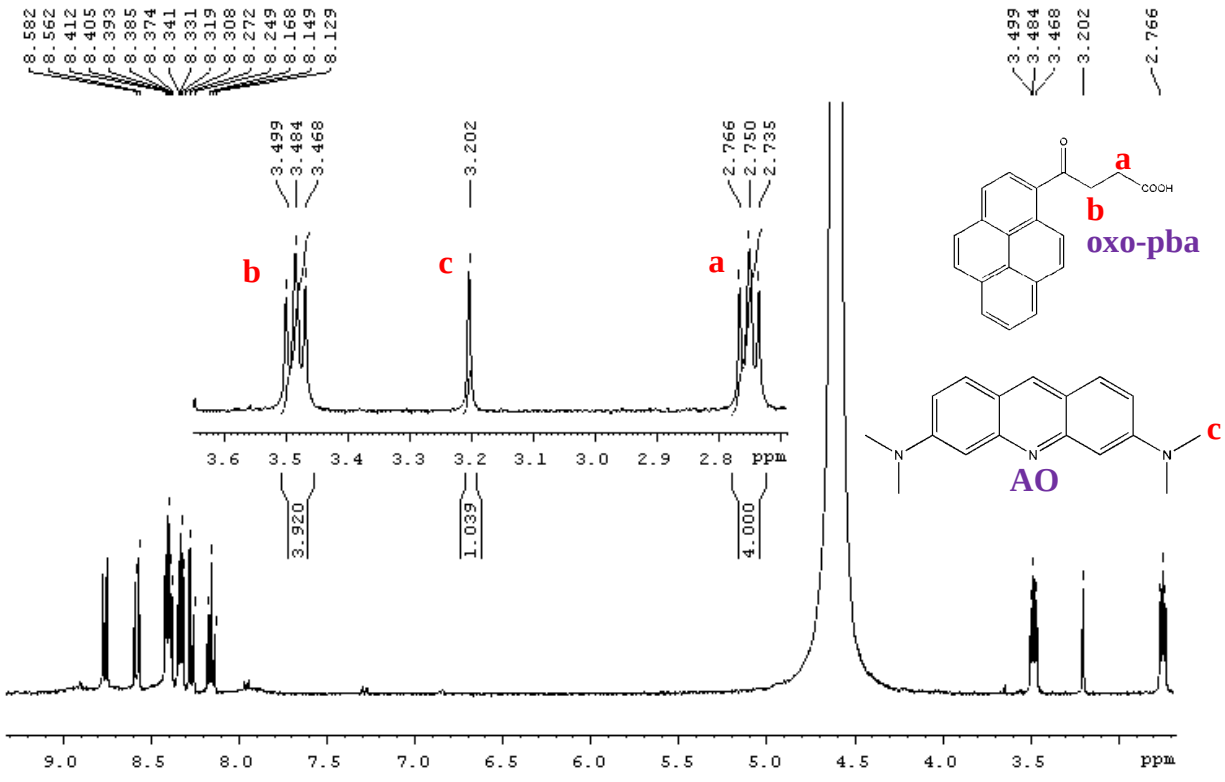

Figure 12: ^{1}H-NMR spectrum of **2@AO** dissolved in DCl/DMSO.

A distinct absorption band around 500 nm further concludes the inclusion of AO (Figure 13a). When the AO loaded compound **2@a** is selectively excited at 400 nm, the excimer emission at 490 nm is almost quenched and strong emission related to AO with maxima at 550 nm appeared (Figure 13b). This suggests an efficient Förster resonance energy transfer (FRET) from framework to non-covalently encapsulated dye molecules. The energy transfer is further supported by the excitation spectrum. Excitation spectrum monitored at AO emission (575 nm) shows a maximum at 410 nm which retells the presence of FRET process (Figure 13c). The perfect spectral overlap of framework emission and AO absorbance creates an efficient FRET process. Further a direct excitation of **2** at 500 nm shows lesser intensity compared to when excited at 400 nm (Figure 13b). This also describes an efficient FRET from framework to the adsorbed AO dye molecules. To further elucidate the energy transfer process we carried out time-resolved single-photon counting experiments of **2@AO** with 405 nm excitation and monitored the emission at 470 (λ_{max} of donor) and 600 nm (for acceptor) (Figure 14a-b). The life-time decreased significantly when monitored at 470 nm (~ 1.9 ns) compared to that of only framework **2** (~ 11.5 ns) and at 600 nm we observed sufficiently high life-time (~ 5.1 ns) compared to only AO dye. This shows that the framework emission energy has been consumed by the acceptor dye leading to decrease of life-time when observed at 470 nm.

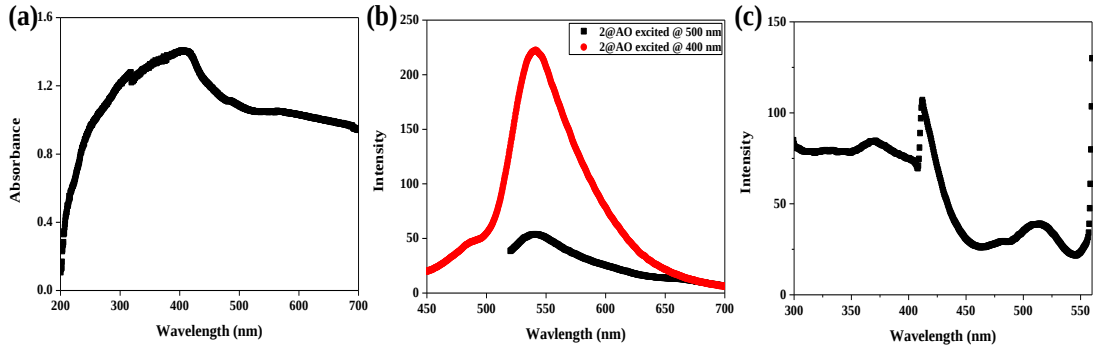

Figure 13: (a) Absorbance spectrum of **2@AO**; (b) Emission spectrum of **2@AO** upon excitation at 400 and 500 nm; (c) Excitation spectrum of **2@AO** monitored at 575 nm.

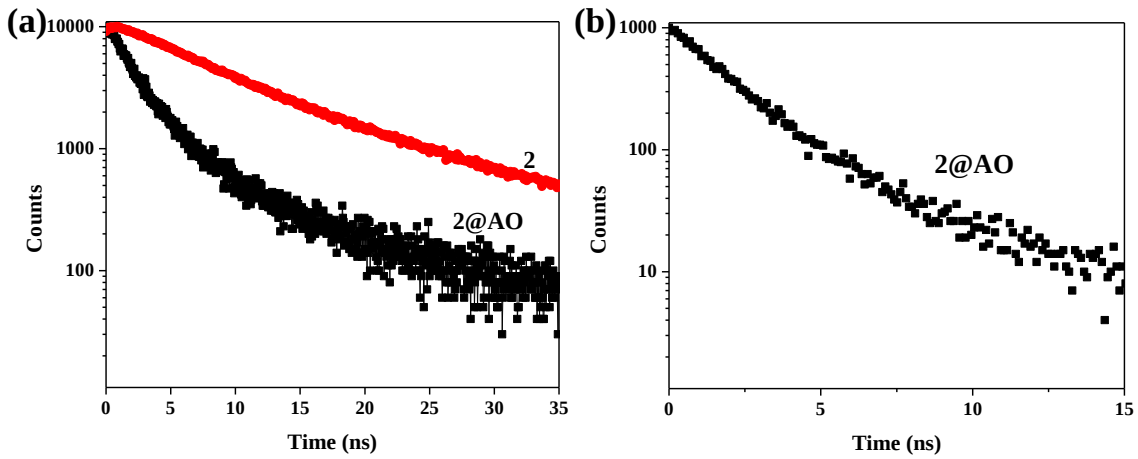

Figure 14: (a) Fluoroscence life time profiles of **2** and **2@AO** monitored at 470 nm upon excitation at 405 nm; (b) Fluoroscence life time profiles of **2@AO** monitored at 600 nm upon excitation at 405 nm.

2.4 Conclusions

In conclusion, a crystal engineering approach and supramolecular design have been implemented to construct a novel 3D supramolecular luminescent porous structure based on a molecular complex {Zn(oxo-pba)$_2$(bpy)} as a building unit. We have shown how a small change in the metal coordination sphere acts as structure directing force to generate an unprecedented structure. Such porous structure with supramolecular channels could be formed due to the perfect spatial organization of pyrene aromatic rings and this is directed by the bpy coordination. The framework is thermally stable and shows sufficient flexibility realized from adsorption studies. Further, presence of hydrophobic and -philic pore surface also influences the solvent vapour adsorption profiles. This framework shows bright cyan colored pyrene excimer emission and that has been exploited for light harvesting application by encapsulating a suitable acceptor dye AO based on FRET process.

2.5 References

1 (a) Y. Cui, Y. Yue, G. Qian and B. Chen, *Chem. Rev.*, 2012, **112**, 1126; (b) M. Nishio, N. Motokawa, M. Takemura and H. Miyasaka, *Dalton Trans.*, 2013, **42**, 15898.

2 (a) A. Banerjee, A. Sahana, S. Guha, S. Lohar, I. Hauli, S. K. Mukopadhyay, J. S. Matalobos and D. Das, *Inorg. Chem.*, 2012, **51**, 5699; (b) D. Thirion, M. Romain, J. R. Berthelot and C. Poriel, *J. Mater. Chem.*, 2012, **22**, 7149; (c) G. Zhang, H. –S.Chou, X. Jiang, P. Sun and C. –H. Cheng, *Organic Electronics*, 2010, **11**, 1165.

3 R. Haldar, K. V. Rao, S. J. George and T. K. Maji, *Chem. Eur. J.*, 2012, **18**, 5848.

4 (a) N. B. Shustova, B. D. McCarthy and M. Dincă, *J. Am. Chem. Soc.*, 2011, **133**, 20126; (b) C. Y. Sun, X. L. Wang, X. Zhang, C. Qin, P, Li, Z. M. Su, D. X. Zhu, G. G. Shan, K. J. Shao, H. Wu and J. Li, *Nat. Comm.*, 2013, **4**, 1.

5 T. M. Figueira-Duarte and K. Müllen, *Chem. Rev*, 2011, **111**, 7260.

6 B. D. Wagner, G. J. McManus, B. Moulton and M. J. Zaworotko, *Chem Commun.*, 2002, 2176.

7 L. Sun, H. Xing, Z. Liang, J. Yu and R. Xu, *Chem. Commun.*, 2013, **49**, 11155.

8 *SMART (V 5.628), SAINT (V 6.45a), Xprep, SHELXTL*; Bruker AXS Inc. Madison, Wisconsin, USA, 2004.

9 G. M. Sheldrick, *Siemens Area Detector Absorption Correction Program*, University of Götingen, Götingen, Germany, 1994.

10 A. Altomare, G. Cascarano, C. Giacovazzo and A. Gualaradi, *J. Appl. Crystallogr.*, 1993, **26**, 343.

11 G. M. Sheldrick, *SHELXL-97, Program for Crystal Structure Solution and Refinement*, University of Götingen, Götingen, Germany, 1997.

12 (a) A. L. Spek, *J. Appl. Crystallogr.*, 2003, **36**, 7; (b) L. J. Farrugia, WinGX-A Windows Program for Crystal Structure Analysis, *J. Appl. Crystallogr.*, 1999, **32**, 837.

13 The sizes of the channels were calculated considering the van der Waals radii of the atoms.

14 A. L. Spek, *J. Appl. Crystallogr.*, 2003, **36**, 7.

15 (a) R. Haldar, S. K. Reddy, V. M. Suresh, S. Mohapatra, S. Balasubramanian and T. K. Maji, *Chem. Eur. J.*, 2014, DOI: 10.1002/chem.201303610; (b) D. Tanaka, K. Nakagawa, M. Higuchi, S. Horike, Y. Kubota, T. C. Kobayashi, M. Takata and S. Kitagawa, *Angew. Chem. Int. Ed.*, 2008, **47**, 3914.

Chapter: 3

Colour tunability and white light emission in Tb^{3+} coordination frameworks by Eu^{3+} doping

Summary

This chapter details the solvothermal synthesis of two new isomorphous flexible supramolecular Eu^{3+} and Tb^{3+} based 3D frameworks, $\{[Eu(L)(DMF)(H_2O)]\cdot 3H_2O\}_n$ (**1**) and $\{[Tb(L)(DMF)(H_2O)]\cdot 3H_2O\}_n$ (**2**). A new flexible tricarboxylic acid linker H_3L (4,4′,4″-[1,3,5-phenyl-tri(methoxy)]-tris-benzoic acid) having emission in the blue region is used for their synthesis. The metal center in each case is eight coordinated; six oxygens from L and two other oxygens are from DMF and water molecule. Dimeric secondary building units (SBU) are formed using metal ion and carboxylate groups which are extended by the L linker along *ac* plane. The 1D chains formed by the help of L shaped linker which are stacked along *a*-axis to form 1D channels occupied by guest water molecules. The desolvated framework shows selective adsorption of CO_2 over CH_4 at 195 K. RGB (red-green-blue) concept is applied to get white light emission from the framework by proper stoichiometric mixing of Tb^{3+} and Eu^{3+} in $\{[Tb_{1-x}Eu_x(L)(DMF)(H_2O)]\cdot 3H_2O\}_n$. Different ratios of Tb^{3+} and Eu^{3+} lead to other emission colours also, such as green, pink, orange and red.

3.1 Introduction

The development of solid state light-emitting materials have been extensively studied in recent years because of their applications in biomedical imaging, photodynamic therapy, color display and solid state lighting.[1] Since the discovery of white light emitting diode (WLEDS), a variety of solid state materials like inorganic oxides, nitrides and quantum dots, discrete organic molecules, and polymers have been discovered with aim to replace the most widely used mercury containing fluorescent lighting.[2] Among the three different type of white light phosphors, trichromatic approaches in which blue, green and red light emitting components are introduced into the resulting white light emitting materials are superior compared to the monochromatic (that emits entire visible regions) and dichromatic (that emit in blue and yellow regions) due to the finer color rendering properties and high quantum efficiencies. Thus design and synthesis of such materials have attracted significant attention. In this context, lanthanide based materials are of paramount importance as they exhibit interesting photoluminescence, magnetic, and electronic properties originating from the 4f electronic configuration. Trivalent lanthanide ions such as Tb^{3+}, Eu^{3+}, Sm^{3+}, Er^{3+} and Yb^{3+} show spectrally narrow line like emission of different colors and their weak emission intensities due to low absorption coefficient can be overcome in complexation with π-conjugated organic ligands via 'antenna effect'.[3] Hence, extended porous lanthanide-coordination polymers are very promising luminescence materials and have shown potential application in LEDs, sensing, catalysis and as opto-electronic/magnetic materials.[4] However, compared to d-block metal ions, design and synthesis of lanthanide-porous coordination polymers (Ln-PCPs) are less explored and that can be attributed to the difficulty in controlling the large coordination sphere which results in a highly stable condensed structure.[5] Furthermore developing suitable Ln-PCPs with tunable emission colour, in particular capable of generating white light for WLED materials is a challenging task. Although such hybrid materials would show greater flexibility, high mechanical properties and easy processibility compared to other polymer materials.[6]

In this regard, we envisioned a new organic ligand (H_3L) with C_3 symmetry which shows bright blue emission (Scheme 1). This linker has flexible backbone of –O-CH_2- and also presence of aromatic rings makes it a good antenna chromophore for lanthanides. In this chapter we have shown the design and synthesis of two new isomorphous flexible supramolecular Eu^{3+} and Tb^{3+} based 3D frameworks,$\{[Eu(L)(DMF)(H_2O)]\cdot 3H_2O\}_n$ (**1**)

and {[Tb(L)(DMF)(H_2O)]·3H_2O}$_n$(**2**). Framework **1** has a porous structure with 1D distorted rectangular shaped channels and the desolvated framework selectively adsorbs CO_2 over CH_4 at 195 K. Proper stoichiometric mixing of Tb^{3+} and Eu^{3+} in {[$Tb_{1-x}Eu_x$ (L)(DMF)(H_2O)]·3H_2O}$_n$ (x= 0.01 (**2a**), 5.9 (**2b**), 6.7 (**2c**), 7.5 (**2d**), 18.4 (**2e**) and 37.8 (**2f**)) frameworks show different emission colours (green, pink, orange and red) and also bright white light emission.

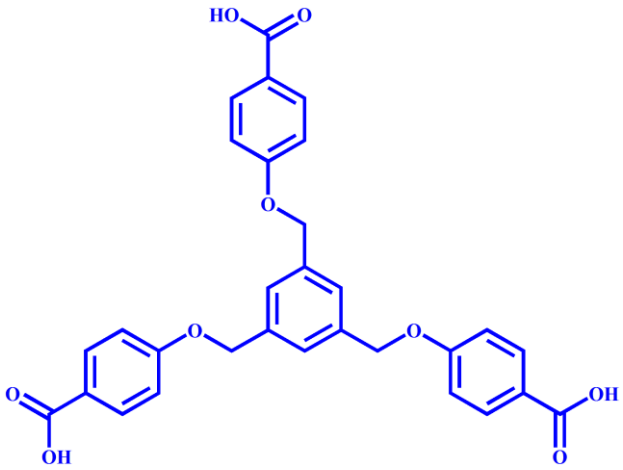

Scheme 1: Chemical structure of H_3L linker.

3.2 Experimental Section

3.2.1 Materials

All the reagents were commercially available and used as provided without further purification. Eu^{3+} and Tb^{3+} salts were obtained from Alfa Aesar and Sigma Aldrich respectively, methyl-4-hydroxy benzoate from SDFCL, 1,3,5-tris(bromomethyl)benzene from Sigma Aldrich and potassium carbonate from Chemical Drug House.

3.2.2 Physical Measurements

Elemental analysis was carried out using a Thermo Fischer Flash 2000 Elemental Analyzer. IR spectra were recorded on a Bruker IFS 66v/S spectrophotometer using KBr pellets in the region 4000–400 cm^{-1}. Thermogravimetric analysis (TGA) was carried out (Metler Toledo) in nitrogen atmosphere (flow rate = 50 mL min^{-1}) in the temperature range 30–700 °C (heating rate = 3 °C min^{-1}). Powder X-ray diffraction (PXRD) pattern of the products were recorded on a Bruker D8 Discover instrument using Cu−Kα radiation. Electronic absorption spectra were recorded on a Perkin Elmer Lambda 900 UV-VIS-NIR

Spectrometer and PL spectra were taken with Perkin-Elmer model LS 55 luminescence spectrometer. ^{1}H-NMR spectra were obtained with a Bruker AVANCE 400 (400 MHz) Fourier transform NMR spectrometer with chemical shifts reported in parts per million (ppm). Fluorescence decay was recorded in a time correlated single photon counting spectrometer of Horiba-Jobin Yvon with 350-450 nm picosecond Ti-saphhire laser. Energy dispersive analysis of X-rays (EDAX) was carried out using Leica-S440I field emission scanning electron microscope (FESEM).

3.2.3 X-ray Crystallography

X-ray single crystal structural data of **1** was collected on a Bruker Smart-CCD diffractometer equipped with a normal focus, 2.4 kW sealed tube X-ray source with graphite monochromated Mo-Kα radiation (λ = 0.71073 Å) operating at 50 kV and 30 mA. The program SAINT[7] was used for integration of diffraction profiles and absorption correction was made with SADABS[8] program. All the structures were solved by SIR 92[9] and refined by the full matrix least-squares method using SHELXL-97.[10] All the hydrogen atoms were fixed by HFIX and placed in ideal positions. Potential solvent accessible area or void space was calculated using the PLATON multipurpose crystallographic software.[11] All crystallographic and structure refinement data of **1** is summarized in Table 1. Selected bond lengths and angles for **1** are given in Table 2-3. All calculations were carried out using PLATON and WinGX system, Ver 1.70.01.[12]

3.2.4 Adsorption Measurements

Adsorption isotherms of N_2 (77 K and 195 K) and CO_2 (195 K) were recorded using the desolvated sample of **1** (**1′**) by using a QUANTACHROME QUADRASORB-SI analyzer. In the sample tube, the adsorbent sample (**1′**) (100−150 mg) were placed which had been prepared at 180 °C under a 1×10^{-1} Pa vacuum for about 12 h prior to measurement of the isotherms. Helium gas (99.999% purity) at a certain pressure was introduced in the gas chamber and allowed to diffuse into the sample chamber by opening the valve. The amount of gas adsorbed was calculated from the pressure difference ($P_{cal} - P_e$), where P_{cal} is the calculated pressure with no gas adsorption and P_e is the observed equilibrium pressure. All the operations were computer controlled and automatic.

3.2.5 Syntheses

3.2.5.1 Synthesis of 4,4′,4″-[1,3,5-phenyl-tri(methoxy)]-tris-benzoic acid (H_3L)

Methyl-4-hydroxy benzoate (1 g, 6.57 mmol), potassium carbonate (2.890 gm, 20.1 mmol) and potassium iodide (0.085 g, 0.51 mmol) were heated in 30 mL DMF at 100 °C for 2 hours in nitrogen atmosphere. A solution of 1,3,5-Tris(bromomethyl)benzene (0.500 g, 1.4 mmol) in 20 mL DMF was then added dropwise to the above heated mixture. The mixture was then heated for 4 hours at 100 °C. After cooling to room temperature, 100 mL of distilled water was added to it. The precipitate formed was filtered, washed with cold distilled water and air dried to get white solid of 4,4′,4″-[1,3,5-phenyl-tri(methoxy)]-tri-methyl benzoate. To 4,4′,4″-[1,3,5-phenyl-tri(methoxy)]-tri-methyl benzoate (for ~500 mg) 40 mL of MeOH and 1 g of sodium hydroxide dissolved in 10 mL of water was added in a RBF. The reaction mixture was then stirred at 50 °C for 12 hours. After cooling to room temperature, the solution was placed in an ice bath and acidified with 6N hydrochloric acid. The precipitate formed was then filtered, washed with cold distilled water and dried. The brownish solid of 4,4′,4″-[1,3,5-phenyl-tri(methoxy)]-tris-benzoic acid ligand was characterized by ^{1}H-NMR (Figure 1).

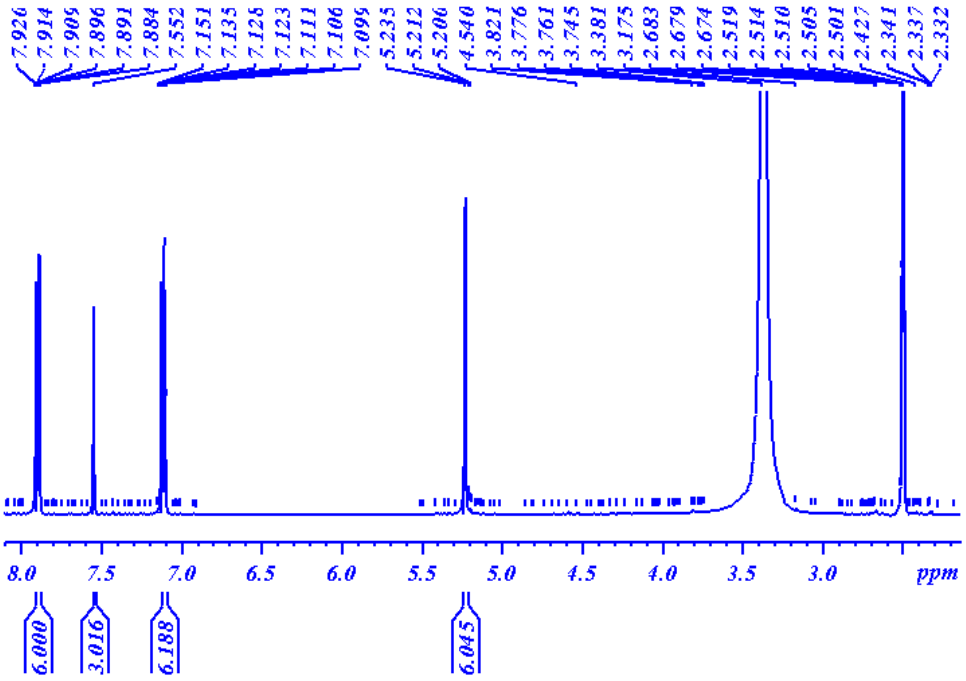

Figure 1: ^{1}H-NMR of 4,4′,4″-[1,3,5-phenyl-tri(methoxy)]-tris-benzoic acid in D_6-DMSO.

3.2.5.2 Synthesis of $\{[Eu(L)(DMF)(H_2O)]\cdot 3H_2O\}_n$ (1)

4,4′,4″-[1,3,5-phenyl-tri(methoxy)]-tris-benzoic acid (0.0396 g, 0.075 mmol) was dissolved in a solvent mixture of 3 mL DMF, 3 mL MeOH and 1.25 mL water in a glass vial. 0.75 mL of 10^{-5} M aqueous solution of $Eu(NO_3)_3\cdot 5H_2O$ was added to the vial before it was sealed and kept in an oil bath at 80 °C. Good quality transparent crystals of **1** were obtained after 24 hours which were washed with fresh methanol before single-crystal X-ray diffraction measurement.Yield of **1**: 59 %; Anal. Calcd.for $C_{33}H_{36}NO_{14}Eu$: C, 48.18; H, 4.38; N, 1.70. Found C, 50.913; H, 4.125; N, 1.803. FT-IR (KBr pellet, 4000−400 cm^{-1}) (Figure 2): 3240 (b), 2928 (m), 2894 (w), 1659 (s), 1603 (s), 1560 (s), 1506 (s), 1416 (s), 1308 (s), 1279 (w), 1254 (s), 1226 (s), 1171 (s), 1144 (m), 1103 (s), 1038 (s), 1002 (s), 910 (m), 865 (s), 787 (s), 724 (m), 700 (m), 676 (s), 647 (w), 612 (s), 562 (m), 535 (w), 510 (m), 469 (m), 436 (m), 414 (m).

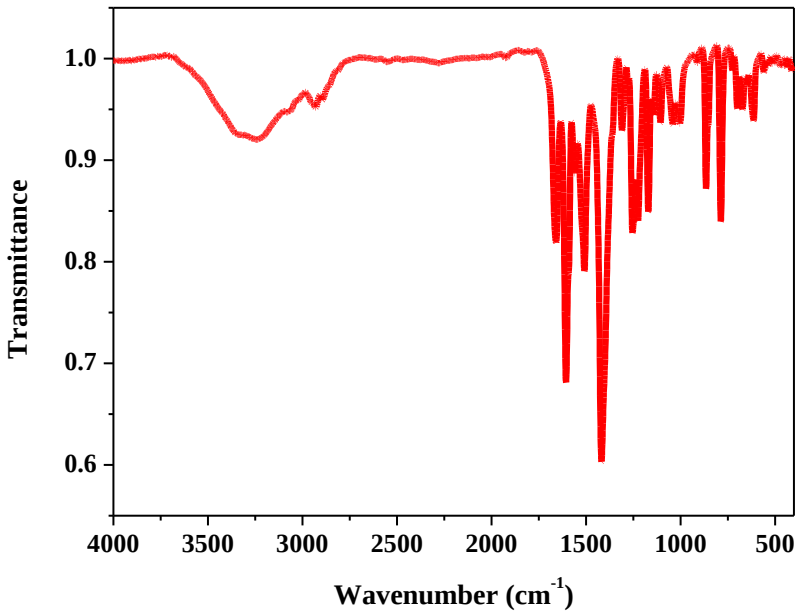

Figure 2: FT-IR spectrum of **1**.

3.2.5.3 Synthesis of $\{[Tb(L)(DMF)(H_2O)]\cdot 3H_2O\}_n$ (2)

Compound **2** was synthesized following the similar procedure except $Eu(NO_3)_3\cdot 5H_2O$ is replaced by $Tb(NO_3)_3\cdot 5H_2O$.Yield for **2**: 68 %; Anal. Calcd.for $C_{33}H_{36}NO_{14}Tb$: C, 47.77; H, 4.34; N, 1.68. Found C, 50.540; H, 4.072; N, 2.012. FT-IR (KBr pellet, 4000−400 cm^{-1}) (Figure 3): 3240 (b), 2928 (m), 2894 (w), 1659 (s), 1603 (s), 1560 (s), 1506 (s), 1416 (s), 1308 (s), 1279 (w), 1254 (s), 1226 (s), 1171 (s), 1144 (m),

1103 (s), 1038 (s), 1002 (s), 910 (m), 865 (s), 787 (s), 724 (m), 700 (m), 676 (s), 647 (w), 612 (s), 562 (m), 535 (w), 510 (m), 469 (m), 436 (m), 414 (m).

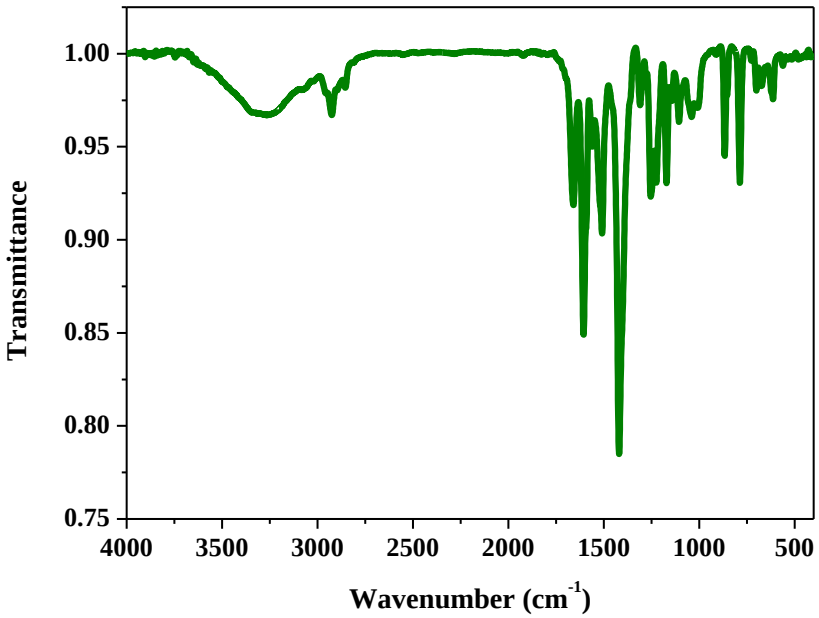

Figure 3: FT-IR spectrum of **2**.

3.2.5.4 Syntheses of $\{[Tb_{1-x}Eu_x(L)(DMF)(H_2O)]\cdot 3H_2O\}_n$ (x= 0.01 (2a), 5.9 (2b), 6.7 (2c), 7.5 (2d), 18.4 (2e) and 37.8 (2f))

The synthesis followed the similar procedure as that of compound **2**; just by replacing a certain amount of aqueous solution of $Tb(NO_3)_3\cdot 5H_2O$ with $Eu(NO_3)_3\cdot 5H_2O$ solution and keeping the total molar amount of the metal same (i.e. 0.75 mL of 10^{-5} M aqueous solution). Six different Eu^{3+} doped Tb^{3+} framework containing 37.8, 18.4, 7.5, 6.7, 5.9 and 0.01 atom% of Eu^{3+} was prepared. FT-IR (KBr pellet, 4000−400 cm^{-1}) (Figure 4):

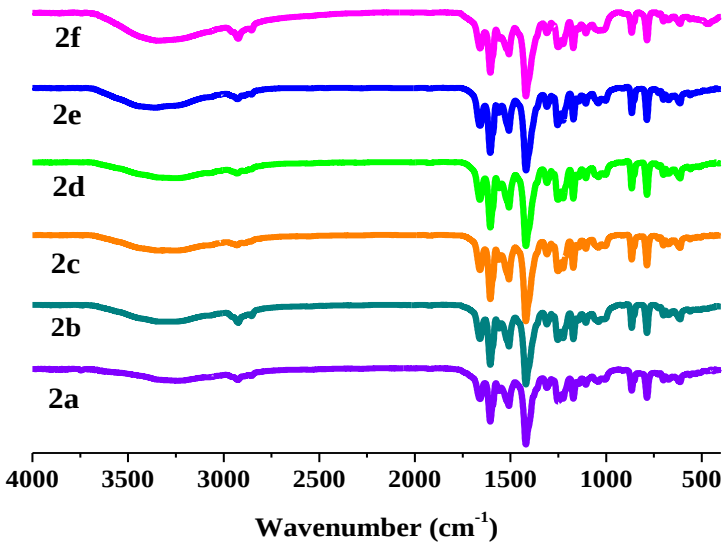

Figure 4: FT-IR spectra of **2a-f**.

3.3 Results and Discussion

3.3.1 Structural Description of $\{[Eu(L)(DMF)(H_2O)]\cdot 3H_2O\}_n$ (1)

Single crystal X-ray diffraction experiment suggests compound **1** crystallizes in a triclinic system with space group *P*ī and asymmetric unit contains a Eu^{3+}, one tricarboxylate linker L, two DMF and three water molecules. Each octa-coordinated Eu^{3+} centre is connected to six oxygen atoms (O1, O2, O3, O4, O5 and O8) from three different tricarboxylate linkers and other two coordination sites are occupied by a water (O6) and a DMF (O7) molecule (Figure 5a). Among the three carboxylate groups of L, one acts as a bridging carboxylate and holds two Eu^{3+} centers to form a dimeric cluster of $\{Eu_2(CO_2)_4(OCO)_2(DMF)_2(H_2O)_2\}$. The Eu···Eu distance within the dimeric cluster is 4.843 Å. The Eu^{3+}-O bond distances are in the range of 2.37(13)-2.50(11) Å. This unit is extended along *ac* plane by two L linker to form a 1D polymeric structure (Figure 5b). Further, these 1D chains stack along *ac* plane through hydrogen bonding interactions between coordinated water (O6) and carboxylate oxygens (O6-H···O1 ~ 2.713 Å and O6-H···O4 ~ 2.778 Å) to form a 2D structure (Figure 6a). These 2D sheets like structures stack over each other along *b* direction but leave no space in between the layers (Figure 5b). View along *a* direction shows 1D channels filled with guest water and coordinated DMF and water molecules. Removal of these guest and coordinated molecules creates a

distorted rectangular shaped pore with dimensions 6 × 4.5 $Å^2$ (Figure 6b). The total void space calculated using PLATON is 33.2 % of the total cell volume.

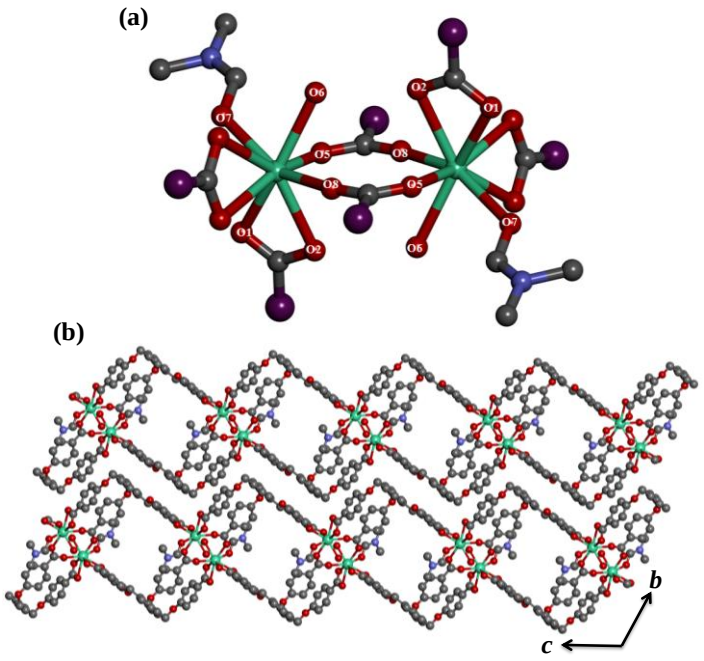

Figure 5: (a) Coordination environment of Eu^{3+} in **1**; (b) 1D polymers of **1** stack over each other.

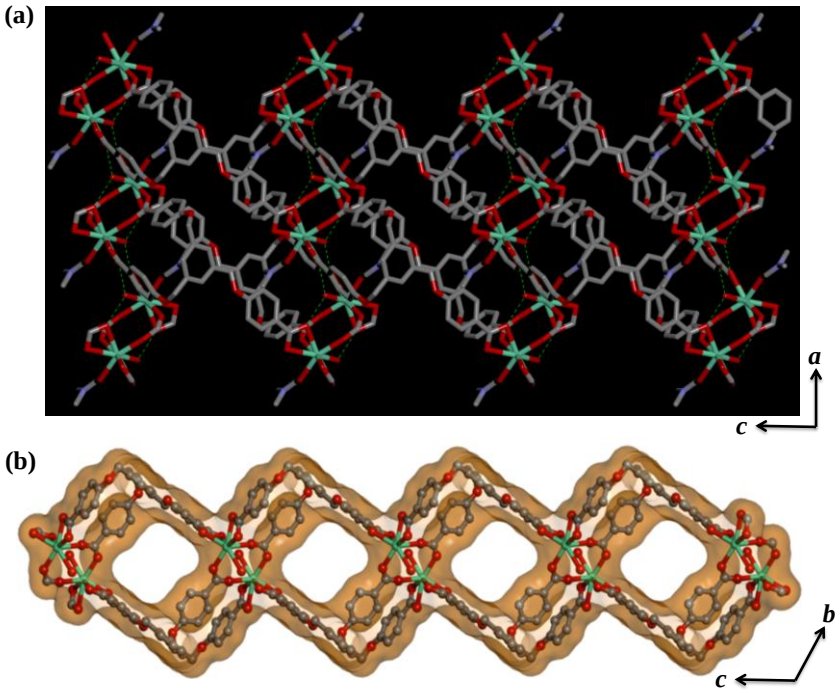

Figure 5: (a) View of the 2D structure formed via hydrogen bonding interactions (green dotted line); (b) View of the distorted rectangular pore windows.

Table 1: Crystal data and structure refinement parameters of **1**.

Parameters	**1**
Empirical formula	$C_{33}H_{36}NO_{14}Eu$
Formula weight	821.9
Crystal system	Triclinic
Space group	$P\bar{1}$
a, Å	8.569(5)
b, Å	14.434(8)
c, Å	14.471(9)
α, deg	98.739(4)
β, deg	95.779(4)
γ, deg	106.745(4)
V, Å^3	1674.20(18)
Z	2
T, K	293
μ,mm^{-1}	1.932
D_{calcd},g/cm^3	1.519
F (000)	766
Reflections [$I>2\sigma(I)$]	3489
Unique reflections	9431
Total reflections	25678
R_{int}	1.00
GOF on F^2	1.00
$R_1[I>2\sigma(I)]^a$	0.0989
R_w[all data]^b	0.3498
$\Delta\rho$ max/min [e Å^{-3}]	2.83, -2.38

$^aR_1 = \sum||F_o|-|F_c||/\sum|F_o|$; $^bR_w = [\sum\{w(F_o^2-F_c^2)^2\}/\sum\{w(F_o^2)^2\}]^{1/2}$

Table 2: Selected Bond Distances (Å) for **1**.

Eu-O1	2.450(13)	Eu-O2	2.500(11)
Eu-O3	2.453(12)	Eu-O4	2.464(13)
Eu-O5	2.292(13)	Eu-O6	2.421(12)
Eu-O7	2.424(14)	Eu-O8	2.371(13)

Table 3: Selected bond angles (°) for **1**.

O1-Eu-O2	52.6(4)	O5-Eu-O6	74.9(4)
O1-Eu-O3	115.4(4)	O5-Eu-O7	153.0(5)
O1-Eu-O4	140.0(4)	O5-Eu-O8	108.8(5)
O1-Eu-O5	89.7(5)	O6-Eu-O7	80.5(5)
O1-Eu-O6	79.4(4)	O6-Eu-O8	77.1(4)
O1-Eu-O7	74.6(5)	O7-Eu-O8	76.0(5)
O1-Eu-O8	144.8(4)	O2-Eu-O4	88.1(4)
O2-Eu-O7	104.9(5)	O2-Eu-O5	81.3(4)
O2-Eu-O8	156.7(4)	O2-Eu-O6	126.2(4)
O2-Eu-O3	78.4(4)	O3-Eu-O5	125.1(4)
O3-Eu-O4	53.5(4)	O3-Eu-O7	81.9(4)
O3-Eu-O6	152.9(4)	O4-Eu-O5	75.5(5)
O3-Eu-O8	78.7(4)	O4-Eu-O7	130.3(4)
O4-Eu-O6	129.4(4)	O4-Eu-O8	74.9(4)

3.3.2 PXRD Analysis and Thermal stability

The TG analysis of **1** suggests release of three guest water molecules (exp. 6 wt%, calc 6.57 wt%) in the temperature range of 35-110 °C (Figure 7). The next weight loss of 11 wt% in the temperature range of 160-280 °C corresponds to one coordinated DMF and one coordinated water (calc. 11.07 wt%). This desolvated state (**1′**) is stable upto 350 °C and further heating disintegrates the framework. We have examined the PXRD patterns of **1** after removing the guest water molecules and also the coordinated solvents (Figure 8). Heating at 100 °C releases only guest water molecules and the PXRD patterns of this phase suggest subtle structural change compared to that of as-synthesized **1**. Heating at

200 °C releases the coordinated solvents and this leads to further structural rearrangement as realized from the PXRD patterns.

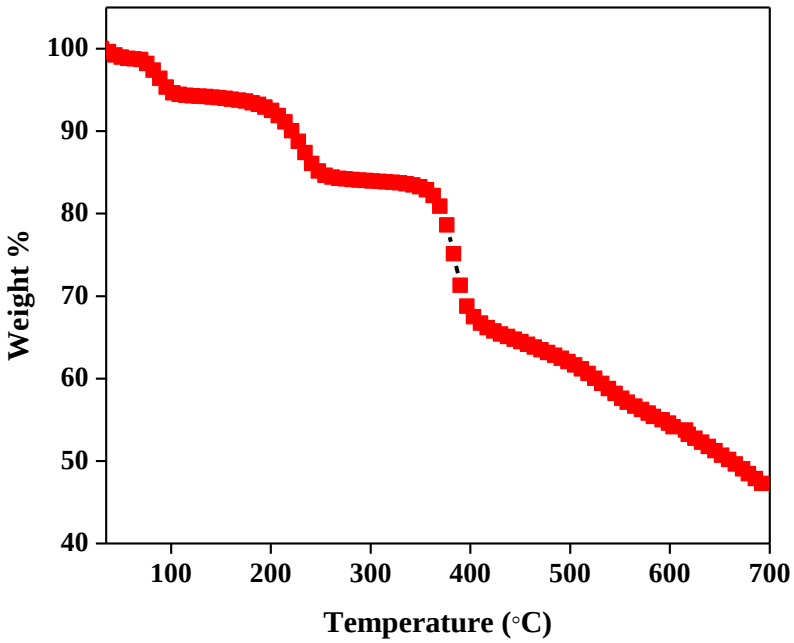

Figure 7: TGA profile of compound **1**.

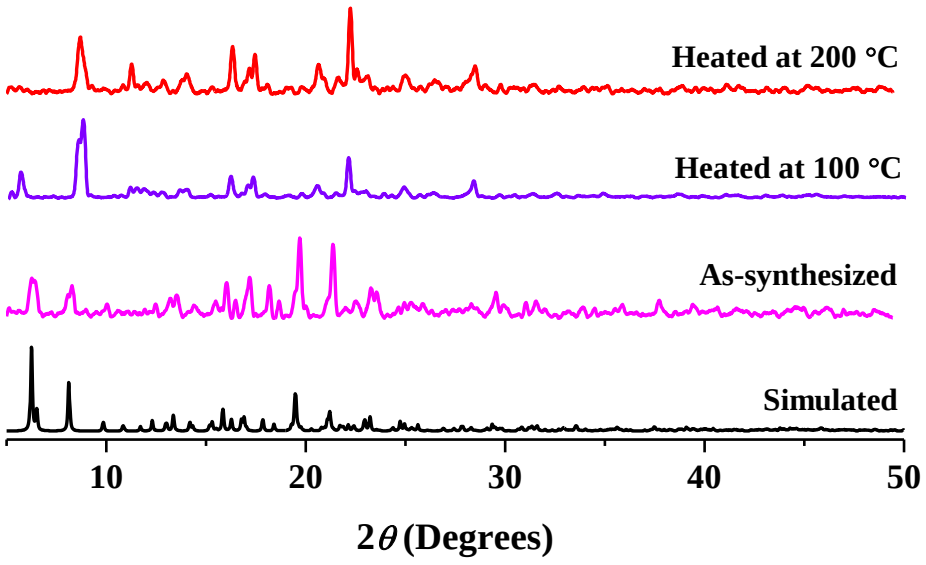

Figure 8: PXRD patterns of compound **1**.

In case of compound **2**, phase purity was checked from the PXRD pattern (Figure 9). We have found similar TGA profile to that in **1** indicating successive loss of guest

water molecules and coordinated water and DMF molecules. The desolvated phase (**2′**) is stable upto 360 °C (Figure10).

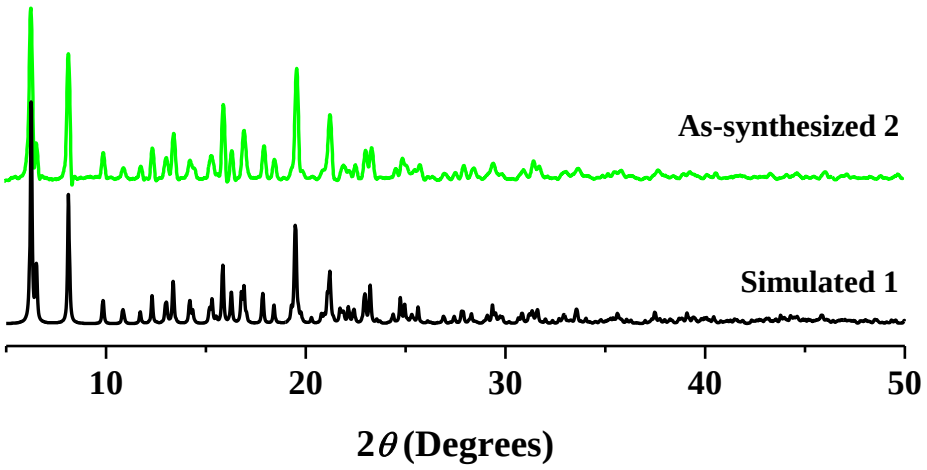

Figure 10: PXRD pattern of phase pure compound **2**.

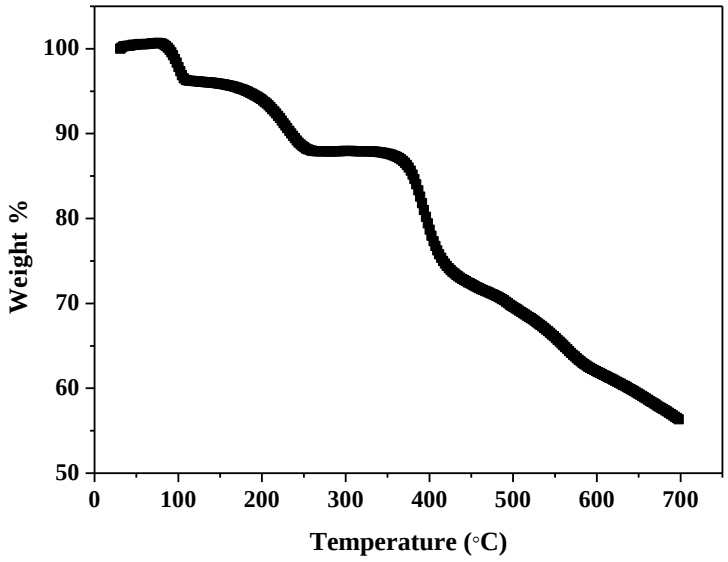

Figure 10: TGA profile of compound **2**.

3.3.3 Gas Adsorption Studies

To measure the porosity of **1′**, N_2 and CO_2 adsorption isotherms were measured at 77 and 195 K. Compound **1′** shows type II adsorption isotherm indicating only surface adsorption though the kinetic diameter of N_2 (3.64 Å) is smaller than the pore diameters

of **1** (Figure 11). Probably removal of guest molecules shrinks the pore aperture and perturbs the N_2 diffusion into the pores.

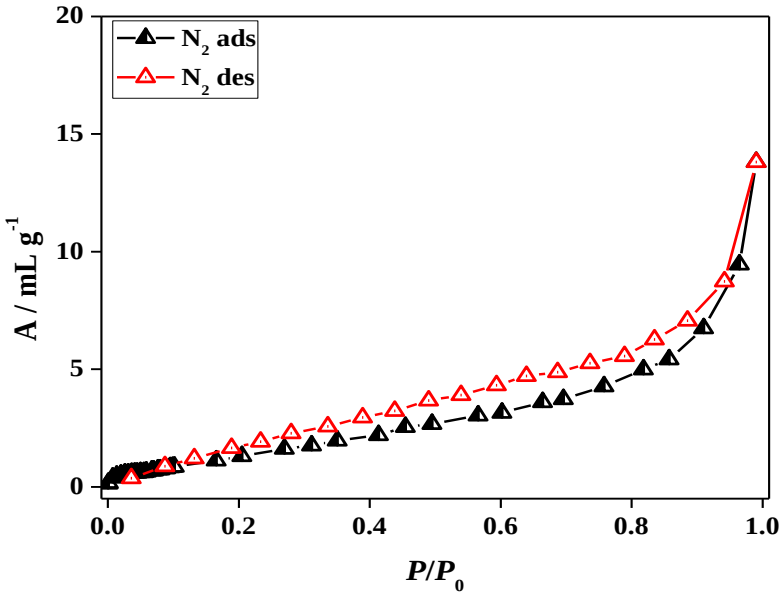

Figure 11: N_2 adsorption isotherm of **1′** at 77 K.

Surprisingly, at 195 K a sharp uptake of CO_2 was observed at low pressure. At very low pressure range a small step in the adsorption profile indicates structural rearrangement and large distinct hysteresis in the desorption path suggests strong CO_2-host (framework) interaction (Figure 12). The final uptake amount was 42 mLg^{-1} (8.25 wt%). Such hysteretic profile may be attributed to the unsaturated Eu^{3+} metal sites or structural rearrangement during CO_2 inclusion. Such sort of unsaturated metal site-CO_2 interactions are well reported in the literatures. At the same temperature adsorption measurement of CH_4 indicated almost no uptake indicating the selective nature of **1′** towards CO_2 gas (Figure12). Such selectivity might be attributed to the polar nature of the pore environment which is not effective for almost nonpolar CH_4. Such sort of selectivity is very important for the separation purpose and is not very often realized in PCPs. As framework **2** is isostructural to **1**, we did not measure its porous nature because it is expected to behave similarly as that of **1**.

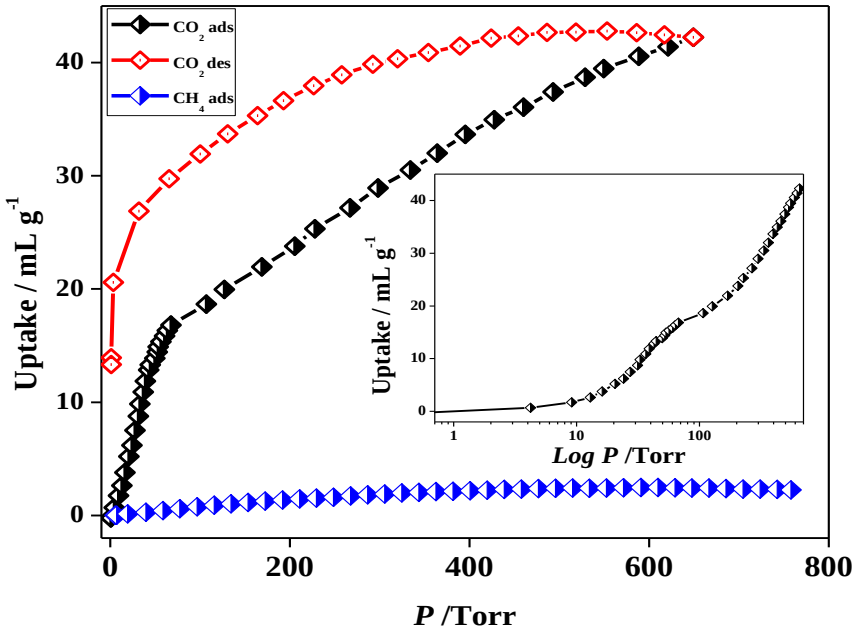

Figure 12: CO_2 and CH_4 adsorption profiles of **1′** at 195 K; inset shows logarithmic scale plot for CO_2 adsorption.

3.3.4 White Light and Tunable Emission

It is well known that lanthanide metal centers are inefficient light emitters due to intra-configurational f-f transition. This problem can be encountered by the indirect excitation of coordinated organic chromophore and this phenomenon is known as "antenna effect". In this case, compound **1** contains Eu^{3+} metal center and an organic chromophore (L) coordination might lead to efficient emission property of Eu^{3+} center. Upon excitation at 300 nm we observed a broad weak emission in the range ~ 400-450 nm and sharp emission peaks centered at 590, 616, 650, and 699 nm related to $^5D_0$-to-^7F_J transitions of Eu^{3+}, where J=1-4, respectively (Figure 13a-13b). The red emission of **1** is due to the most intense peak at 616 nm which corresponds to $^5D_0$-to-$^7F_2$ transition. In this case though there is an antenna effect from ligand chromophore (L) to the metal center, we do observe weak emission at blue region which is due to inefficient overlap of the energy of ligand excited state and lanthanide (Eu^{3+}) ground state. Such dual emission in one hybrid matrix is promising for white light emission which requires emission in the red, green and blue (RGB) region. To exploit this possibility, we have introduced Tb^{3+}, which shows green emission in the presence of strong ligand field (through antenna effect) in the same matrix. As Tb^{3+} and Eu^{3+} have similar ionic radii and coordination mode, an isostructural framework was obtained, described in the previous sections. The

emission spectrum of compound **2** shows emission peaks at 490, 545, 586 and 699 nm corresponding to $^5D_4$-to-^7F_J (J = 6-3 respectively) transitions and relatively weak emission ~ 400-450 nm corresponding to the linker emission (Figure13c). Here, the sharp peak at 545 nm is due to transitions from $^5D_4$-to-$^7F_5$ is responsible for the green emission.

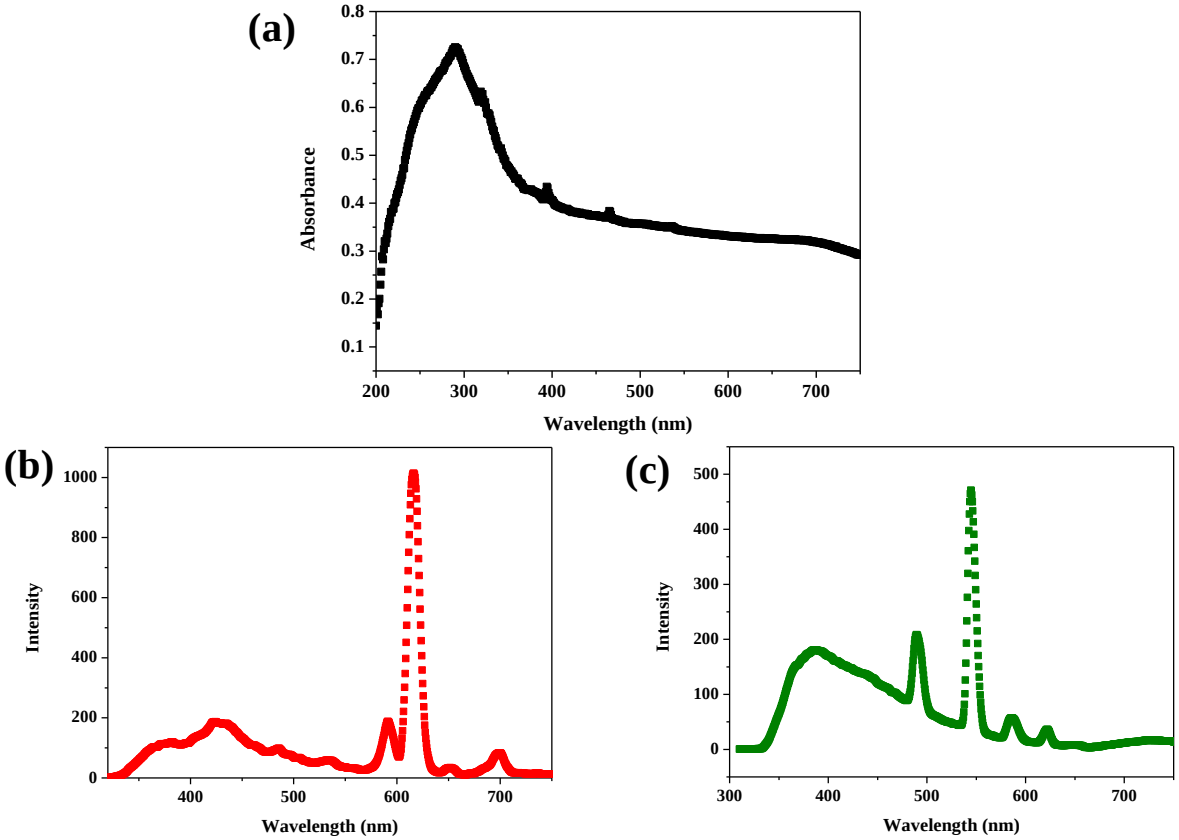

Figure 13: (a) UV-vis spectrum of **1**; (b) Emission spectrum of **1** upon excitation at 300 nm; (c) Emission spectrum of **2** upon excitation at 300 nm.

We envisioned mixing of Tb^{3+} (green), Eu^{3+} (red) and ligand emission (blue) in same framework matrix to obtain white light emission. We have synthesized six different Eu^{3+} doped Tb^{3+} frameworks with Eu^{3+} atom% 0.01 (**2a**), 5.9 (**2b**), 6.7 (**2c**), 7.5 (**2d**), 18.4 (**2e**) and 37.8 (**2f**). These frameworks are isostructural with parent frameworks (**1** and **2**) and have been characterized by PXRD, energy dispersive x-ray analysis (Figure 14).

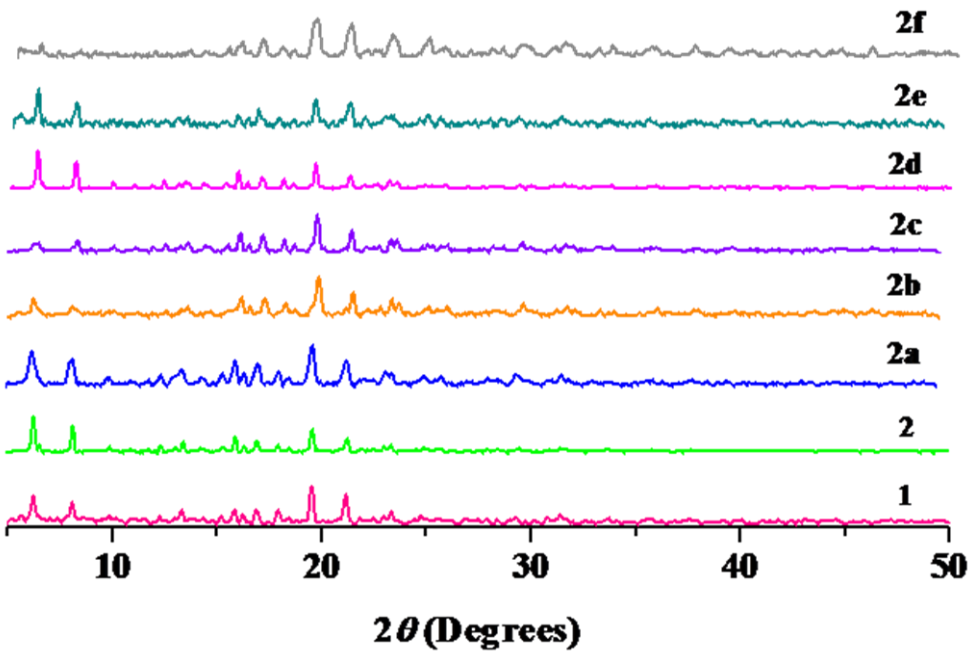

Figure 14: PXRD patterns **1**, **2** and **2a**-**2f**.

Here, before discussing the emission characteristics it is worth to mention that Tb^{3+} and Eu^{3+} are well-known donor-acceptor pair; Tb^{3+} acts as a donor whereas Eu^{3+} acts as an acceptor. Hence, it is possible that in such mixed metal systems energy transfer process would occur from Tb^{3+} to Eu^{3+}. Evidently, mixing of Tb^{3+} and Eu^{3+} in equal concentration may not lead to similar composition of green and red emission. As we increase the concentration of Eu^{3+} in **2f** we observed pink emission while for **2e** orange emission was obtained. These final emissions are mainly governed by the intensities of emission peaks centered at 545 and 615 nm attributed to Tb^{3+} and Eu^{3+}, respectively (Figure 15). As we further decrease the Eu^{3+} concentration we observed almost white emissions for compound **2a-2d** (Figure16a-16b). The calculated CIE coordinates are 0.24/0.33, 0.27/0.34, 0.27/0.31 and 0.27/0.29 for **2a-2d**, respectively (Figure 16c). These coordinates lie in the white light region. Further, we have coated a thin layer of compound **2b** on a blue light emitting LED. The resulting LED emits bright white light on applying voltage (Figure 16b).

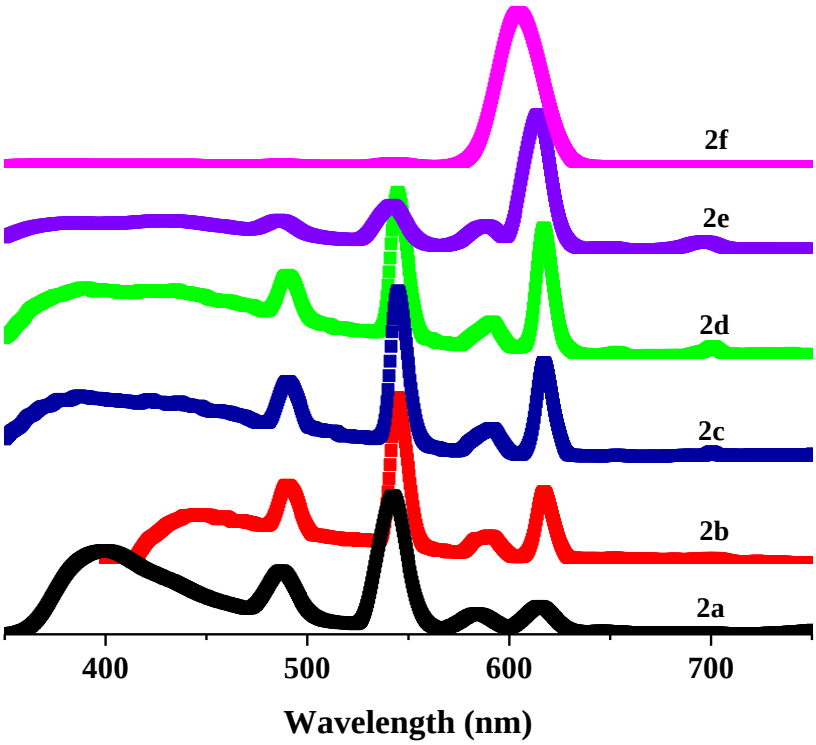

Figure 15: Emission spectra of compound **2a-f**.

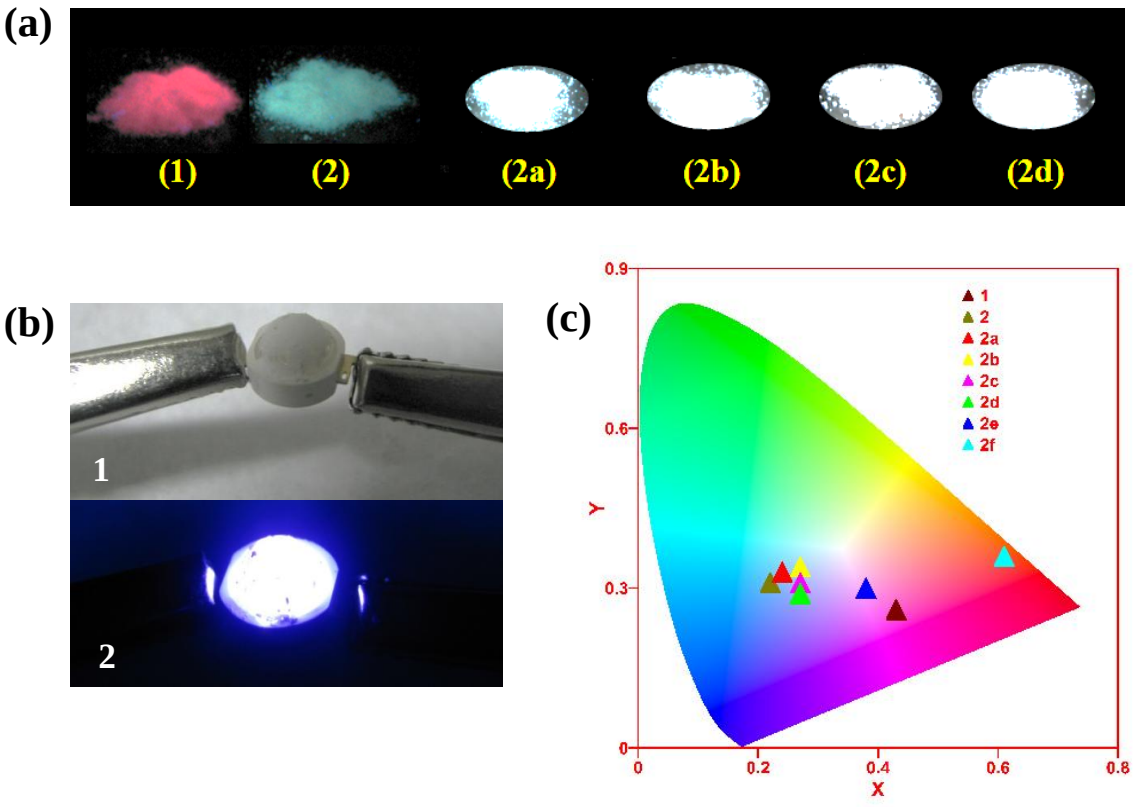

Figure 16: (a) Photographs of compound **1**, **2** and **2a-d** under UV lamp; (b) (1) LED coated with a thin layer of **2b**, (2) The coated LED was turned on and illuminates bright white light; (c) CIE spectrum showing colour coordinates of **1**, **2**, **2a-f**.

3.3.5 Energy Transfer from Tb^{3+} to Eu^{3+}

To confirm the contribution of energy transfer phenomenon we carried out fluorescence lifetime experiments. In Tb^{3+}- Eu^{3+} mixed matrix Tb^{3+} is the usual donor and Eu^{3+} acts as an acceptor. Hence, we monitored the lifetime at 545 nm ($^5D_4$ Tb^{3+} emission) for **2** and **2a-2f**. We observed with increasing percentage of Eu^{3+} in the framework the lifetime decreases from 0.803 to 0.327 ms; whereas the lifetime observed at 625 nm corresponding to $^5D_0$ Eu^{3+} emission increases with increasing Eu^{3+} concentration (Figure 17a-17b). These observations clearly suggest energy transfer from Tb^{3+}→ Eu^{3+}. Further, we calculated the probability of energy transfer ($P_{Tb\rightarrow Eu}$) and energy transfer efficiency ($E_{Tb\rightarrow Eu}$) in **2a-2f** using following equations (Figure 17c):

$I=I_0\exp(-T/\tau)$; where T = time, τ = lifetime and I = Intensity

The probability of energy transfer ($P_{Tb\rightarrow Eu}$)= $(1/\tau)-(1/\tau_0)$

Energy transfer efficiency ($E_{Tb\rightarrow Eu}$) = $1-(\tau/\tau_0)$

where τ_0 = lifetime of Tb^{3+}($^5D_4$) in absence of Eu^{3+}

τ = lifetime of Tb^{3+} ($^5D_4$) in presence of Eu^{3+}

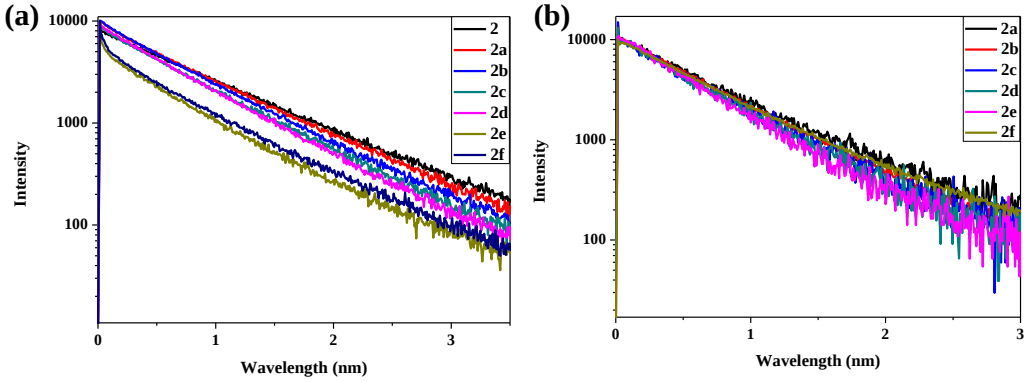

(c)

Compound	$\tau(^5D_4)$(ms)	$P_{Tb\rightarrow Eu}(ms^{-1})$	$E_{Tb\rightarrow Eu}$(%)
2	0.803	----------	----------
2a	0.730	0.124	9.09
2b	0.680	0.224	15.30
2c	0.590	0.450	26.52
2d	0.550	0.573	31.51
2e	0.339	1.655	57.78
2f	0.327	1.813	59.27

Figure 17: (a) Decay profiles of $^5D_4$ state of Tb(III) excited at 300 nm; (b) Decay profiles of $^5D_0$ state of Tb(III) excited at 300 nm; (c) Life time and composition dependent change in the probability ($P_{Tb\rightarrow Eu}$) and efficiency of energy transfer ($E_{Tb\rightarrow Eu}$).

3.4 Conclusions

In conclusion, we have synthesized two isostructural Eu^{3+} and Tb^{3+} based 1D coordination polymer which *via* non-covalent interaction form supramolecular porous frameworks, **1** and **2**, respectively. Framework **1** shows structural flexibility upon removal of guest and coordinated solvent molecules and high selectivity for CO_2 against CH_4 at 195 K. Such selectivity is very important for separation purposes and is rare phenomenon in lanthanide based frameworks. Further, we observed a dual emission characteristics in **1** and **2**, along with Eu^{3+}/ Tb^{3+} emission ligand emission is also visible in the spectra. Following this, proper mixing of Tb^{3+} and Eu^{3+} in same framework matrix yielded orange, pink and white emissions. Such composition dependent emission colour and white light emission in porous lanthanide frameworks are interesting and in future we aim to explore sensing properties and also its solution based processibility.

3.5 References

1 (a) B. W. D' Andrade and S. R. Forrest, *Adv. Mater.*, 2004, **16**, 1585; (b) T. H. L. He, L. Duan and Y. Qiu, *J. Mater. Chem.*, 2012, **22**, 4206; (c) J. H. Burroughes, D. D. C. Bradley, A. R. Brown, R. N. Marks, K. Mackay, R. H. Friend, P.L. Burns and A. B. Holmes, *Nature*, 1990, **347**, 539; (d) W. W. Yu, E. Chang, R. Drezek and V. L. Colvin, *Biochem. Biophys. Res. Commun.* , 2006, **348**, 781.

2 (a) R. M. Mueller-Mach, G. Mueller, M. R. Krames, H. A. Höppe, F. Stadler, W. Schnick, T. Juestel and P. Schmidt, *Phys. Stat. Sol.*, 2005, **202**, 1727; (b) J. Thompson, R. I. R. Blyth, M. Mazzeo, M. Anni, G. Gigli, and R. Cingolani, *Appl. Phys. Lett.*, 2001, **79**, 560.

3 (a) S. Mohapatra, S. Adhikari, H. Riju and T. K. Maji, *Inorg. Chem.*, 2012, **51**, 4891; (b) Q. Tang, S. Liu, Y. Liu, D. He, J. Miao, X. Wang, Y. Ji and Z. Zheng, *Inorg. Chem.*, 2014, **53**, 289; (c) Y. Yip, H. Wen, W. Wong, P. A. Tanner and K. Wong, *Inorg. Chem.*, 2012, **51**, 7013.

4 (a) H. Li, W. Shi, K. Zhao, Z. Niu, H. Li and P. Cheng, *Chem. Eur. J.*, 2013, **19**, 3358; (b) M. Gustafsson, A. Bartoszewicz, B. Martín-Matute, J. Sun, J. Grins, T. Zhao, Z. Li, G. Zhu and X. Zou, *Chem. Mater.*, 2010, **22**, 3316; (c) C. A. Black, J. S. Costa,W. T. Fu, C.

Massera, O. Roubeau, S. J. Teat, G. Aromí, P. Gamez and J. Reedijk, *Inorg. Chem.*, 2009, **48**, 1062.

5 (a) Y. Han, X. Li, L. Li, C. Ma, Z. Shen, Y. Song and X. You, *Inorg. Chem.*, 2010, **49**, 10781; (b) S. Chen, R. Fan, C. Sun, P. Wang, Y. Yang, Q. Su and Y. Mu, *Cryst. Growth Des.*, 2012, **12**, 1337; (c) S. Chen, Y. Ren, W. Wang and S. Gao, *Dalton Trans.*, 2010, **39**, 1552.

6 (a) H. Liu, Y. Luo, Z. Mao, L. Liao and Z. Xia, *J. Mater. Chem. C*, 2014, **2**, 1619; (b) Y. Wei, Q. Li, R. Sa and K. Wu, ***Chem. Commun.***, 2014, **50**, 1820; (c) Y. Liu, M. Pan, Q. Yang, L. Fu, K. Li, S. Wei and C. Su, *Chem. Mater.*, 2012, **24**, 1954; (d) S. Dang, J. Zhangb and Z. Sun, *J. Mater. Chem.*, 2012, **22**, 8868.

7 *SMART (V 5.628), SAINT (V 6.45a), Xprep, SHELXTL*; Bruker AXS Inc. Madison, Wisconsin, USA, 2004.

8 G. M. Sheldrick, *Siemens Area Detector Absorption Correction Program*, University of Götingen, Götingen, Germany, 1994.

9 A. Altomare, G. Cascarano, C. Giacovazzo and A. Gualaradi, *J. Appl. Crystallogr.*, 1993, **26**, 343.

10 G. M. Sheldrick, *SHELXL-97, Program for Crystal Structure Solution and Refinement*, University of Götingen, Götingen, Germany, 1997.

11 (a) A. L. Spek, *J. Appl. Crystallogr.*, 2003, **36**, 7; (b) L. J. Farrugia, WinGX-A Windows Program for Crystal Structure Analysis, *J. Appl. Crystallogr.*, 1999, **32**, 837.

12 The sizes of the channels were calculated considering the van der Waals radii of the atoms.

Chapter: 4

Dye encapsulated into frameworks: Efficient supramolecular light harvesting antenna with colour tunable emission

Summary

This chapter describes design and synthesis of two novel isomorphous 3D flexible supramolecular frameworks for emission colour tunability by encapsulation of a suitable dye. Here, we have utilized biphenyl core as the luminescent chromophoric linker. $\{[Zn(bpdc)(bpy)]\cdot DMF\}_n$ (**1**) and {[Zn(bpdc)(*o*-phen)]·DMF} (**2**) (bpdc = biphenyl-4,4′-dicarboxylic acid ; bpy = 2,2′- bipyridine; *o*-phen = ortho-phenanthroline) are synthesized following simple solvothermal technique. Both 1 D coordination polymers are formed by bridging bpdc linkers where each Zn^{2+} centre is hexacoordinated and connected by four chelated carboxylate oxygen atoms from bpdc and two chelated nitrogen atoms of one bpy or *o*-phen. Supramolecular (π···π or C-H···π) interactions help in the formation of 3D frameworks with large distorted rectangular shaped 1D channel. Solvent vapour adsorption studies are also done for these compounds to understand the nature of pore surface. Partial overlap of the emission spectra of these frameworks with the absorbance spectrum of acridine orange (AO) dye prompted us to incorporate this dye in the pores of the framework for light harvesting applications. Emission colours are tuned through partial energy transfer process by varying the dye percentage in compounds **1** and **2**.

4.1 Introduction

Porous coordination polymers (PCPs) are attractive inorganic-organic hybrid materials in the context of high surface area, modular nature and flexibility with periodic structure.[1] Interesting structural features and ease of functionalization provide wide applicability in gas storage and separation, catalysis, sensing, drug delivery etc.[2] Additionally, the presence of inorganic and organic components also creates the possibility of metal ion and linker based luminescent properties in such hybrid materials. Like lanthanide ions (Tb^{3+}, Eu^{3+} and Sm^{3+}) based emission properties can be realized in PCPs through hybridization of suitable organic linkers through the antenna effect. Luminescent PCPs can be synthesized by connecting suitable metal ions with different organic chromophoric linkers. Such luminescent PCPs have been explored for metal ion/anion/solvent sensing, light harvesting application and other light emitting device applications.[3]

Materials with multicolour emission characteristic have recently become attractive because of their wide applications in flexible full colour display and next generation lighting sources.[4] Organic polymers with different chromophores or lanthanide metal based complexes or coordination polymers have been well exploited in last decade.[5] Organic materials containing RGB chromophoric systems can be ratiometrically tuned at molecular level to get white light emission and presence of energy transfer processes; such as Förster, Dexter or trivial, facilitates such possibilities.[6] Hence, control over the energy transfer process is quite important to generate targeted emission colour. In case of lanthanide based complexes or polymers the mixing of Tb^{3+}/Eu^{3+} in the same matrix can yield multiple emissions and have been exploited for tuning of emission wavelength.[7] In this case also, trivial mixing fails to generate aimed emission arising due to energy transfer process. Apart from these, another way of generating multicolour emission is by doping of luminescent dye molecules in a porous emissive material.[8] The primary criterion is poor or moderate overlap between the donor emission and acceptor absorbance to control the efficiency of energy transfer process. In this work we have exploited a new flexible supramolecular framework for emission colour tuning through encapsulation of dye molecules and successive partial energy transfer from framework to the dye chromophore (Scheme 1). We chose a biphenyl core as the luminescent chromophore and were able to assemble a 1D coordination polymer of $\{[Zn(bpdc)(bpy)]\cdot DMF\}_n$ (**1**). It forms supramolecular 3D structure with large one

dimensional channel. **1** was found to be flexible as realized from PXRD studies, CO_2 adsorption and solvent vapour (water, methanol and ethanol) adsorption studies. The flexible and aromatic electron rich pore surfaces were exploited for dye (Acridine Orange) encapsulation and partial energy transfer process from framework to dye molecule. Further structural modification was done by synthesizing structurally similar $\{[Zn(bpdc)(o\text{-phen})]\cdot DMF\}_n$ (**2**) with different chelating linker but similar pore surface and structural flexibility to that of **1** was obtained. Such modulation affects the energy transfer process and emission colours are further tuned. Such tuning of emission colours from host framework to non-covalently encapsulated guest dye molecule is unprecedented.

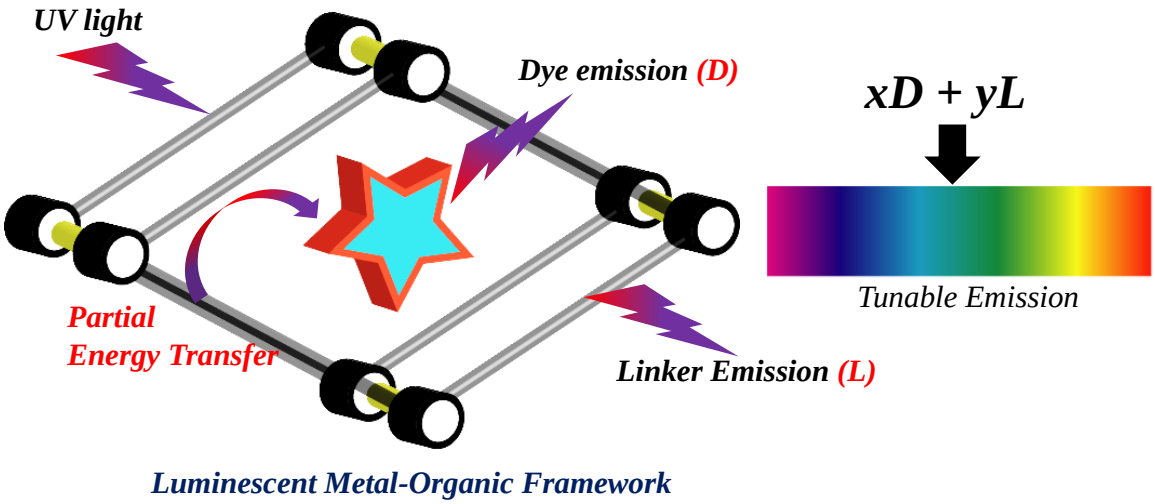

Scheme 1: Schematic showing dual emission from dye encapsulated PCP through partial energy transfer from host PCP to the guest.

4.2 Experimental Section

4.2.1 Materials

All the reagents were commercially available and used as provided without further purification. Metal salt was obtained from SDFCL, biphenyl-4,4′-dicarboxylic acid, ortho-phenanthroline and 2,2′-bipyridine were obtained from Sigma Aldrich chemicals. Acridine orange hydrochloride hydrate was purchased from Acros Organics.

4.2.2 Physical Measurements

Elemental analysis was carried out using a Thermo Fischer Flash 2000 Elemental Analyzer. FT-IR spectra were recorded on a Bruker IFS 66v/S spectrophotometer using KBr pellets in the region 4000–400 cm^{-1}. Thermogravimetric analysis (TGA) was carried out (Metler Toledo) in nitrogen atmosphere (flow rate = 50 mL min^{-1}) in the temperature range 30–700 °C (heating rate = 3 °C min^{-1}). Powder X-ray diffraction (PXRD) patterns of the products were recorded on a Bruker D8 Discover instrument using Cu−Kα radiation. The pattern agreed with those calculated from single crystal structure determination. Electronic absorption spectra were recorded on a Perkin Elmer Lambda 900 UV-VIS-NIR Spectrometer and PL spectra were taken with Perkin-Elmer model LS 55 luminescence spectrometer. NMR spectra were obtained with a Bruker AVANCE 400 (400 MHz) Fourier transform NMR spectrometer with chemical shifts reported in parts per million (ppm). Fluorescence decay was recorded in a time correlated single photon counting spectrometer of Horiba-Jobin Yvon with 350-450 nm picosecond Ti-saphhire laser.

4.2.3 X-ray Crystallography

X-ray single crystal structural data of **1** and **2** were collected on a Bruker Smart-CCD diffractometer equipped with a normal focus, 2.4 kW sealed tube X-ray source with graphite monochromated Mo-Kα radiation (λ = 0.71073 Å) operating at 50 kV and 30 mA. The program SAINT[9] was used for integration of diffraction profiles and absorption correction was made with SADABS[10] program. All the structures were solved by SIR 92[11] and refined by the full matrix least-squares method using SHELXL-97.[12] All the hydrogen atoms were fixed by HFIX and placed in ideal positions. Potential solvent accessible area or void space was calculated using the PLATON multipurpose crystallographic software.[13] All crystallographic and structure refinement data of **1** and **2** are summarized in Table 1. Selected bond lengths and angles for **1** and **2** are given in Tables 2-5. All calculations were carried out using PLATON and WinGX system, Ver 1.70.01.[15]

4.2.4 Adsorption Measurements

Adsorption isotherms of N_2 (77 K and 195 K) and CO_2 (195 K) were recorded using the desolvated samples of **1** (**1′**) and **2** (**2′**) by using a QUANTACHROME QUADRASORB-SI analyzer. In the sample tube, the adsorbent samples (**1′** and **2′**)

(~100−150 mg) were placed which had been prepared at 150 °C under a 1×10^{-1} Pa vacuum for about 12 h prior to measurement of the isotherms. Helium gas (99.999% purity) at a certain pressure was introduced in the gas chamber and allowed to diffuse into the sample chamber by opening the valve. The amount of gas adsorbed was calculated from the pressure difference ($P_{cal} - P_e$), where P_{cal} is the calculated pressure with no gas adsorption and P_e is the observed equilibrium pressure. All the operations were computer controlled and automatic. The adsorption isotherm of different solvents (methanol at 293 K, ethanol and water at 298 K) of **1′** and **2′** were measured in the vapour state by using a BELSORP-aqua volumetric adsorption instrument from BEL, Japan. A sample of about ~100−150 mg was prepared by heating at 150 °C for about 12 h under a vacuum (1×10^{-1} Pa) prior to measurement of the isotherms. The solvent molecules used to generate the vapour were degassed fully by repeated evacuation. Dead volume was measured with helium gas. The adsorbate was placed into the sample tube, then the change of the pressure was monitored, and the degree of adsorption was determined by the decrease in pressure at the equilibrium state. All operations were computer controlled and automatic.

4.2.5 Syntheses

4.2.5.1 Synthesis of {[Zn(bpdc)(bpy)]·DMF}$_n$ (1)

Biphenyl-4,4′-dicarboxylic acid (0.024 g, 0.1 mmol) and 2,2′- bipyridine (0.016 g, 0.1 mmol) were dissolved in 5 mL of dimethyl formamide (DMF) and mixed well. 0.03 g (0.1 mmol) of $Zn(NO_3)_2 \cdot 6H_2O$ was added to the ligand solution and sonicated before the sealed vial was kept in an oven at 120 °C for 24 h. Good quality transparent crystals of **1** were isolated and washed with fresh DMF before taking for single-crystal X-ray diffraction measurement. Yield for **2**: 63%; Anal. Calcd. for $C_{27}H_{23}N_3O_5Zn$: C, 60.63; H, 4.3; N, 7.85. Found C, 60.05; H, 4.16; N, 7.83. FT-IR (KBr pellet, 4000-400 cm^{-1}): 3425 (b), 2925 (s), 2852 (s), 1818 (w), 1747 (s), 1664 (s), 1581 (s), 1529 (s), 1465 (w), 1446 (w), 1394 (s), 1319 (w), 1261 (s), 1174 (w), 1105 (m), 1020 (s), 854 (s), 813 (w), 779 (s), 667 (m), 584 (m), 532 (w), 480 (m).

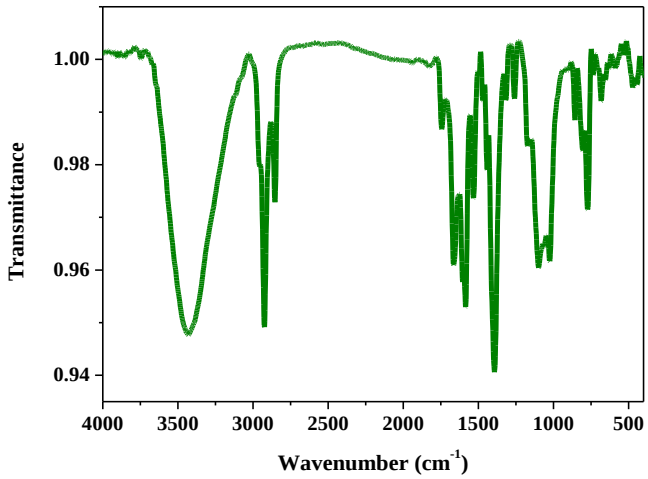

Figure 1: FT-IR spectrum of **1**.

4.2.5.2 Synthesis of {[Zn(bpdc)(*o*-phen)]·DMF}$_n$ (2)

Synthesis of **2** is similar to that of **1** except 2,2′-bipyridine is replaced by 1,10-phenanthroline (0.02 g, 0.1 mmol). Yield of **2**: 56 %; Anal. Calcd. for $C_{29}H_{23}N_3O_5Zn$: C, 62.30; H, 4.12; N, 7.52. Found C, 62.01; H, 4.13; N, 7.80. FT-IR (KBr pellet, 4000−400 cm^{-1}): 3425 (b), 3068 (s), 2921 (s), 2856 (s), 1676 (s), 1602 (s), 1543 (s), 1523 (w), 1496 (w), 1421 (w), 1386 (s), 1103(s), 1006 (m), 854 (s), 777 (s), 725 (s), 686 (s), 649 (w), 550 (w), 476 (w), 440 (s).

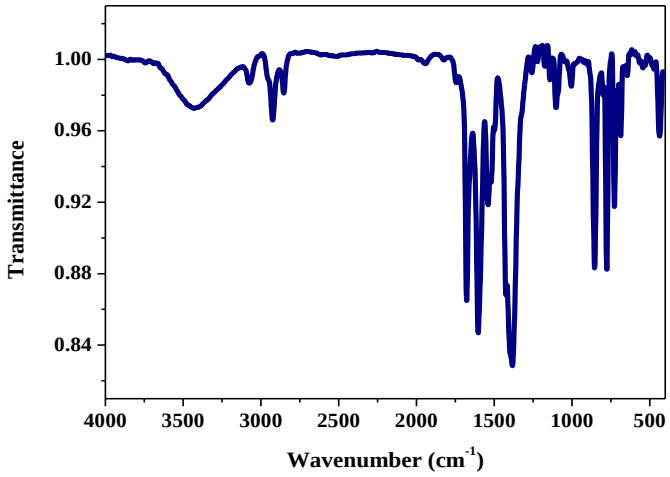

Figure 2: FT-IR spectrum of **2**.

4.2.5.3 Synthesis of AO dye included 1 and 2 (1a, 1b, 1c, 1d, 2a and 2b)

0.03 g of compound **1′** was dipped in 1.5 mL methanol solution of 5 mole% acridine orange dye. The mixture was then stirred for 48 hours, filtered, washed with fresh methanol and dried to obtain compound **1a** containing 0.125% of AO dye. Further, the dye amount was increased to 15 mole% and compound **1** was stirred in 1.5 mL methanol solution of AO dye for 30, 48 and 72 hours. The composite formed (**1b**, **1c** and **1d**) contains 0.32, 0.46 and 0.65% of AO respectively. **1a**-**1d** have been characterized by FT-IR and ^{1}H-NMR studies (Figure 3-7).

0.03 g of compound **2′** was dipped in 1.5 mL methanol solution of 5 mol% acridine orange dye. The mixture was then stirred for 48 hours, filtered, washed with fresh methanol and dried to obtain compound **2a** containing 0.125% of AO dye. Similar procedure was followed for the preparation of **2b** except the amount of acridine orange was increased to 15 mol%. The resulting compound has 1.24% dye content. **2a** and **2b** have been characterized by FT-IR and ^{1}H-NMR studies (Figure 8-10).

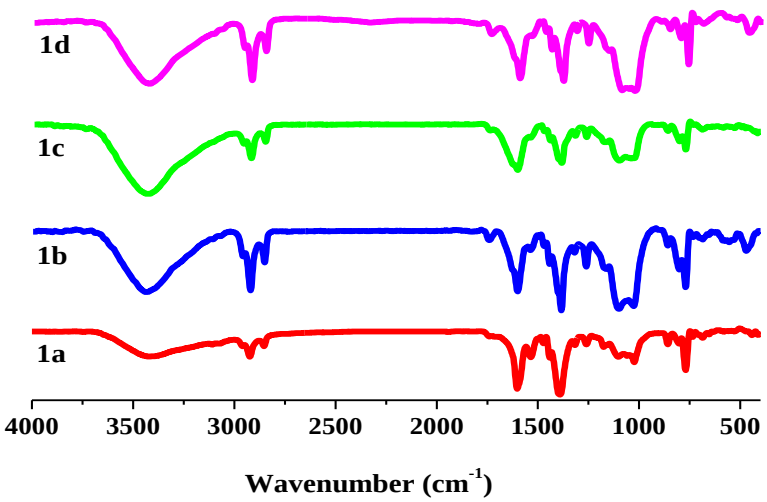

Figure 3: FT-IR spectra of **1a**, **1b, 1c** and **1d**.

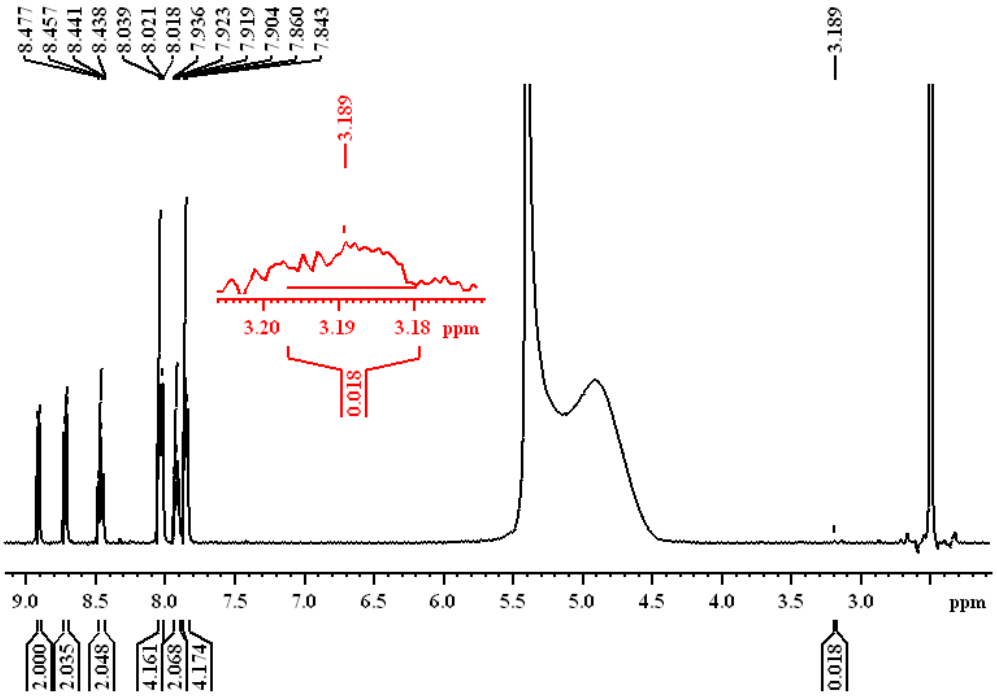

Figure 4: ^{1}H-NMR spectrum of the digested compound **1a** (DCl/d_6-DMSO).

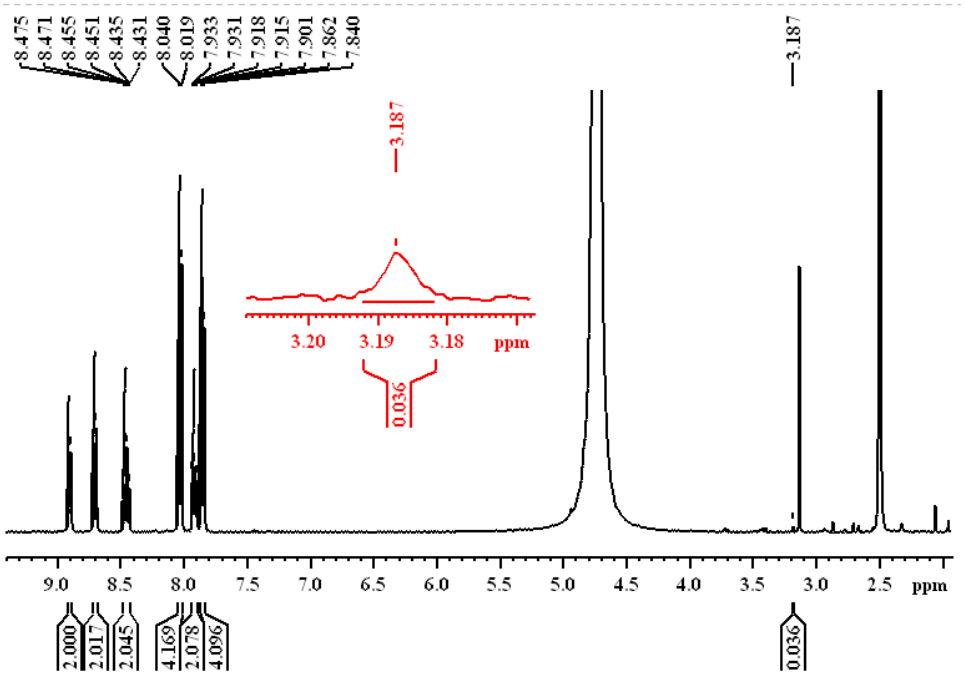

Figure 5: ^{1}H-NMR spectrum of the digested compound **1b** (DCl/d_6-DMSO).

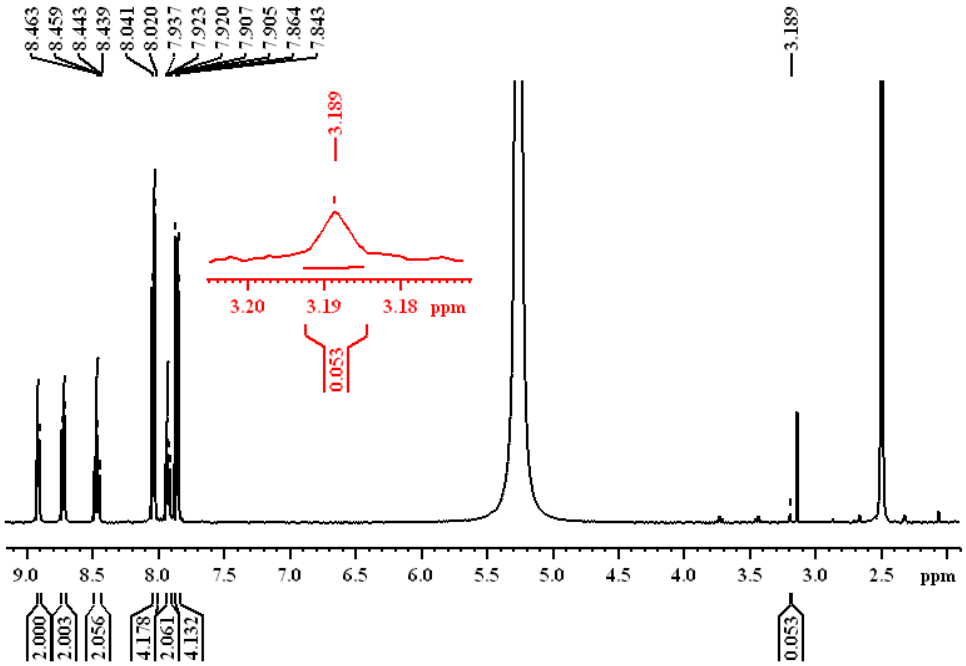

Figure 6: ^{1}H-NMR spectrum of the digested compound **1c** (DCl/d_6-DMSO).

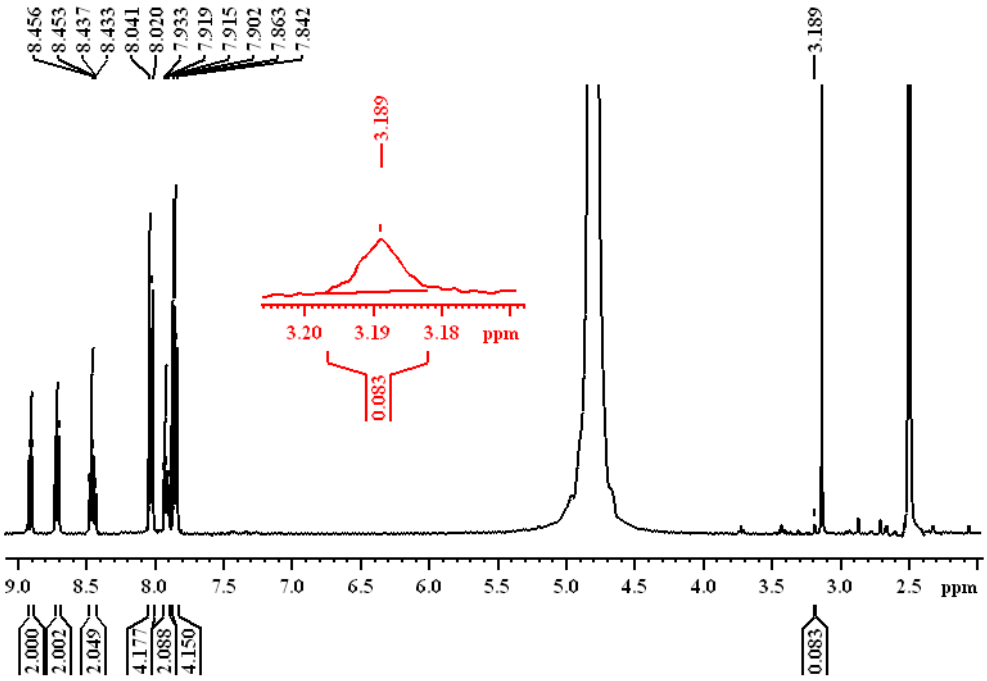

Figure 7: ^{1}H-NMR spectrum of the digested compound **1d** (DCl/d_6-DMSO).

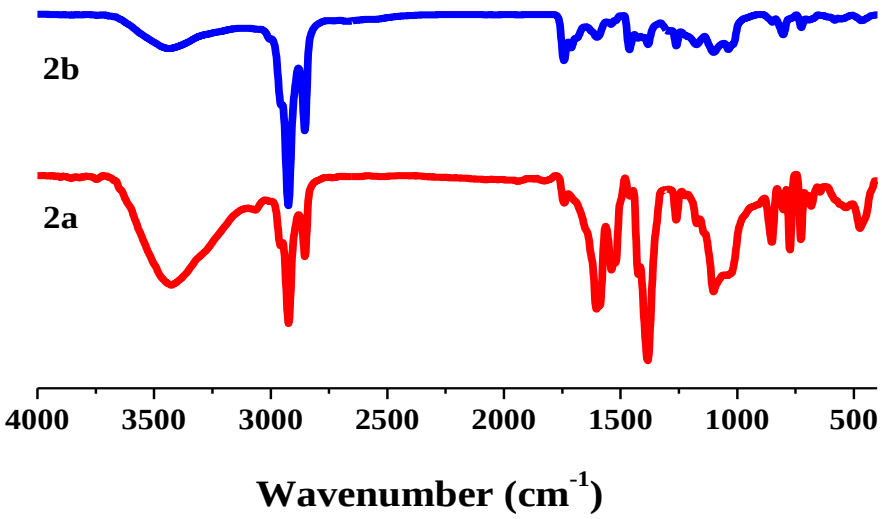

Figure 8: FT-IR spectra of **2a** and **2b**.

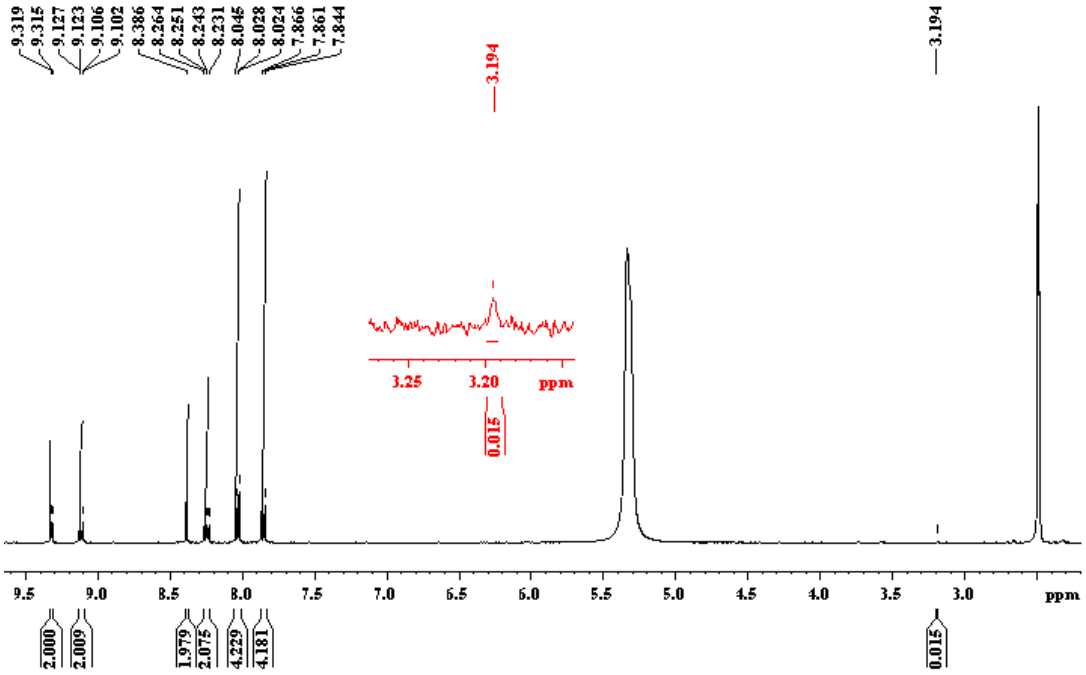

Figure 9: ^{1}H-NMR spectrum of the digested compound **2a** (DCl/d_6-DMSO).

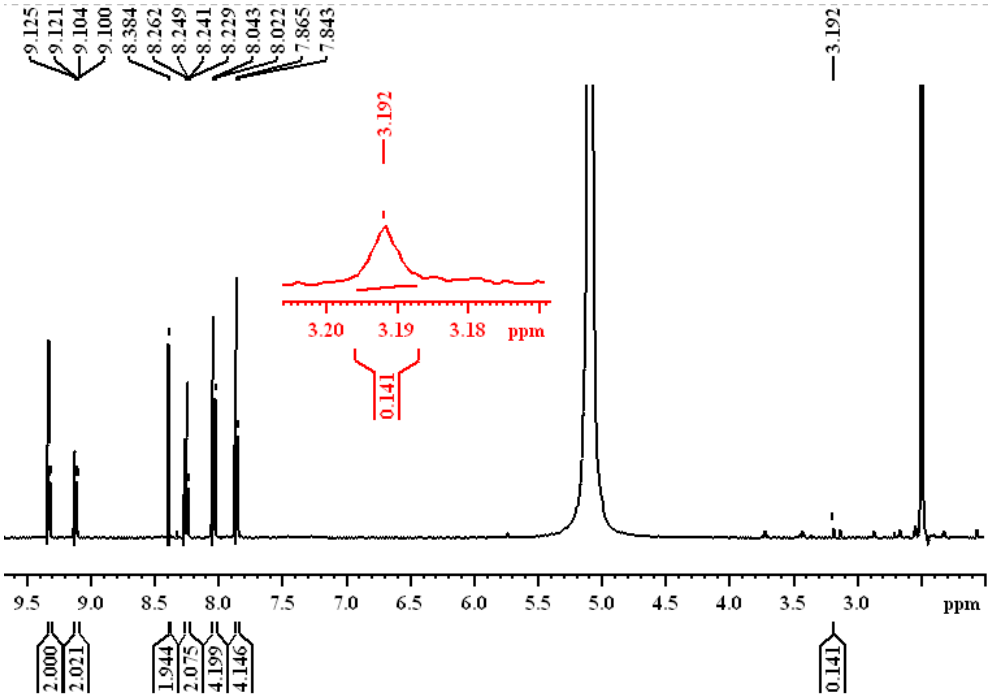

Figure 10: ^{1}H-NMR spectrum of the digested compound **2b** (DCl/d_6-DMSO).

4.3 Results and Discussion

4.3.1 Structural Description of {[Zn(bpdc)(bpy)]·DMF}$_n$ (1)

Compound **1** crystallizes in monoclinic $P2_1/n$ space group. The metal center Zn(II) is hexacoordinated; four oxygens (O1, O2, O3 and O4) from two bpdc and two nitrogens (N1 and N2) of one bpy (Figure 11a) fulfil the coordination sphere. The bpdc linkers connect two metal centers and bpy binds in chelating fashion to form a 1D *zigzag* chain. The 1D coordination polymer so formed stack over each other by face to face π-π interaction between bpy and forms a supramolecular 3D structure with large distorted rectangular shaped 1D channels (13.4×10.5 Å^2) (Figure 11b-11c). The void space calculated using PLATON software is 46% of the total cell volume. The guest DMF molecules are confirmed from TGA, elemental analysis and ^{1}H-NMR (Figure 12 and 13).

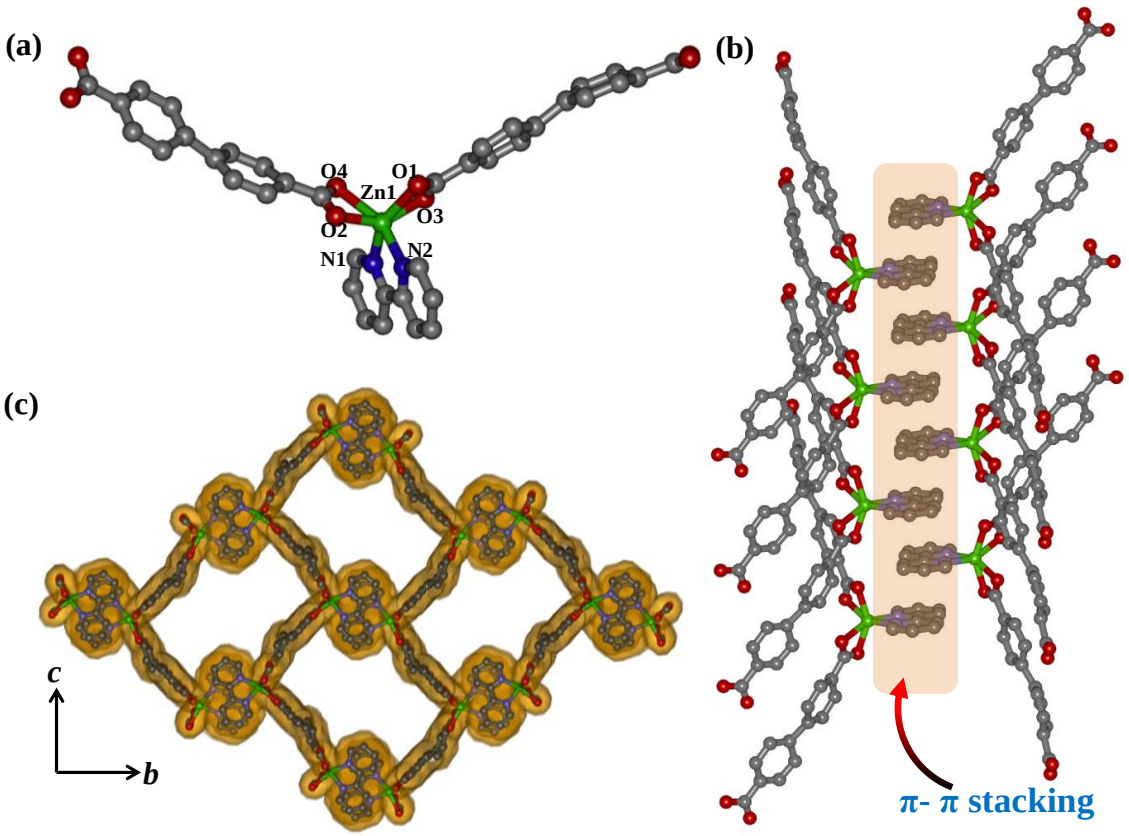

Figure 11: Structural details of **1**: (a) Coordination environment of Zn(II); (b) π-π stacking of the *o*-phen along *a*-axis; (c) View of the distorted rectangular 1D pore.

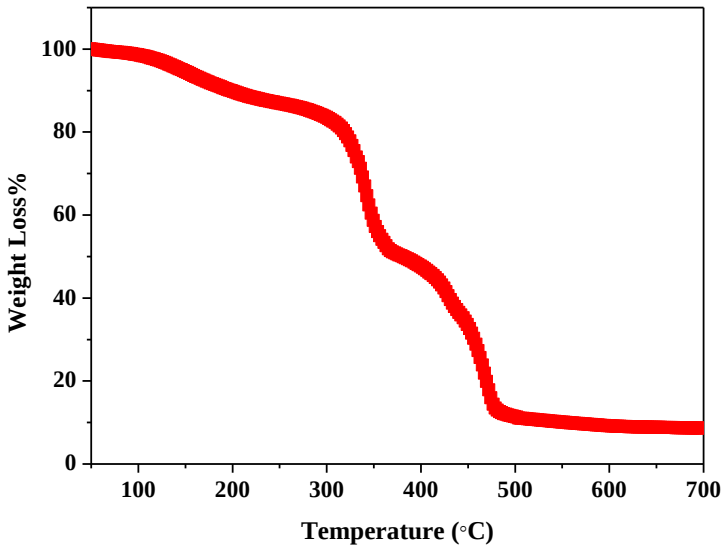

Figure 12: TGA profile for compound **1** in the range of 50–700 °C.

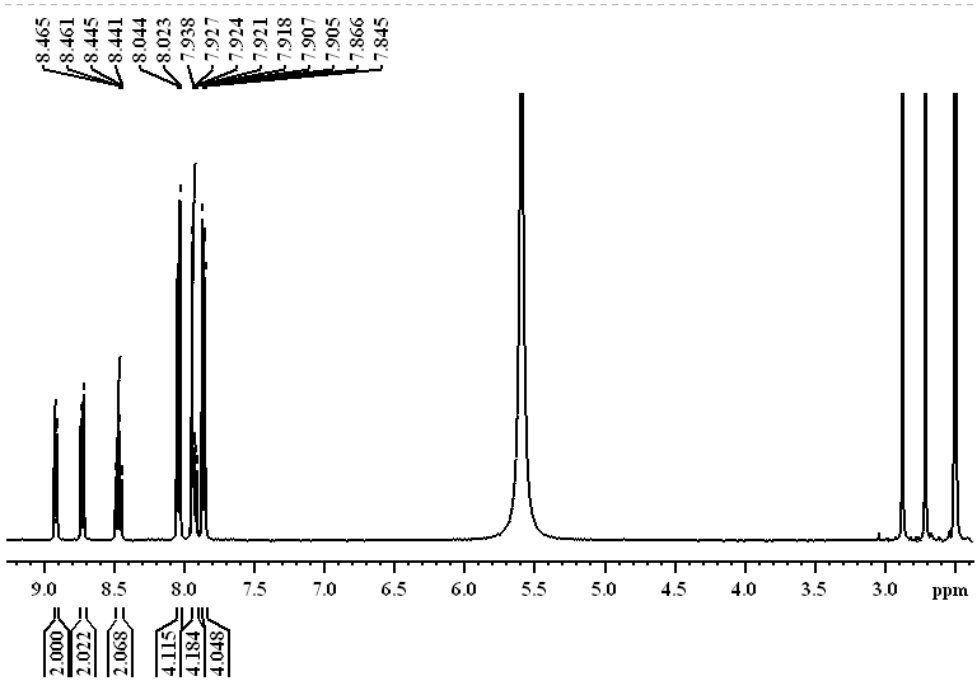

Figure 13: ^{1}H-NMR spectrum of the digested compound **1** (DCl/d_6-DMSO).

4.3.2 Structural Description of {[Zn(bpdc)(*o*-phen)]·DMF}$_n$ (2)

Compound **2** contains a different chelator, *o*-phen and structure determination using single crystal X-ray diffraction suggests that **2** crystalizes in monoclinic $P2_1/n$ space group and the asymmetric unit contains one Zn^{2+} metal center, one bpdc and one *o*-phen (Figure 14a). The Zn^{2+} coordination environment remains similar to that in **1**, six coordinating atoms are four oxygen atoms (O1, O2, O3 and O4) from two carboxylate groups of bpdc and two nitrogen atoms (N1 and N2) from one *o*-phen. Similar to **1**, the bpdc linkers connect two metal centers and *o*-phen binds in chelating fashion to form a 1D *zigzag* chain (Fig. 11a). These 1D chains are held together by face to face π-π interaction (3.518 Å) between the *o*-phen rings of neighbouring chains to grow along the *a* and *b*-axes (Figure 14b). Such soft van der Waals force affords a 3D supramolecular framework furnishing large distorted rectangular shaped 1D channels with dimensions 14.5 × 9 Å^2 (Figure 14c). The replacement of bpy by *o*-phen does change the pore size significantly. These channels are filled with guest DMF molecules, confirmed from TGA, elemental analysis and ^{1}H-NMR (Figure 15 and 16). Calculated void space after removal of guest DMF molecules using PLATON software is 44% of the total cell volume, slightly lower than that observed in **1**.

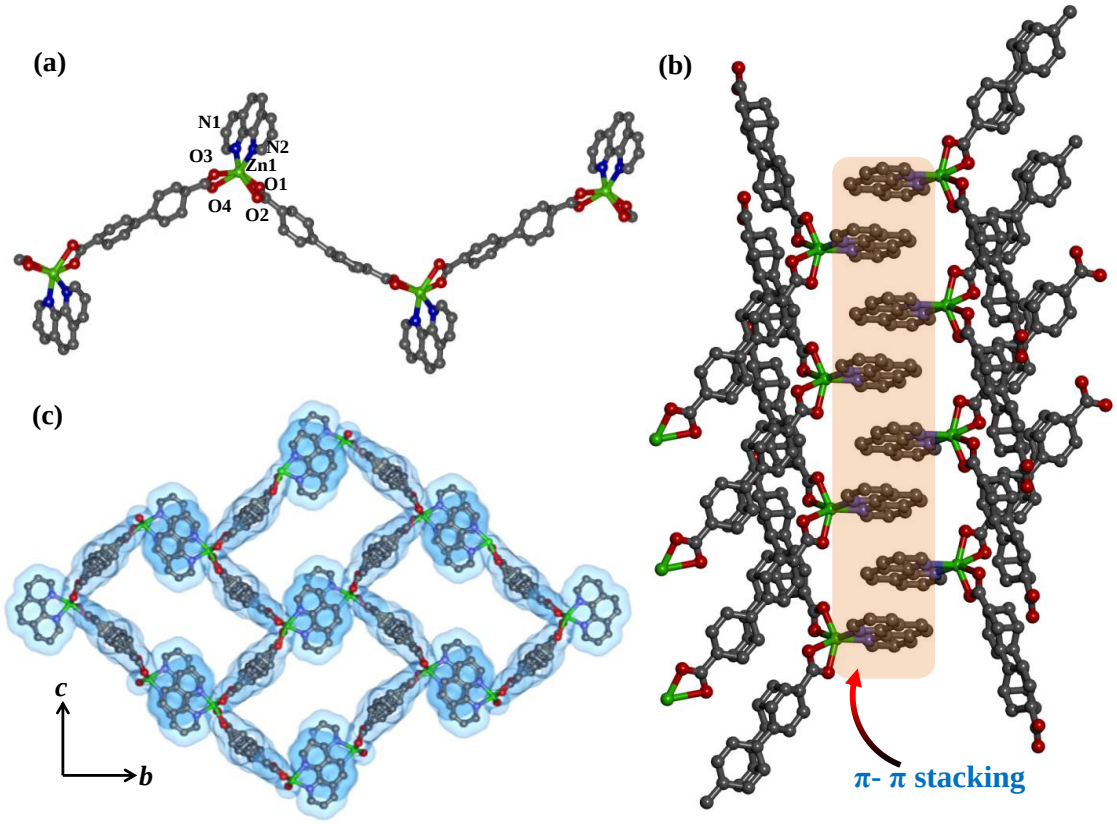

Figure 14: Structural details of **2**: (a) *Zigzag* 1D coordination polymer; (b) π···π stacking of the *o*-phen along *a*-axis; (c) View of the distorted rectangular 1D pore.

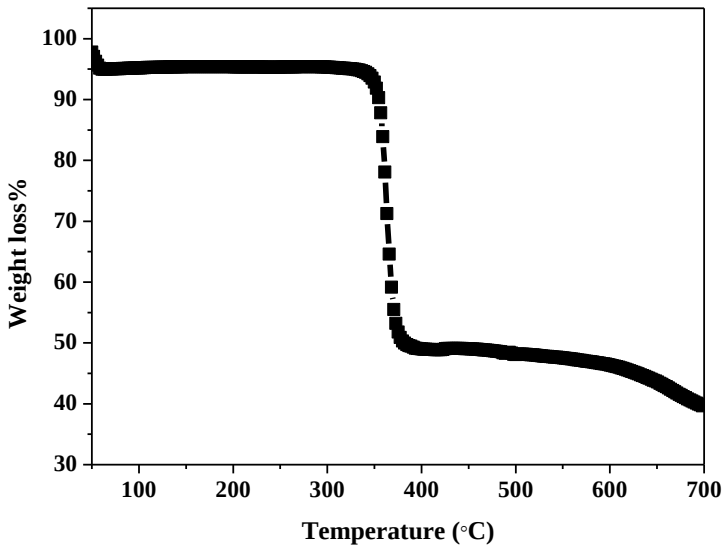

Figure 15: TGA profile for compound **2** in the range of 50–700 °C.

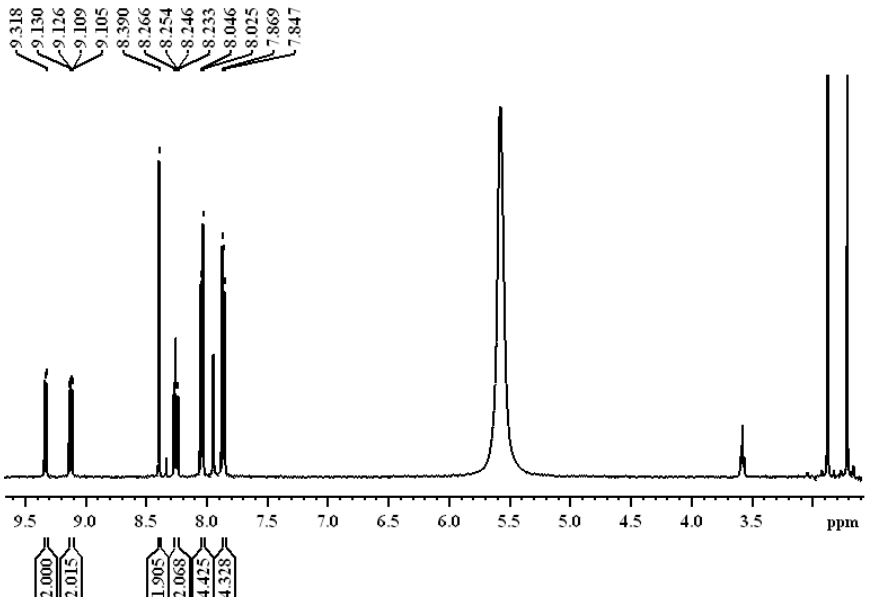

Figure 16: ^{1}H-NMR spectrum of the digested compound **2** (DCl/d_6-DMSO).

Table 1: Crystal data and structure refinement parameters of **1** and **2**.

Parameters	**1**	**2**
Empirical formula	$C_{27}H_{23}N_3O_5Zn$	$C_{29}H_{23}N_3O_5Zn$
Formula weight	534.38	558.59
Crystal system	Monoclinic	Monoclinic
Space group	$P2_1/n$	$P2_1/n$
a, Å	7.7079(4)	7.7033(3)
b, Å	25.7517(14)	28.6099(11)
c, Å	17.1869(10)	16.1008(6)
β, deg	99.453	100.478(2)
V, Å^3	3365.1(3)	3489.3(2)
Z	4	4
T, K	293	293
μ,mm^{-1}	0.750	0.726
D_{calcd},g/cm^3	0.896	0.913
F (000)	912	968
Reflections [$I>2\sigma(I)$]	4213	3774
Unique reflections	8394	8696
Total reflections	38326	42278
R_{int}	0.077	0.079
GOF on F^2	1.11	1.06
$R_1[I>2\sigma(I)]^a$	0.0966	0.0951
R_w[all data]^b	0.3448	0.3579
$\Delta\rho$ max/min [e Å^{-3}]	1.00, -0.99	1.02, -0.65

$^aR_1 = \sum||F_o|-|F_c||/\sum|F_o|$; $^bR_w = [\sum\{w(F_o^2-F_c^2)^2\}/\sum\{w(F_o^2)^2\}]^{1/2}$

Table 2: Selected bond distances (Å) for **1**.

Zn1-O1	2.030(3)	Zn1-O2	2.053(3)
Zn1-O3	2.307(5)	Zn1-O4	2.291(5)
Zn1-N1	2.098(5)	Zn1-N2	2.104(5)

Table 3: Selected bond angles (°) for **1**.

O1-Zn1-O2	146.65(16)	O1-Zn1-O3	58.91(14)
O1-Zn1-O4	99.21(15)	O1-Zn1-N1	107.10(18)
O1-Zn1-N2	100.91(17)	O2-Zn1-O3	99.29(14)
O2-Zn1-O4	59.87(14)	O2-Zn1-N2	104.94(17)
O2-Zn1-N1	98.80(17)	O3-Zn1-N1	94.1(2)
O3-Zn1-O4	105.21(18)	O4-Zn1-N1	152.90(19)
O3-Zn1-N2	155.30(17)	N1-Zn1-N2	77.7(2)
O4-Zn1-N2	91.27(19)		

Table 4: Selected bond distances (Å) for **2**.

Zn1-O1	2.306(6)	Zn1-O2	1.989(4)
Zn1-O3	2.412(6)	Zn1-O4	2.030(4)
Zn1-N1	2.119(8)	Zn1-N2	2.143(6)

Table 5: Selected bond angles (°) for **2**.

O1-Zn1-O2	98.65(18)	O1-Zn1-O3	104.4(2)
O1-Zn1-O4	59.25(18)	O1-Zn1-N1	154.3(2)
O1-Zn1-N2	91.0(2)	O2-Zn1-O4	143.83(17)
O2-Zn1-O3	57.41(17)	O2-Zn1-N2	100.1(2)
O2-Zn1-N1	106.1(2)	O3-Zn1-O4	98.02(18)
O3-Zn1-N1	95.0(3)	O3-Zn1-N2	153.9(2)
O4-Zn1-N2	108.0(2)	O4-Zn1-N1	101.9(2)
N1-Zn1-N2	77.9(3)		

4.3.3 PXRD Analysis and Thermal Stability

TGA profile of **1** shows a weight loss of ~14 weight % in the temperature range of 100-270 °C which corresponds to loss of one guest DMF molecule (Figure 12). The desolvated framework (**1′**) is stable upto ~ 300 °C and collapses upon further heating. TG analysis of **2** shows initial weight loss of 10 wt% indicating loss of guest DMF molecule and the desolvated state (**2′**) is stable upto 340 °C (Figure 15). Further heating decomposes the framework. PXRD pattern of the desolvated framework **1′** shows distinct difference compared to the as-synthesized pattern suggesting structural reorganization after guest removal (Figure 17). In this sort of supramolecular framework structural rearrangement after guest removal is expected due to presence of weak non-covalent interactions. Similarly, for compound **2** also we observed changes in the PXRD pattern after guest solvent removal at 160 °C indicating structural rearrangement (Figure 18).

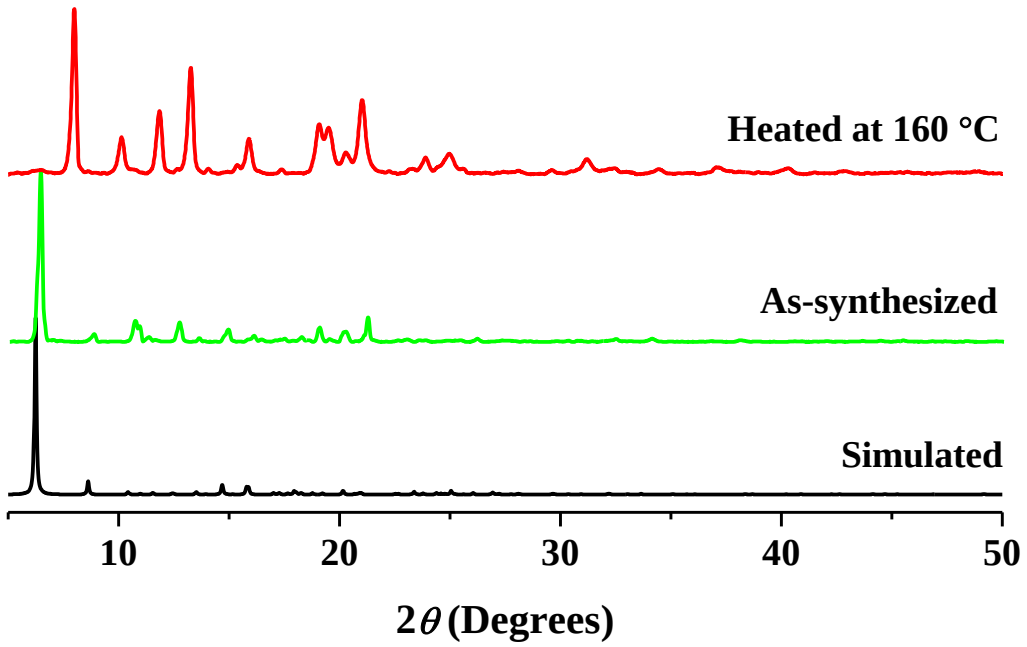

Figure 17: PXRD patterns of simulated, as-synthesized and heated phase of compound **1**.

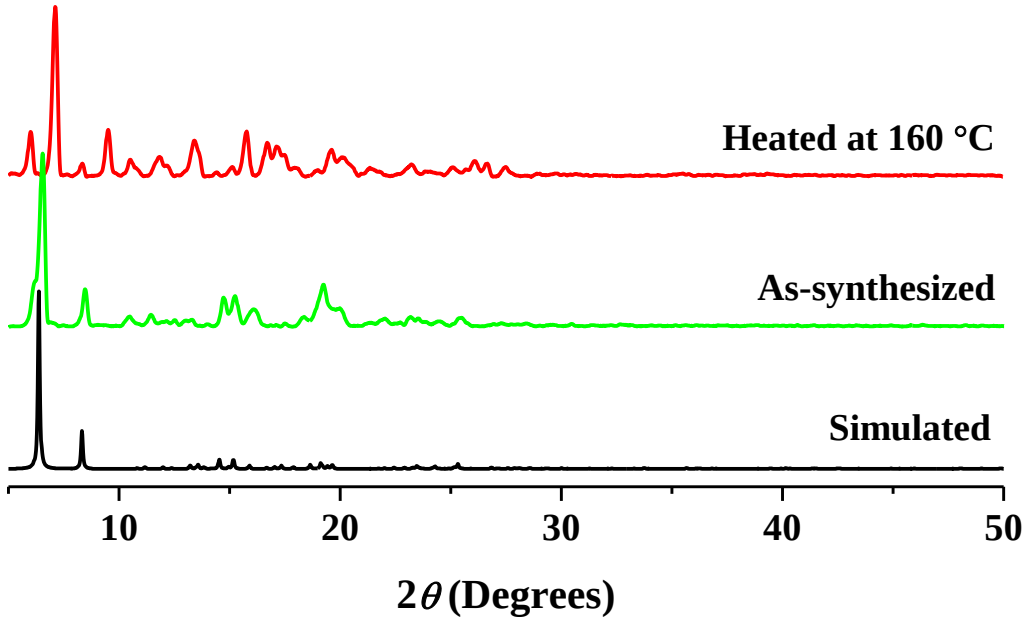

Figure 18: PXRD patterns of simulated, as-synthesized and heated phase of compound **2**.

4.3.4 Gas and Solvent Vapour Adsorption

To verify the porosity in compound **1′** and compound **2′** we measured the N_2 adsorption isotherm at 77 K. Both of them show a typical type-II adsorption profile indicating only surface adsorption (Figure 19). As the desolvated phases of **1** and **2** both

undergo structural contraction, the pore sizes are probably not suitable for N_2 (kinetic diameter ~ 3.64 Å) diffusion. But surprisingly at 195 K both show stepwise CO_2 adsorption profiles with final uptake amounts 33 and 30 mLg^{-1} (Figure 20). Compound **1′** shows a small step at P/P_0 ~ 0.1 and the desorption path does not re-track the adsorption path leading to a huge hysteresis. Similarly, compound **2′**, shows a clear step around P/P_0 ~ 0.1 and the desorption path creates a small hysteresis indicating structural change during adsorption and strong interaction with CO_2. In both cases, the most probable interaction sites inside the pores are the aromatic π-clouds from bpdc and *o*-phen/bpy. Similar sort of aromatic $\pi\cdots CO_2$ interactions are reported in literatures.

To further probe the pore surfaces of both the compounds we carried out different solvent (water, methanol and ethanol) vapour adsorption experiments. At 298 K, water vapour uptake increases slowly for **1′** and rises in linear fashion to reach a final uptake amount of ~ 50 mLg^{-1} (1.03 molecules of water per formula) (Figure 21a). The desorption profile follows a path different from that of adsorption and hence displays a small hysteresis. Surprisingly, methanol vapour adsorption profile for **1′** at 293 K shows stepwise uptake with two steps. It follows a type I profile till ~ 0.4 P/P_0 with an uptake amount of ~ 63 mLg^{-1} (1.3 molecules per formula) (Figure 21b). Then the uptake increases until a second step occurs at 0.62 P/P_0 where the uptake amount is 110 mLg^{-1} which corresponds to 2.3 molecules per formula. The uptake increases further and reaches finally to 115 mLg^{-1} (2.4 molecules per formula). The desorption curve shows a large hysteresis. The ethanol adsorption profile of **2′** shows an almost type I profile where the final uptake reaches to ~ 17 mLg^{-1} (0.35 molecules per formula), much lesser than methanol vapour uptake. Desorption do not retract the adsorption path exhibiting a hysteresis in the profile (Figure 21c). Lesser uptake is probably due to larger kinetic diameter of ethanol. Evidently, the methanol and ethanol contains hydrophobic aliphatic component which interact with pore channels more effectively than highly polar water molecules. This concludes hydrophobic nature of the pore surface.

The above conclusions about the structure are further confirmed by the solvent vapour adsorption study of compound **2′**. At 298 K, water adsorption profile of compound **2′** shows very slow initial uptake and rises almost linearly to reach final uptake amount 94 mLg^{-1} (2 molecules of water per molecular formula) (Figure 22a). Interestingly, it leaves a small hysteresis in the desorption profile and releases almost all the adsorbed water vapour. Methanol vapour adsorption profile shows a stepwise uptake profile similar

to **1′** with a distinct large hysteresis at 293 K (Figure 22b). Till P/P_0 ~ 0.36 uptake profile is type-I and uptake amount is 51 mLg^{-1} which corresponds to one molecule of methanol per formula. After this point, uptake rises further to reach 115 mLg^{-1} at P/P_0 ~ 0.73 (2.5 molecules/formula). Further steep uptake reaches to a final uptake amount of 172 mLg^{-1} which is 3.72 molecules per formula. During the desorption process till P/P_0 ~ 0.3 almost all adsorbed methanol is retained and then releases slowly till P/P_0 ~ 0.1 (76 mLg^{-1}). At 298 K, ethanol vapour adsorption profile shows negligible uptake till P/P_0 ~ 0.57 and then suddenly jumps to reach a final uptake value of 48 mLg^{-1} (1 molecule of ethanol per formula) which is much less than methanol vapour uptake (Figure 22c). Such gate opening type uptake profile also accompanies large hysteresis.

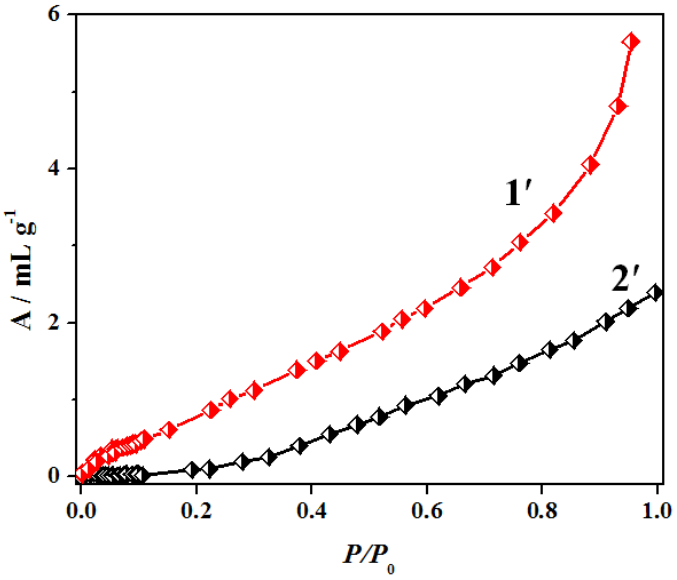

Figure 19: N_2 adsorption profiles for **1′** and **2′** at 77 K.

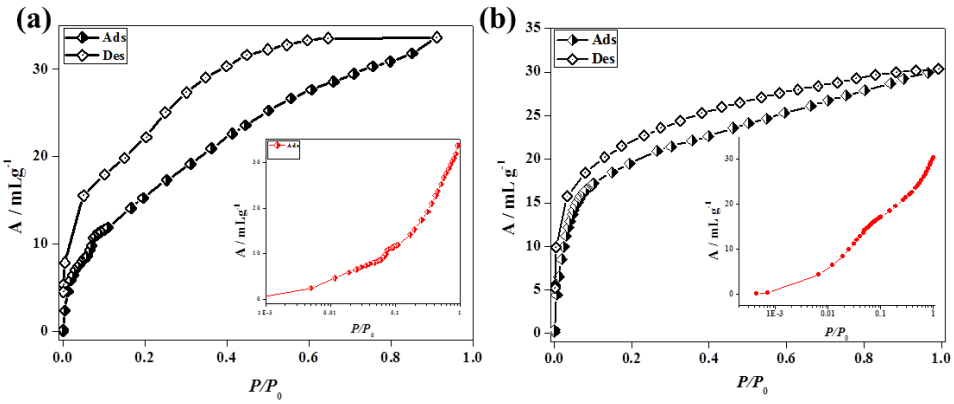

Figure 20: CO_2 adsorption profiles for (a) **1′** and (b) **2′** at 195 K. Inset shows pressure in logarithmic scale.

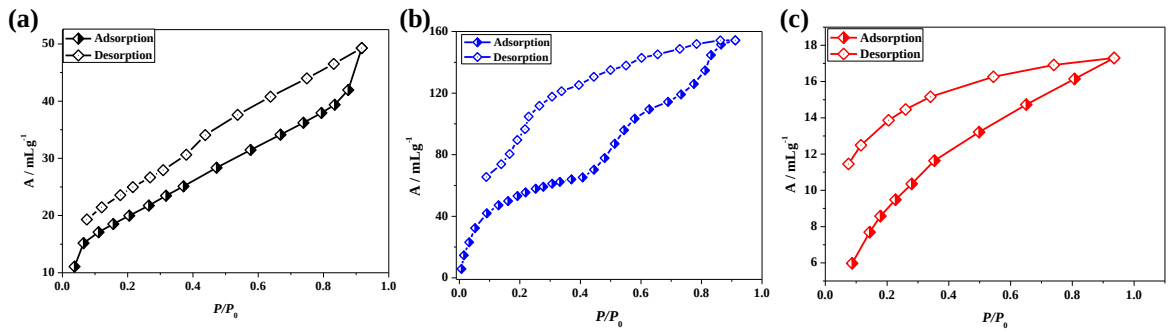

Figure 21: Vapour adsorption profiles of compound **1′**: (a) water; (b) methanol; (c) ethanol. P_0 values for water, methanol and ethanol are 3.17, 12.94 and 7.87 kPa, respectively.

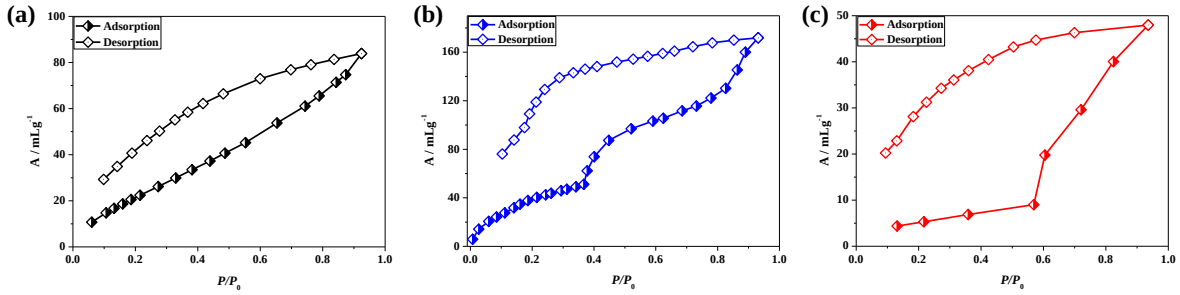

Figure 22: Vapour adsorption profiles of compound **2′**: (a) water; (b) methanol; (c) ethanol. P_0 values for water, methanol and ethanol are 3.17, 12.94 and 7.87 kPa, respectively.

4.3.5 Colour Tuning by Dye Inclusion

Compound **1** shows bright blue emission centered at 415 nm upon excitation at 350 nm (Figure 23a and 23b). This blue emission corresponds to bpdc linker and a slight red shift compared to free ligand suggests metal coordination (Figure 23b).

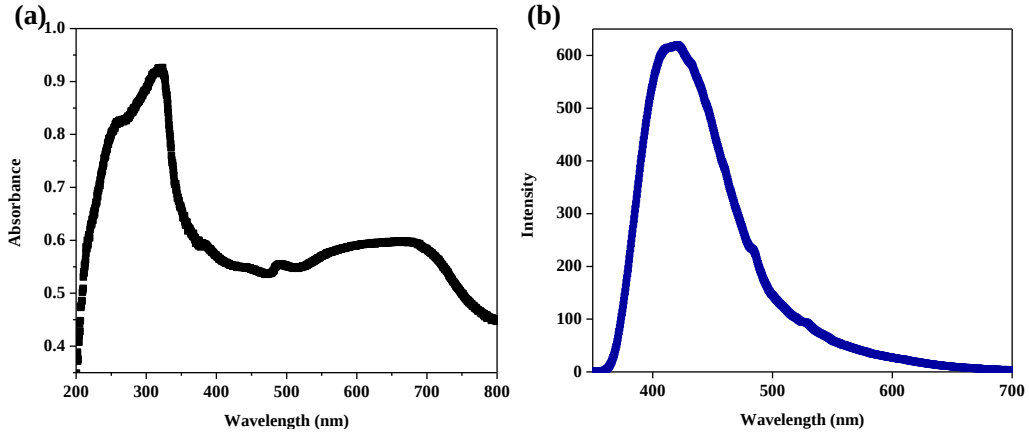

Figure 23: (a) Absorbance and (b) emission spectra of compound **1**.

The bright blue emission, porous nature of the framework and aromatic electron cloud rich pore surface propelled us to study dye inclusion properties of the framework. Further an optimum absorbance spectrum that partially overlaps with the emission spectrum of the donor framework is a crucial requirement to achieve tuneable emission characteristics. Considering the above criteria we preferred acridine orange (AO) which has well separated absorbance and emission band, partial overlap of its absorbance profile with emission profile of the framework and a comparable molecular dimension (13×6 $Å^2$) to the pore dimension of the as-synthesized framework (Figure 24).

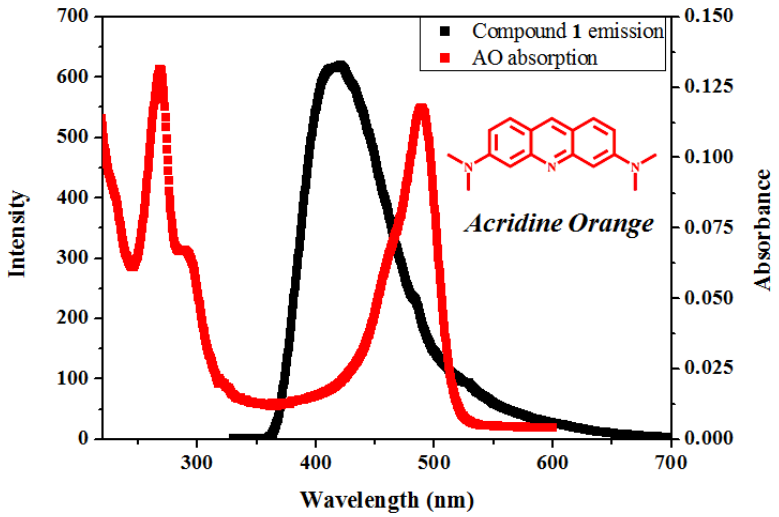

Figure 24: Partial overlap of compound **1** emission and AO absorbance; Inset figure shows the chemical structure of AO dye.

Four different AO included compounds were prepared with dye percentages 0.125 (**1a**), 0.32 (**1b**), 0.46 (**1c**) and 0.65 % (**1d**). In case of **1a**, the absorbance spectrum clearly shows additional absorbance peak at 500 nm indicating presence of AO (Figure 25a). Upon excitation at 350 nm a strong emission centered at 550 nm corresponding to the incorporated dye and comparatively a weak emission centered at 400 nm corresponding to framework is observed (Figure 25b). This observation suggests Förster energy transfer from the donor framework to the acceptor dye which leads to a green emission with CIE coordinates 0.34/0.50 (Figure 25c). The excitation spectrum monitored at 550 nm shows maximum intensity at 500 nm and very weak intensity at ~ 330 nm corresponding to donor absorbance (Figure 25d). This suggests an inefficient energy transfer. Increasing the dye amount in **1b** leads to more intense emission at 540 nm (λ_{ex}=350 nm) and also comparatively intense band at 330 nm (λ_{mon}= 550 nm) indicating a more efficient energy

transfer process (Figure 24a-25b). This leads to a dull green emission with CIE coordinates 0.34/0.48 (Figure 24c). Excitation spectrum (λ_{mon} = 550 nm) reveals a comparatively stronger intensity at 330 nm indicating better energy transfer efficiency than in **1a** (Figure 25d). The other two AO included compound 1 (**1c** and **1d**) also follows the same trend with CIE coordinates 0.32/0.46 and 0.38/0.52. To further prove the energy transfer process we carried out fluoroscence life time measurements of **1**, **1a**, **1b**, **1c** and **1d**. Monitoring the decay profile at 400 nm for **1**, **1a-1d** suggests with that increasing dye concentration, framework life time decreases from 3.65 ns to 3.6, 3.35, 2.2 and 1.00 ns, respectively (Figure 26).

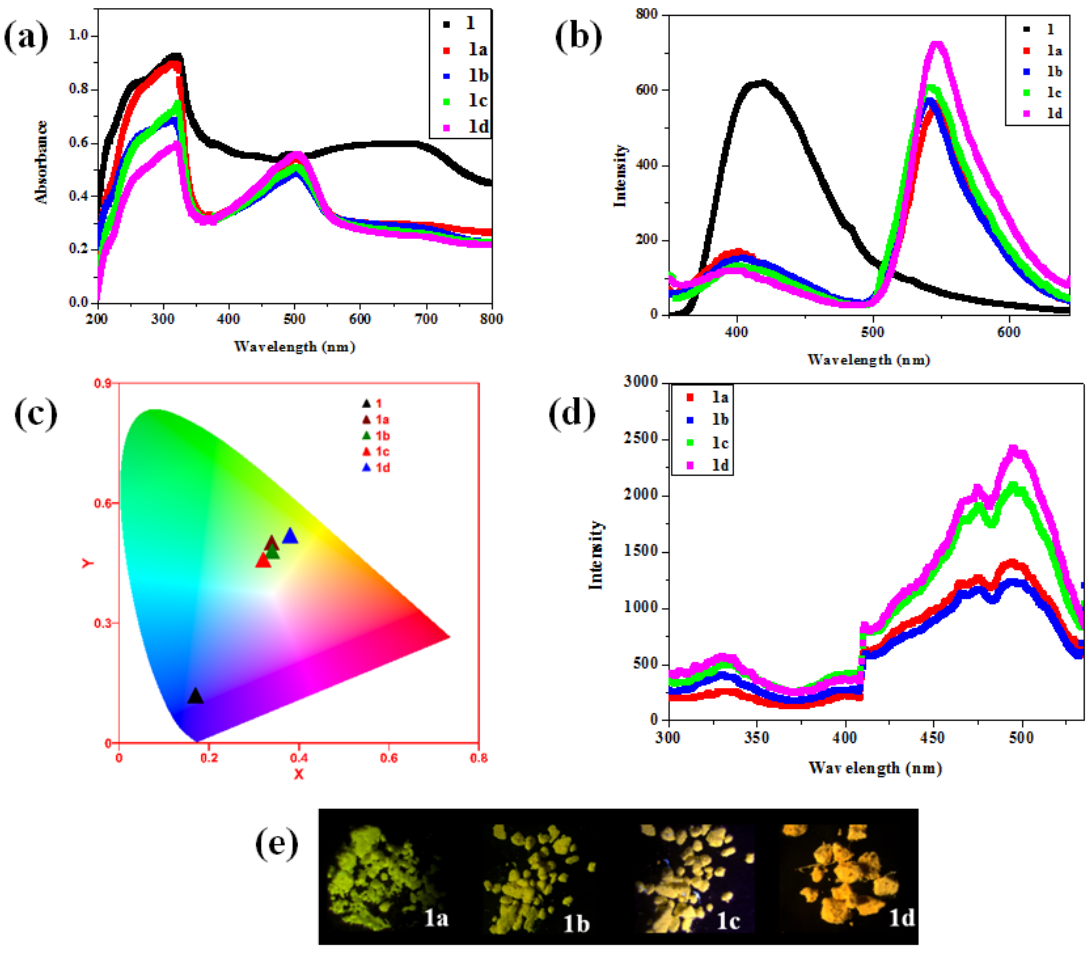

Figure 25: (a) UV-vis spectra of **1** and **1a-1d**; (b) Emission spectra of **1** and **1a-1d** upon excitation at 350 nm; (c) CIE graph of **1** and **1a-1d**; (d) Excitation spectrum of **1a-1d** monitored at 550 nm; (e) Picture shows the emission colour of **1a-1d** under UV light in solid state.

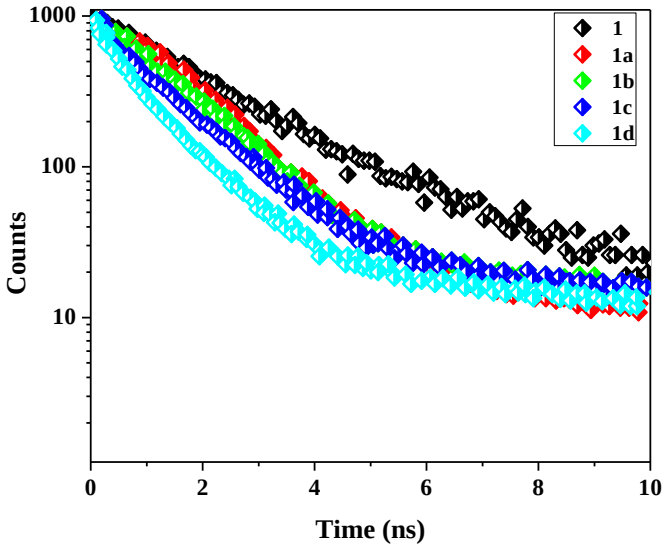

Figure 26: Fluoroscence lifetime decay profile for **1** and **1a-1d** monitored at 400 nm.

Along with the amount of dye, shape and size of the pore structure might also play an important role to determine the energy transfer efficiency and finally the emission colour as the FRET process is highly sensitive to the distance and dipole-dipole interactions between donor and acceptor. Compound **2**, which has a slightly different pore structure, was utilized for this study. **2** shows emission band around 390 nm upon excitation at 350 nm (Figure 27). We have further checked the overlap of the framework emission spectrum and AO absorbance, which suggest partial overlap (Figure 28). We have synthesized AO included compound **1** with varying dye percentages; 0.125 (**2a**) and 1.24 % (**2b**) AO respectively. The UV spectra of the two compounds show the presence of characteristic AO absorbance peak at 500 nm (Figure 29a). Emission spectra show that with increasing dye concentration, emission band at 550 nm rises and the framework emission band at 390 nm has lesser intensity (Figure 29b). This dual emission feature is similar to **1a-1d** but with lesser concentration of AO dye in compound **1** we could achieve bright yellow emission in case of **1d**. The CIE coordinates of **2a** and **2b** are 0.32/0.47 and 0.38/0.51 respectively (Figure 29c). Presence of energy transfer phenomena in the compounds were confirmed from the excitation spectra. With increasing dye concentration, intensity at 330 nm increases suggesting more efficient energy transfer from donor framework to the acceptor dye (Figure 29d). The fluoroscence decay profiles further support it. Monitoring the decay profile at 380 nm for **2**, **2a** and **2b** suggests with increasing dye concentration, framework life time decreases from 3.5 ns to 3.0 and 1.8 ns, respectively (Figure 30). More efficient energy transfer in case of AO included

compounds of **2** might be due to better spectral overlap or closer donor-acceptor distances.

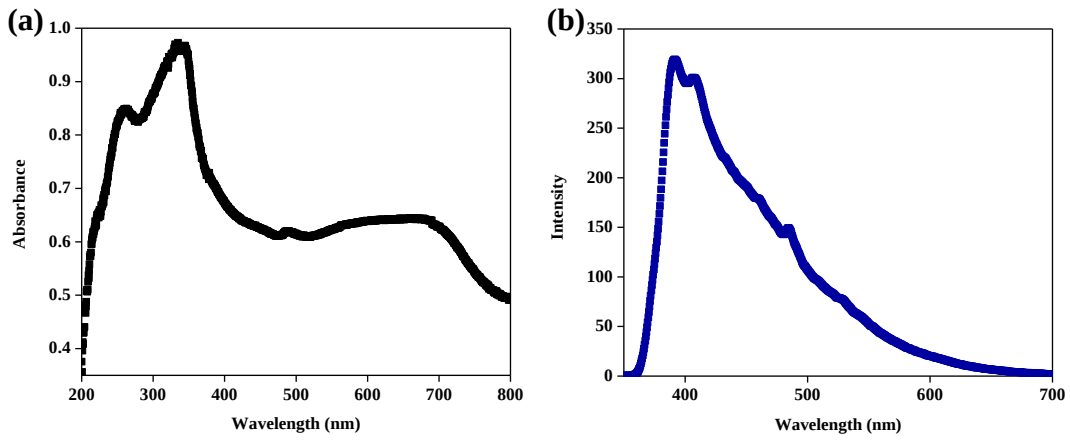

Figure 27: (a) Absorbance and (b) emission spectra of compound **2**.

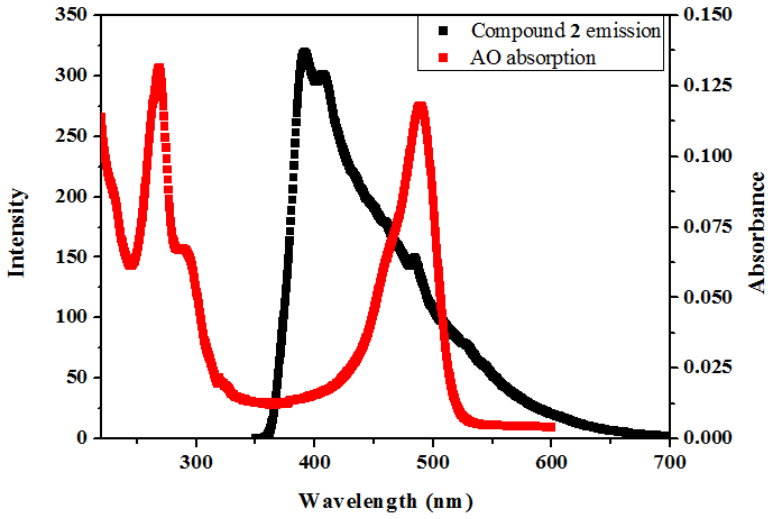

Figure 28: Partial overlap of compound **2** emission and AO dye absorbance.

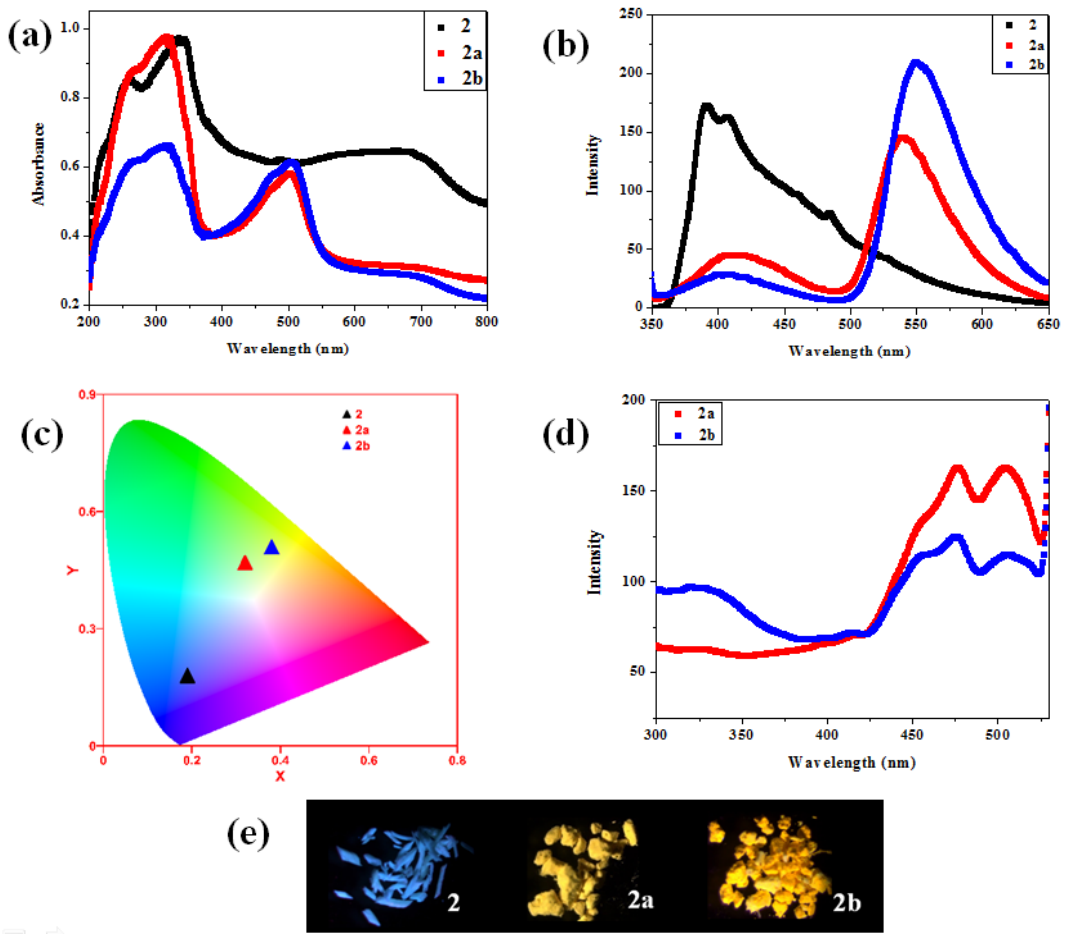

Figure 29: (a) UV-vis spectra of **2**, **2a** and **2b**; (b) Emission spectra of **2**, **2a** and **2b** upon excitation at 350 nm; (c) CIE graph of **2**, **2a** and **2b**; (d) Excitation spectrum of **2a** and **2b** monitored at 550 nm; (e) Picture show the emission colour of **2**, **2a** and **2b** under UV light in solid state.

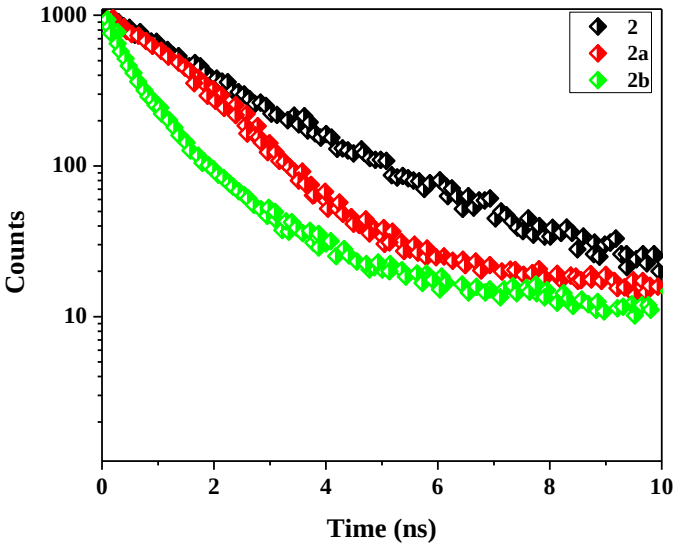

Figure 30: Fluoroscence lifetime decay profile for **2**, **2a** and **2b** monitored at 380 nm.

4.4 Conclusions

In conclusion we have synthesized two new 1D coordination polymers, **1** and **2** which self-assembles via π···π interactions to form 3D supramolecular structure with large one dimensional distorted channels. Both the frameworks after desolvation undergo structural reorganization leading to a structural contraction as realized from the PXRD studies and CO_2 adsorption isotherms. The solvent vapour (water, methanol and ethanol) adsorption profiles suggest flexible and hydrophobic pore surface of both the frameworks. Different percentages of AO dye inclusions in **2** show dual emission via partial energy transfer from framework to the included dye leading to light and bright yellow emission. In case of **1**, even smaller percentages of inclusions give rise to bright yellow emission. This is attributed to the better energy transfer efficiency due to good spectral overlap compared to AO included compound **2**. This sort colour tunability in PCP using partial energy transfer from host framework to non-covalently encapsulated guest (dye) is unprecedented and opens up a new route to fabricate solid state light emitting materials.

4.5 References

1 (a) S. Kitagawa, R. Kitaura and S. Noro, *Angew. Chem. Int. Ed.*, 2004, **43**, 2334; (b) D. N. Dybtsev, H. Chun and K. Kim, *Angew. Chem. Int. Ed.*, 2004, **116**, 5143.

2 (a) J. Li, R. J. Kuppler and H. Zhou, *Chem. Soc. Rev.*, 2009, **38**, 1477; (b) L. E. Kreno, K. Leong, O. K. Farha, M. Allendorf, R. P. V. Duyne and J. T. Hupp , *Chem. Rev.*, 2012, **112**, 1105; (c) L. Ma, C. Abney and W. Lin, *Chem. Soc. Rev.*, 2009, **38**, 1248; (d) R. C. Huxford, J. D. Rocca and W. Lin, *Curr. Opin Chem Biol.*, 2010, **14**, 262.

3 (a) Z. Chen, Y. Sun, L. Zhang, D. Sun, F. Liu, Q. Meng, R. Wang and D. Sun, *Chem. Commun.*, 2013, **49**, 11557; (b) B. Chen, L. Wang, F. Zapata, G. Qian and E. B. Lobkovsky, *J. Am. Chem. Soc.*, 2008, **130**, 6718; (c) Y. Li, S. Zhang and D. Song, *Angew. Chem. Int. Ed.*, 2013, **52**, 710; (d) C. Y. Lee, O. K. Farha, B. J. Hong, A. A. Sarjeant, S. T. Nguyen and J. T. Hupp, *J. Am. Chem. Soc.*, 2011, **133**, 15858; (e) M. Wang, S. Guo, Y. Li, L. Cai, J. Zou, G. Xu, W. Zhou, F. Zheng and G. Guo, *J. Am. Chem. Soc.*, 2009, **131**, 13572.

4 (a) A. H. Mueller, M. A. Petruska, M. Achermann, D. J. Werder, E. A. Akhadov, D. D. Koleske, M. A. Hoffbauer and V. I. Klimov, *Nano Lett.*, 2005, **5**, 1039; (b) V. L. Colvin,

M. C. Schlamp and A. P. Alivisatos, *Nature*, 1994, **370**, 354; (c) R. C. Evans, L. D. Carlos, P. Douglas and J. Rocha, *J. Mater. Chem.*, 2008, **18**, 1100.

5 (a) M. T. Bernius, M. Inbasekaran, J. M. O'Brien and W. Wu, *Adv. Mater.*, 2000, **12**, 1737; (b) M. Berggren, O. Inganas, G. Gustafsson, J. Rasmusson, M. R. Anderson, T. Hjertberg and O. Wennerstrom, *Nature*, 1994, **372**, 444; (c) S. Mohapatra, S. Adhikari, H. Riju and T. K. Maji, *Inorg. Chem.*, 2012, **51**, 4891; (d) A. R. Ramya, D. Sharma, S. Natarajan and M. L. P. Reddy, *Inorg. Chem.*, 2012, **51**, 8818.

6 (a) B. W. D Andrade and S. R. Forrest, *Adv. Mater.*, 2004, **16**, 1585; (b) J. Thompson, R. I. R. Blyth, M. Mazzeo, M. Anni, G. Gigli, and R. Cingolani, *Appl. Phys. Lett.*, 2001, **79**, 560.

7 (a) X. P. Zhang, D. Wang, Y. S. H. Tian, J. Lin, Y. L. Fenga and J. Cheng, *Dalton Trans.*, 2013, **42**, 10384; (b) Z. Liu, M. Wu, S. Wang, F. Zheng, G. Wang, J. Chen, Y. Xiao, A. Wu, G. Guo and J. Huanga, *J. Mater. Chem. C*, 2013, **1**, 4634.

8 (a) N. Mizoshita, Y. Goto, T. Tani and S. Inagaki, *Adv. Mater.*, 2009, **21**, 4798; (b) L. Sun, H. Xing, Z. Liang, J. Yu and R. Xu, *Chem. Commun.*, 2013, **49**, 11155.

9 SMART (V 5.628), SAINT (V 6.45a), XPREP, SHELXTL; Bruker AXS Inc. Madison, Wisconsin, USA, 2004.

10 G. M. Sheldrick, Siemens Area Detector Absorption Correction Program, University of Göttingen, Göttingen, Germany, 1994.

11 A. Altomare, G. Cascarano, C. Giacovazzo and A. Gualaradi, *J. Appl. Cryst.*, 1993, **26**, 343

12 G. M. Sheldrick, SHELXL-97, Program for Crystal Structure Solution and Refinement; University of Göttingen, Göttingen, Germany, 1997

13 A. L. Spek, *J. Appl. Cryst.*, 2003, **36**, 7.

14 L. J. Farrugia, WinGX–A Windows Program for Crystal Structure Analysis, *J. Appl.Crystallogr.*, 1999, **32**, 837.

Chapter: 5

A luminescent metal-organic complex for ratiometric Al^{3+} sensing

Summary

In this chapter we have chosen a new electron deficient linker, bipyridophenazine (bpz) which can interact with electron rich anthracene dicarboxylate (adc) in a Zn(II) complex. A novel highly luminescent tetrameric complex, $\{[Zn_4(adc)_3(bpz)_6(NO_3)_2]\cdot 2H_2O\}$ (**1**) was synthesized by solvothermal technique. **1** shows bright red emission due to the presence of adc:bpz exciplex which is formed by stacking of two neighbouring tetramers. The further growth of the tetramer is blocked by the two bpz linkers present at each end of the tetramer. It forms a 3D supramolecular structure through π···π and C-H···π interactions. The exciplex is sensitized by the coordinated adc monomer emission through FRET process. This complex can be used for selective ratiometric detection of Al^{3+} among a number of metal ions. Upon addition of Al^{3+} to the dispersed solution of compound **1** in methanol leads to change in the emission of solution from red to cyan. Selective sensing of this biologically toxic metal ion is possible at a very low concentration of 10 nM.

5.1 Introduction

Organic chromophore based molecular sensors are well-known and widely used for selective recognition of biological and chemical species.[1] Exploiting the non-covalent molecular interactions; such as hydrogen bonding, π-π and van der Waals interactions the organic molecular probes transduct the information based on change in emission intensities or new emission through excited state photophysical process such as exciplex formation or change in visible colour due to ground state interactions. It is worth to mention that emission or visible colour change is the most efficient and easily detectable outputs that can be achieved for molecular sensors. Using this strategy various organic chromophore based molecular sensors have been deployed for selective sensing of various biologically toxic metal ions such as Al^{3+}, Cu^{2+}, Zn^{2+} etc.[2] Among these Al^{3+} is one of the most abundant in the bio-system and known for its toxicity. Diseases like headaches, anaemia, speech problem, softening of bone, rickets, colic, and Alzheimer can be caused by extreme Al^{3+} exposure.[3] Hence, to develop an effective method to detect such toxic Al^{3+} is important and to serve this purpose various molecular probes have been reported in literatures.[4a] In most cases mechanistic pathway involves charge transfer, electron transfer or energy transfer phenomena.[4b] Apart from purely organic based probes there are almost no reports with metal-organic hybrid systems with potential application in Al^{3+} sensing.

Use of lanthanide based coordination polymers (CPs) (read as metal-organic) as sensory material is well-known.[5] The lanthanide emission is sensitive to its coordination sphere and exploiting its high coordination number many metal ion, anion and solvent molecule sensing have been reported till date.[5] On the other hand organic linkers in metal organic systems are also sensitive to its microenvironment and hence can be used as sensing platform has not been properly exploited.[6] Here, in this chapter we have exploited the change in spatial organization of chromophoric linkers that lead to change in excited photophysical processes. Anthracene is a well-known organic chromophore which has a long lived excited state, high quantum yield and well separated absorption and emission band. This chromophore is also known to act as a good electron donor and hence can form excited state complex with a suitable acceptor. We have chosen a new electron deficient linker, bipyridophenazine (bpz) which can interact with electron rich anthracene. Self-assembly of anthracene dicarboxylic acid (adc), bpz and Zn(II) yields a tetrameric complex $\{[Zn_4(adc)_3(bpz)_6(NO_3)_2]\cdot 2H_2O\}$ (**1**) which forms 3D supramolecular structure

through π···π and C-H···π interactions. Compound **1** shows bright red emission due to the presence of anthracene:bpz exciplex formed by stacking of two neighbouring tetramers. Moreover an efficient energy transfer process also operates from remaining anthracene moiety to anthracene:bpz exciplex. Interestingly, this complex selectively sense biologically toxic Al^{3+} ion at a very low concentration of 10 nM. The emission of the complex changes from bright red to cyan in presence of Al^{3+} but does not show any change for other metal ions such as Ga^{3+}, In^{3+}, Ca^{2+}, Zn^{2+}, Cu^{2+}, Mn^{2+}, K^{+}, Na^{+}, Li^{+}, Ni^{2+}, Co^{2+} and Fe^{3+}.

5.2 Experimental section

5.2.1 Materials

All the reagents employed were commercially available and used as provided without further purification. Metal salts, 9,10-anthracenedicarboxylic acid, 1,10-phenanthroline-5,6-dione and *o*-phenylenediamine were obtained from Sigma Aldrich chemicals.

5.2.2 Physical Measurements

Elemental analysis was carried out using a Thermo Fischer Flash 2000 Elemental Analyzer. IR spectra were recorded on a Bruker IFS 66v/S spectrophotometer using KBr pellets in the region 4000–400 cm^{-1}. Thermogravimetric analysis (TGA) was carried out (Metler Toledo) in nitrogen atmosphere (flow rate = 50 mL min^{-1}) in the temperature range 30–700 °C (heating rate = 3 °C min^{-1}). Powder X-ray diffraction (PXRD) patterns of the products were recorded on a Bruker D8 Discover instrument using Cu−Kα radiation. The pattern agreed with those calculated from single crystal structure determination. Electronic absorption spectra were recorded on a Perkin Elmer Lambda 900 UV-VIS-NIR Spectrometer and PL spectra were taken with Perkin-Elmer model LS 55 luminescence spectrometer. Fluorescence decay was recorded in a time correlated single photon counting spectrometer of Horiba-Jobin Yvon with 350-450 nm picosecond Ti-saphhire laser. Energy dispersive analysis of X-rays (EDAX) was carried out using Leica-S440I field emission scanning electron microscopy (FESEM). NMR spectra were obtained with a Bruker AVANCE 400 (400 MHz) Fourier transform NMR spectrometer with chemical shifts reported in parts per million (ppm).

5.2.3 X-ray Crystallography

X-ray single crystal structural data of **1** was collected on a Bruker Smart-CCD diffractometer equipped with a normal focus, 2.4 kW sealed tube X-ray source with graphite monochromated Mo-Kα radiation (λ = 0.71073 Å) operating at 50 kV and 30 mA. The program SAINT[7] was used for integration of diffraction profiles and absorption correction was made with SADABS[8] program. All the structures were solved by SIR 92[9] and refined by the full matrix least-squares method using SHELXL-97.[10] All the hydrogen atoms were fixed by HFIX and placed in ideal positions. Potential solvent accessible area or void space was calculated using the PLATON multipurpose crystallographic software.[11] All crystallographic and structure refinement data of **1** are summarized in Table 1. Selected bond lengths and angles for **1** are given in Tables 2-3. All calculations were carried out using PLATON and WinGX system, Ver 1.70.01.[12]

5.2.4 Syntheses

5.2.4.1 Synthesis of Bipyridophenazine (bpz)

10 mL methanol solution of o-phenylenediamine (0.054 g, 0.5 mmol) was added dropwise to *o*-phenanthroline-5,6-dione (0.105 g, 0.5 mmol) dissolved in 15 mL methanol in a round bottom flask. The reaction mixture was refluxed for 2 hours at 60 °C and then cooled to room temperature. Light brown precipitate formed was filtered and dried to get the product, bpz. Yield: 95%; Characterized by ^{1}H-NMR spectrum (Figure 1).

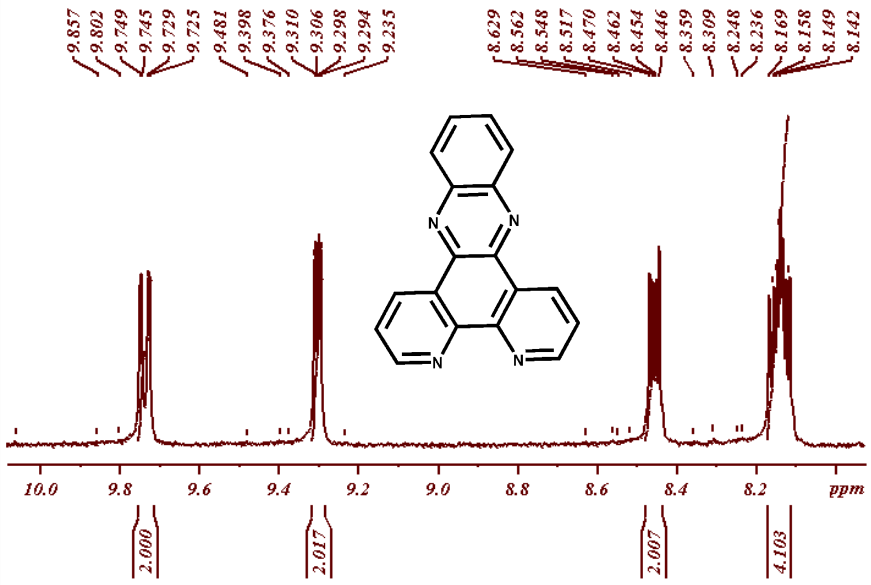

Figure 1: ^{1}H-NMR spectrum of bpz in D_6-DMSO.

5.2.4.2 Synthesis of $[\{Zn_4(adc)_3(bpz)_6(NO_3)_2\}\cdot 2H_2O]$ (1)

Anthracene dicarboxylate (0.020 g, 0.075 mmol) and bipyridophenazine (0.042 g, 0.15 mmol) were dissolved in a solvent mixture of 10 mL dimethylformamide (DMF) and 2 mL water in a glass vial. Then $Zn(NO_3)_2\cdot 6H_2O$ (0.030 g, 0.1 mmol) was added to the above ligand solution and sonicated before the vial was sealed and kept in an oil bath at 90 °C for 3 days. Good quality red coloured crystals were obtained which were washed with fresh methanol before collecting single-crystal X-ray diffraction data. Yield of **1**: 61 %; Anal. Calcd. for $C_{156}H_{88}N_{26}O_{20}Zn_4$: C, 64.43; H, 3.03; N, 12.53. Found C, 65.01; H, 3.02; N, 11.98. FT-IR (KBr pellet, 4000−400 cm^{-1}): 3450 (b), 3105 (w), 3072 (m), 3040 (s), 2962 (s), 2932 (m), 2900 (s), 1617 (s), 1606 (w), 1590 (s), 1565 (w), 1540 (w), 1507 (s), 1489 (s), 1474 (s), 1443 (s), 1409 (s), 1383 (s), 1372 (w), 1344 (s), 1313 (s), 1295 (w), 1252 (s), 1233 (m), 1211 (s), 1192 (s), 1179 (m), 1168 (w), 1160 (m), 1143 (m), 1121 (s), 1077 (s), 1058 (m), 1041 (w), 1024 (s), 1016 (w), 991 (m), 954 (s), 918 (w), 882 (s), 846 (s), 819 (w), 802 (s), 776 (s), 736 (s), 719 (s), 694 (w), 683 (s), 657 (w), 652 (w), 633 (s), 602 (b), 556 (m), 547 (m), 520 (b), 504 (w), 421 (s).

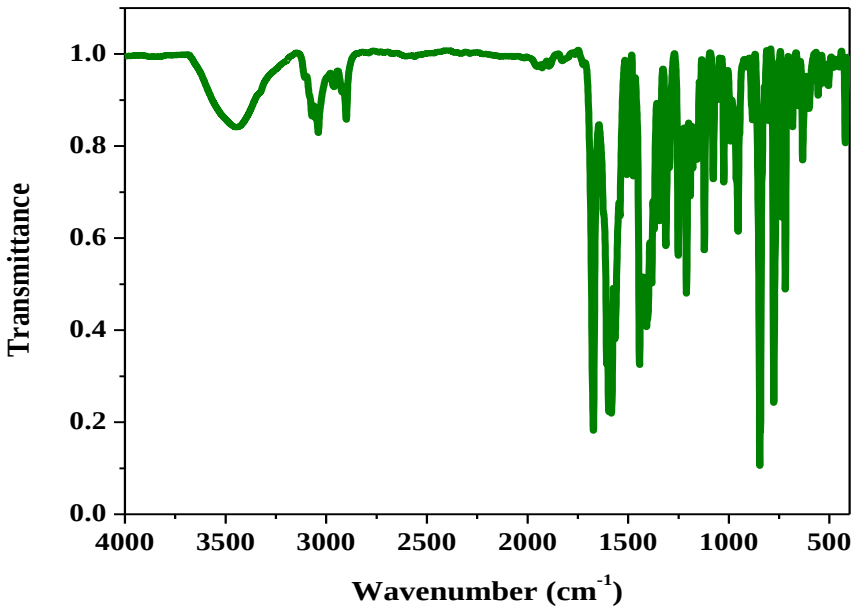

Figure 2: FT-IR spectrum of compound **1**.

5.3 Results and Discussion

5.3.1 Structural description of $[\{Zn_4(adc)_3(bpz)_6(NO_3)_2\}\cdot 2H_2O]$ (1)

Compound **1** crystallizes in monoclinic $P2_1/n$ space group and structure determination by X-ray crystallography reveals that there are two types of crystallographically independent Zn(II) atoms in a tetramer; Zn1 and Zn2 which are connected through one adc moiety (Figure 3). Zn1 centers remain at the two ends of the tetramer and are hexacoordinated; four nitrogens from two bpz and two oxygens from one adc carboxylate group. Zn2 centers are pentacoordinated by two nitrogen atoms from one bpz, two oxygens from two adc carboxylates and one oxygen from $-NO_3$ (Figure 3). The two Zn2 centers in the tetramer are linked by the carboxylate groups of an adc. There are two types of adc linker; one that remains at the center of the tetramer shows monodentate binding for both the carboxylate groups while the other two adc have one chelating and one monodentate carboxylate group. The terminal Zn1 centers are coordinated by two chelating bpz and thus blocks the further growth of the structure leading to a tetramer. The tetramer features four pendent oxygens from four carboxylate groups and two oxygens from two coordinated nitrate groups. Interestingly, there are several non-covalent interactions between the tetramers that extend the structure in three dimensions. The central adc linker is sandwiched between two terminal bpz aromatic rings from two different tetramers ($\pi\cdots\pi$ distance is 3.594 Å) (Figure 4a). Those two end bpz then stacks above other five stacked bpz aromatic rings from five different tetramers in a offset face-to-face fashion to form a continuous $\pi\cdots\pi$ stacked array of $(bpz:bpz:bpz:bpz:bpz:bpz:adc)_n$ (Figure 4b). Most importantly, the two terminal adc rings do not undergo any face-to-face interactions but have weak hydrogen bonding interactions between neighbouring bpz nitrogen (C-H$\cdots$N3 ~ 2.716 Å) and nitrate oxygen (C-H$\cdots$O9 ~ 2.582 Å) (Figure 4c). In combination of all these non-covalent interactions a 3D supramolecular structure is thus formed.

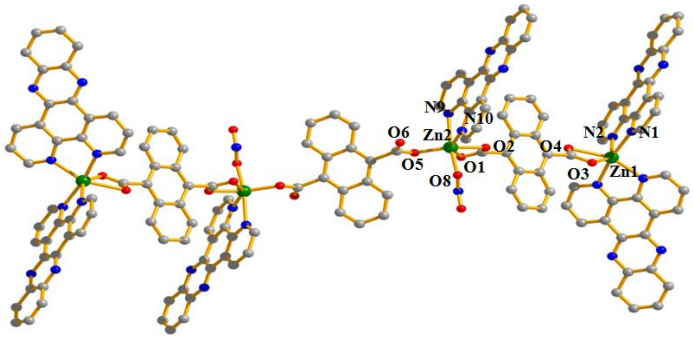

Figure 3: Coordination environment of Zn1 and Zn2 in tetramer of **1**.

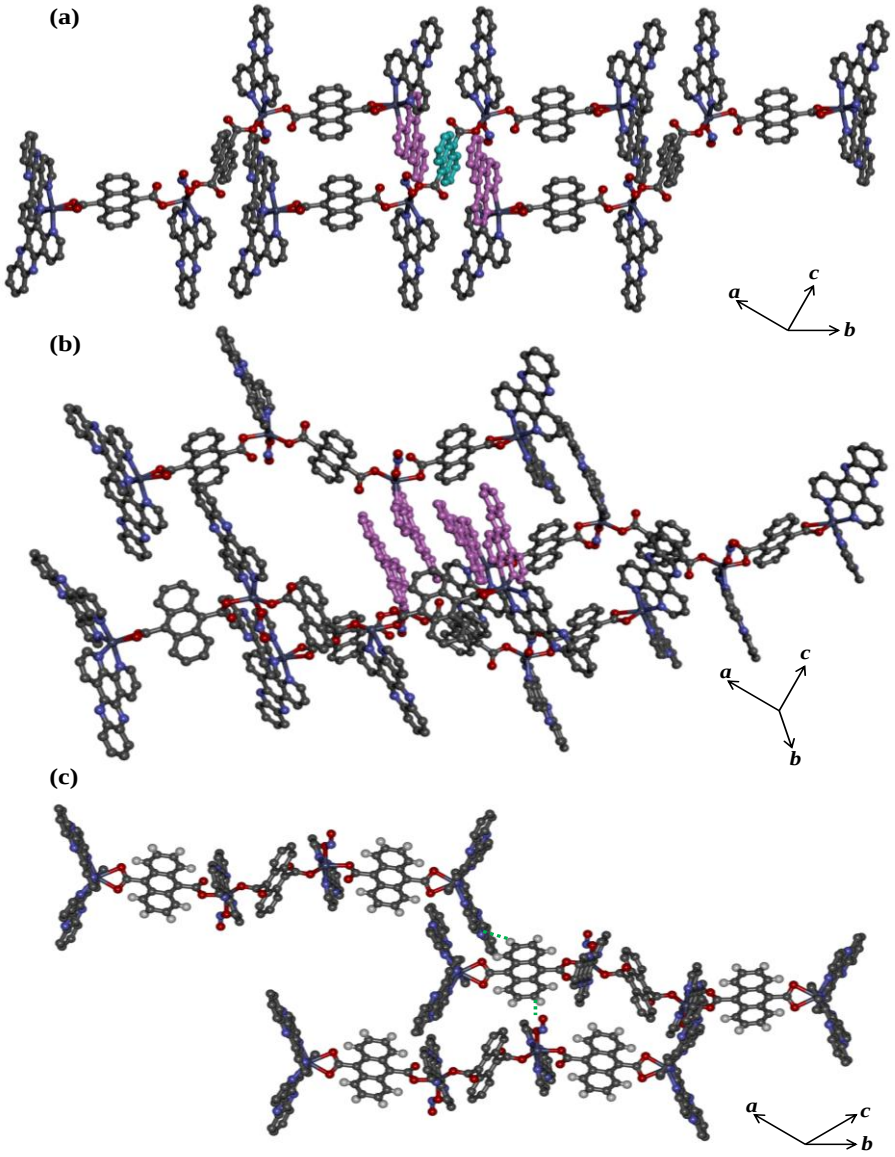

Figure 4: Structural details of **1**: (a) bpz:adc:bpz face-to-face interaction (bpz= pink and adc = cyan); (b) Among six four bpz stack face-to-face (shown in pink); (c) Hydrogen bonding between C-H and NO_3 oxygen and bpz nitrogen (dotted lines are H-bonds).

Table 1: Crystal data and structure refinement parameters of **1**.

Parameters	**1**
Empirical formula	$C_{156}H_{88}N_{26}O_{20}Zn_4$
Formula weight	2905.52
Crystal system	Monoclinic
Space group	$P2_1/n$
a, Å	18.6944(3)
b, Å	17.1337(3)
c, Å	20.3166(3)
β, deg	97.552(1)
V, Å^3	6451.05(18)
Z	2
T, K	293
μ,mm^{-1}	0.817
D_{calcd},g/cm^3	1.443
F (000)	2796
Reflections [$I>2\sigma(I)$]	3569
Unique reflections	1489
Total reflections	2563
R_{int}	0.045
GOF on F^2	0.95
$R_1[I>2\sigma(I)]^a$	0.0265
R_w[all data]^b	0.156
$\Delta\rho$ max/min [e Å^{-3}]	0.236/0.159

$^aR_1 = \sum||F_o|-|F_c||/\sum|F_o|$; $^bR_w = [\sum\{w(F_o^2-F_c^2)^2\}/\sum\{w(F_o^2)^2\}]^{1/2}$

5.3.2 PXRD Analysis and Thermal Stability

The PXRD pattern of as-synthesized compound **1** matches well with the simulated pattern suggesting phase purity of the bulk product (Figure 5). To verify the thermal stability of compound **1** TG analysis was carried out. The TGA profile shows a weight loss of ~ 1.18 weight% in the temperature range of 30-170 °C which corresponds to the loss of **2** guest water molecules (calc. 1.23 weight%) (Figure 6). The desolvated framework is stable upto 280 °C and disintegrates upon further heating.

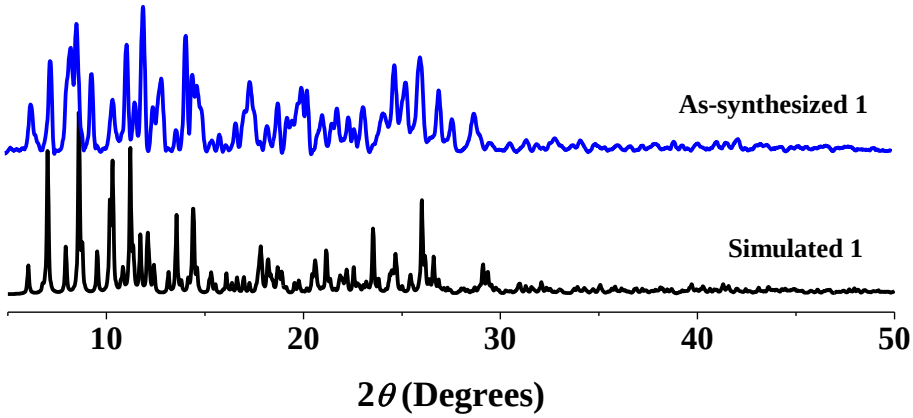

Figure 5: PXRD patterns of simulated and as-synthesized **1**.

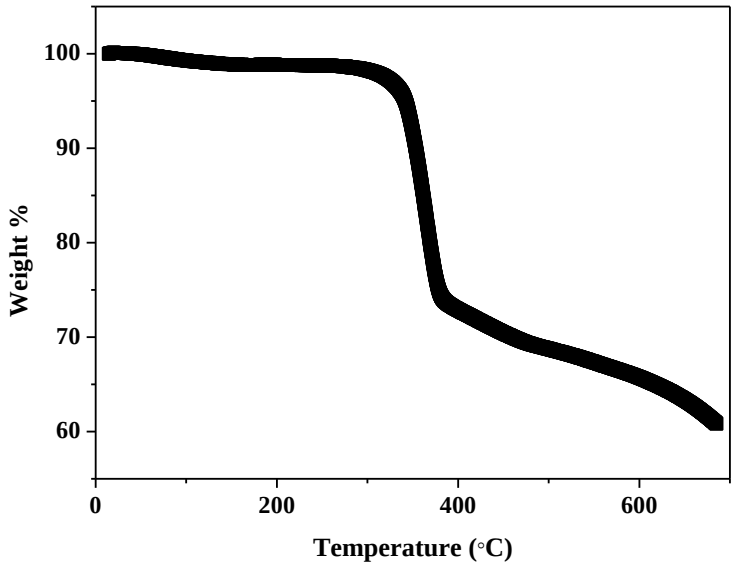

Figure 6: TGA profile of compound **1**.

5.3.3 Photophysical Properties of 1

The absorbance spectrum of compound **1** showed very broad nature with maximum around 526 nm (Figure 7a). Such broad spectrum and huge intensity at the visible region suggest presence of ground state interactions in **1**. The dark red colour of **1** also suggests the same (Figure 8a). Excitation of **1** at 400 nm shows a broad featureless emission spectrum with maxima centered at 585 nm (Figure 7b and 8b). This bright red emission corresponds to the presence of excited state photophysical processes. The excitation spectrum of **1** monitored at 620 nm shows two distinct peaks at 340 and 400 nm (Figure 9a). Moreover, we also observed a broad shoulder from 420 to 500 nm region. These observations clearly suggest presence of bpz:anthracene 2:1 exciplex formation; bpz acts as acceptor and adc as donor. Such huge spectral shift of anthracene emission (~ 400 nm) from blue to red region is due to a very strong association at the ground state itself. The fluoroscence life time observed for this exciplex with charge transfer characteristic is ~ 16 ns, which is sufficiently high and unprecedented in similar system (Figure 9b). Further, a close inspection of the structure shows there are two anthracene cores (terminal) which are not in close contact with bpz to form any such excited state dimer or trimer and hence we should observe anthracene monomer emission in the emission spectrum. But even excitation upon 330 nm we do not observe any emission around 400 nm for anthracene monomer. Hence we propose there is an energy transfer phenomenon from free anthracenes to the exciplex. Here, anthracene acts as an antenna for energy transfer and this sort of observations are reported by our group previously in metal-organic complex. This is further supported by the sharp intensity observed at 330 nm in excitation spectrum monitored at 620 nm.

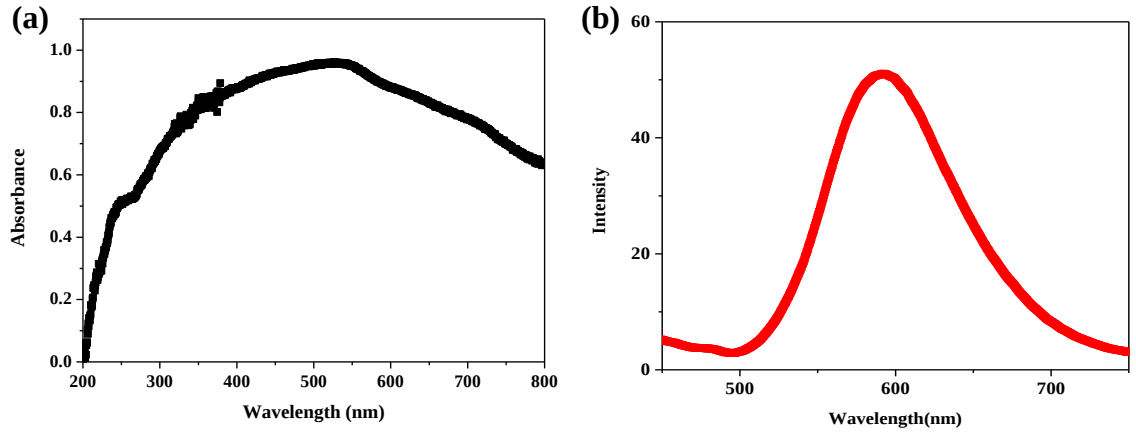

Figure 7: Absorbance (a) and emission (b) spectra of compound **1**.

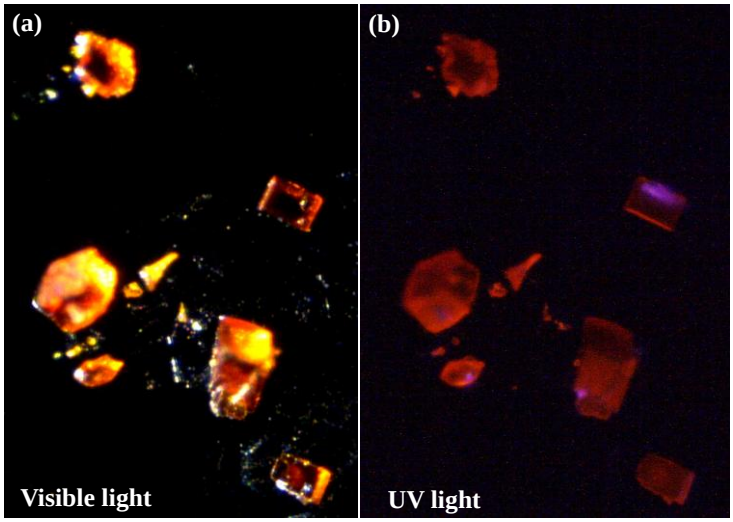

Figure 8: Pictures of compound **1** crystals under (a) visible light and (b) UV light.

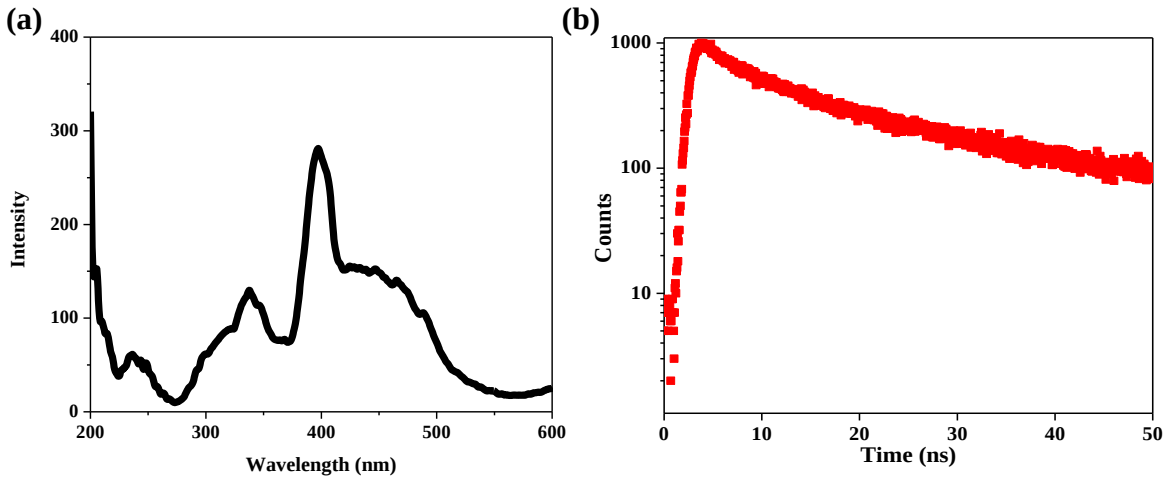

Figure 9: (a) Excitation spectrum of **1** monitored at 620 nm; (b) Fluoroscence life time spectrum of **1** monitored at 600 nm.

5.3.4 Metal Ion (Al^{3+}) Sensing

The tetramer contains several pendent oxygen atoms and the interesting photophysical processes that it shows prompted us to further investigate its response to various metal ions. To perform such studies we verified the stability of the tetramer in different solvents, such as,

acetonitrile, chloroform, chlorobenzene, DCM, DMF, ethanol, methanol and water. The emission spectra of dispersed solutions were recorded upon excitation at 400 nm (Figure 10). We observed only methanol solution spectrum exactly matches with that of the

compound **1** in solid state and hence it can be assumed that tetramer assembly is stable in methanol. While for other solvents an additional emission band arises around 450 nm which probably corresponds to coordinated anthracene emission. Appearance of anthracene emission corresponds to perturbation in energy transfer process.

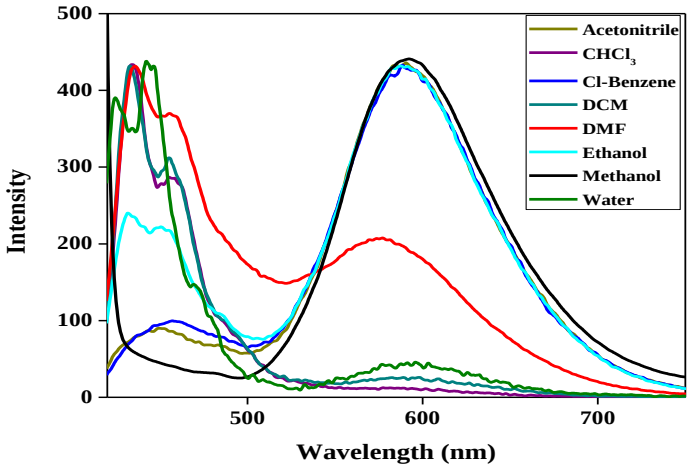

Figure 10: Emission spectra of **1** dispersed in different solvents upon excitation at 330 nm.

A 100 nM stock solution of compound **1** was prepared by dispersing in methanol and its emission response was observed after the addition of solutions of various metal ions. After addition of 10 nM Al^{3+} methanol solution a new emission peak with maxima centered at 460 nm arises and the emission maxima centered at 585 nm diminishes (Figure 11). With increase in concentration of Al^{3+} the 585 nm peak completely vanishes and maxima at 460 nm dominates. The emission of the solution changes from bright red to cyan colour (Inset Figure 11). Such huge shift (125 nm) of emission spectra is unusual and leads to a ratiometric sensing characteristics.

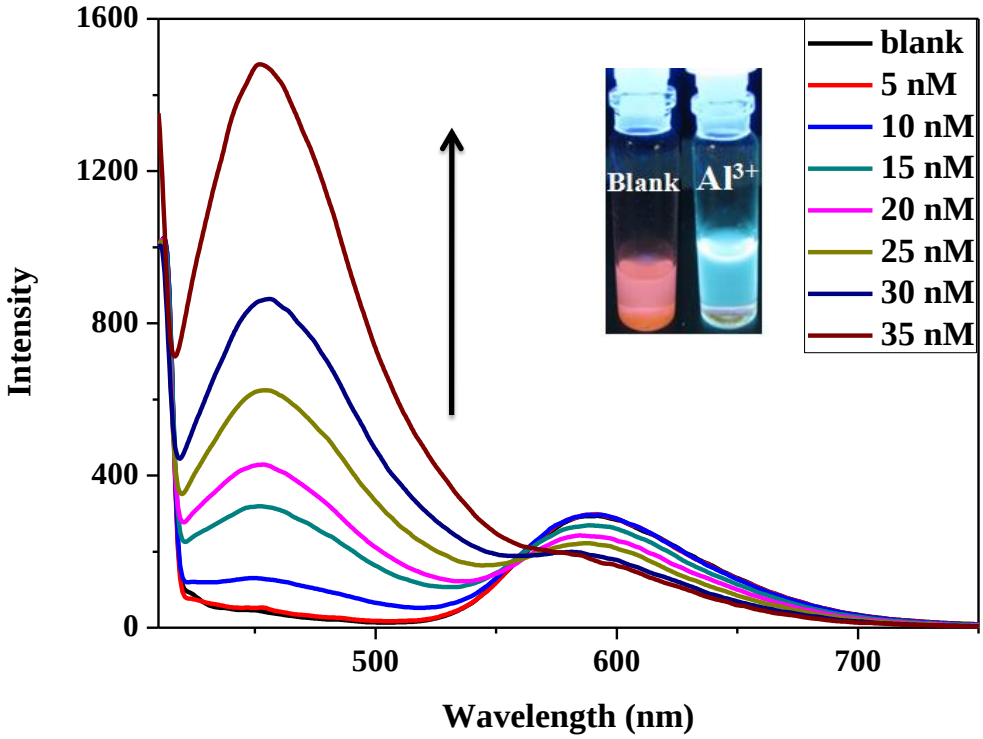

Figure 11: Fluorescence titration experiment: 10 nM of Al^{3+} solution was added each time. Inset shows colour change of solution of compound **1** (dispersed in methanol) upon addition of Al^{3+}.

For other metals of same group Ga^{3+} and In^{3+} no such trend was observed (Figure 12). On addition of transition metal ions such as Mn^{2+}, Fe^{3+},Co^{2+}, Ni^{2+} no changes were observed in the emission spectra (Figure 12). Only for Cu^{2+} there was a decrease in the intensity of emission maxima centered at 585 nm (Figure 13). After addition of 90 nM of Cu^{2+} solution ~ 17 % decrease in the emission intensity was observed. Such sort of emission quenching is common for d^9 metal ion as the emission energy is consumed by the d-d transition. For other systems like d^3–d^8 there is no change as these metal systems do not couple with the excited state chromophore. Other metal ions like Cd^{2+}, Zn^{2+}, Ca^{2+}, Mg^{2+}, K^+, Na^+ and Li^+ also do not change the emission spectra of **1** (Figure 12). Such observation confirms highly selective ratiometric detection of Al^{3+}. Even a small concentration of 10 nM in case of Al^{3+} brings drastic change in the emission spectrum.

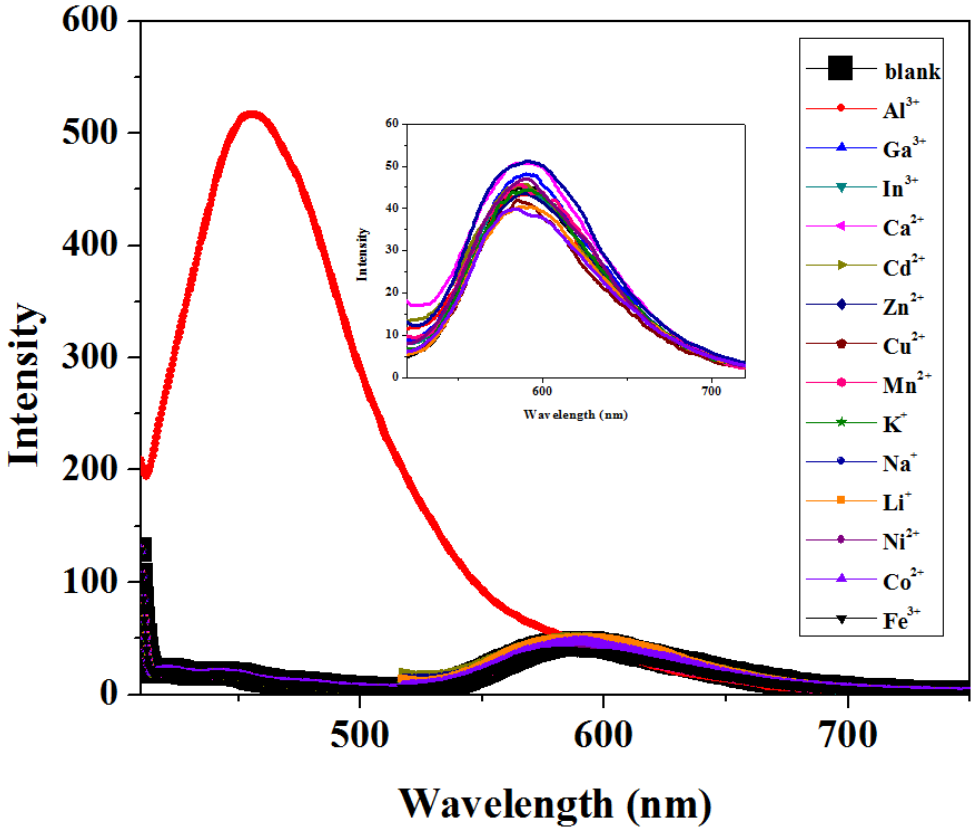

Figure 12: Emission spectra collected upon excitation at 400 nm: 40 nM of metal solutions (methanol) were added to 100 nM compound dispersed in methanol. Inset shows the magnified emission spectra suggesting that no significant change occurs after the addition of metal ions other than Al^{3+} to the methanol solution of compound **1**.

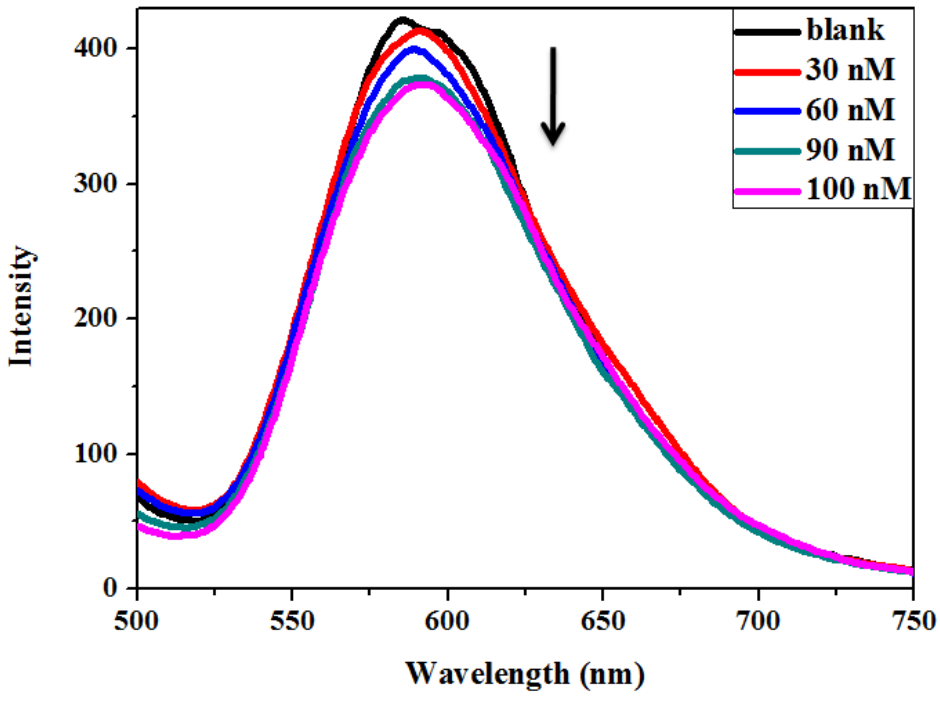

Figure 13: Emission spectra showing quenching of emission upon addition of Cu^{2+}.

5.3.5 Mechanistic Pathway

The unusual emission characteristic of Al^{3+} can be regarded as disruption in the packing in solid state of compound **1**. As the exciplex emission diminishes it can be concluded that two tetramers are not in close proximity which will help to form exciplex between anthracene and bpz. Moreover rise of the emission band with maxima around 460 nm can be attributed to the coordinated anthracene monomer emission. Complete breakdown i.e. release of anthracene molecules could have shifted the emission further in the blue region around 400 nm. Emission around 460 nm indicates typical metal coordinated anthracene emission which further suggests that disruption occurs in the packing only. The probable binding site of Al^{3+} is the pendent oxygen atom of carboxylate group (Figure 14a). And the disruption in the crystal packing is possibly directed by the coordination of Al^{3+} to these pendant oxygen sites of carboxylate functionality (Figure 14b).

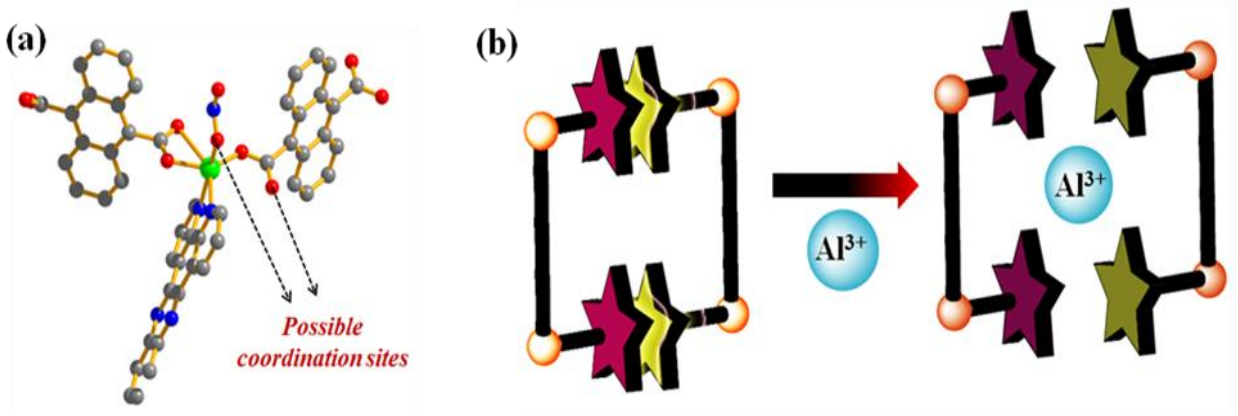

Figure 14: (a) Possible binding site of Al^{3+} is the pendent oxygen atom of carboxylate group; (b) Schematic representation of mechanistic pathway of Al^{3+} sensing.

To prove the presence of Al^{3+} and the assisted change in the structure of complex, we have carried out energy dispersive X-ray analysis (EDAX), FT-IR analysis, TGA analysis and PXRD studies. Concentration of Al^{3+} in the compound was found to be 0.68 atom% by energy dispersive X-ray analysis (EDAX). The PXRD patterns of Al^{3+} exposed compound **1** suggest huge structural change but retention of crystallinity (Figure 15a). Very slight change in the TGA profile of the Al^{3+} added compound **1**, confirms the fact that the crystallinity is retained and framework does not break (Figure 15b). The FT-IR spectrum of Al^{3+} added compound **1** shows significant change in the peaks corresponding to antisymmetric and symmetric stretching of carboxylate group (Figure 16). Further, O-NO_2 symmetric stretching peak of nitrate also shows a shift (Figure 15). These changes in

the IR spectra suggest that pendent oxygen atoms of carbonate and nitrate groups are the possible binding sites of Al^{3+} ions.

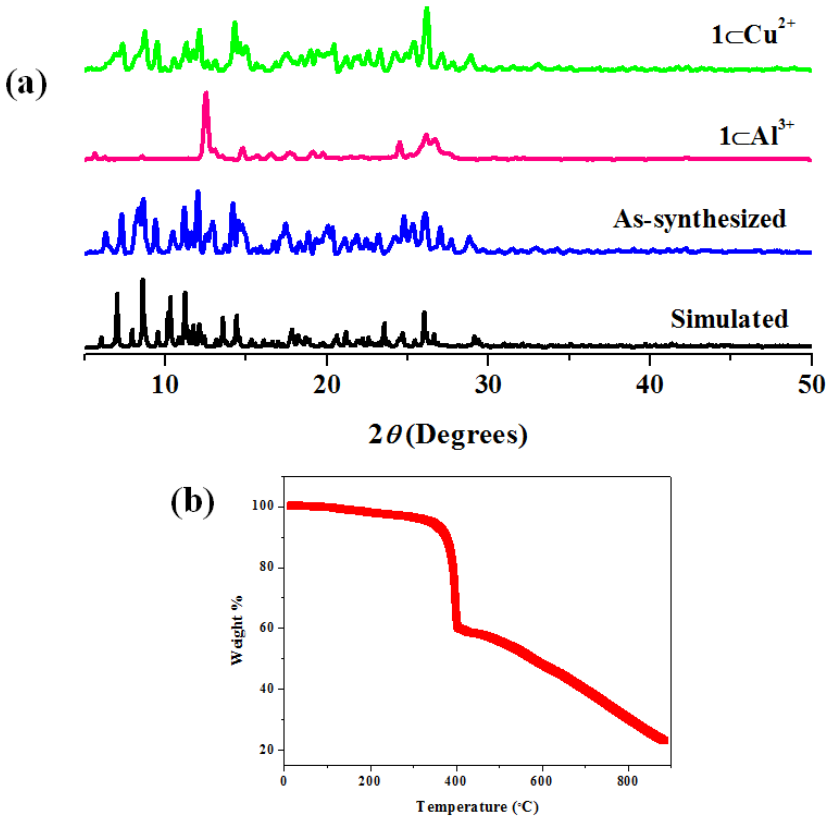

Figure 15: (a) PXRD patterns; (b) TGA profile of Al^{3+} added compound **1**.

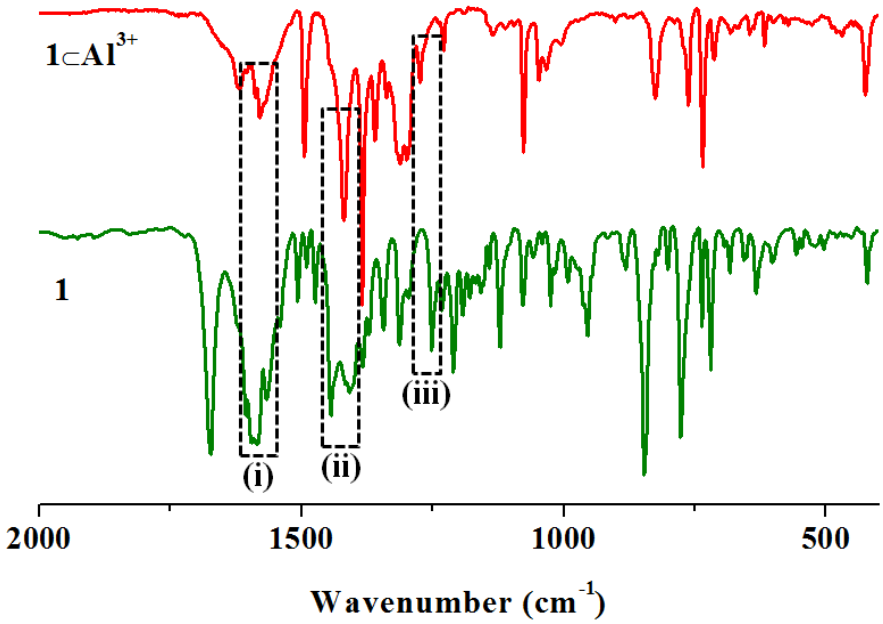

Figure 15: FT-IR spectra of compound **1** and **1⊂Al^{3+}** showing change in the (i) asymmetric stretching (~ 1600 cm^{-1}), symmetric stretching (~ 1400 cm^{-1}) of carboxylate group and (iii) O-NO_2 symmetric stretching (~ 1270 cm^{-1}) of nitrate group.

5.4 Conclusions

In conclusion, we have synthesized a novel metal organic highly luminescent complex, $[\{Zn_4(adc)_3(bpz)_6(NO_3)_2\}\cdot 2H_2O]$ (**1**) which forms 3D supramolecular framework. It shows emission in the red region upon excitation at 400 nm with λ_{max}=585 nm. An efficient energy transfer process takes place in **1** from anthracene to anthracene:bpz exciplex. Further, this complex can be used for ratiometric sensing of Al^{3+} through quenching of exciplex emission (λ_{max}=585 nm) and appearance of new emission peak in the blue region with maxima centered at 460 nm upon addition of Al^{3+} to **1** dispersed in methanol. This change was observed for a very low concentration of Al^{3+} (10 nM). The probable mechanism of Al^{3+} detection can be attributed to the disruption of tetramer packing (exciplex).

5.5 References

1 (a) S. Goswami, A. Manna, S. Paul, A. K. Das, K. Aich and P. K. Nandi, *Chem. Commun.*, 2013, **49**, 2912; (b) H. Zhang, P. Wang, Y. Yang and H. Sun, *Chem. Commun.*, 2012, **48**, 10672; (c) M. Suresh, S. Mishra, S. K. Mishra, E. Suresh, A. K. Mandal, A. Shrivastav and A. Das, *Org. Lett.*, 2009, **11**, 2740.

2 (a) H. S. Jung, M. Park, D. Y. Han, E. Kim, C. Lee, S. Ham and J. S. Kim, *Org. Lett.*, 2009, **11**, 3378; (b) S. Ast, P. J. Rutledge and M. H. Todd, *Eur. J. Inorg. Chem.*, 2012, 5611.

3 (a) P. T. Srinivasan, T. Viraraghavan and K. S. Subramanian, *Water SA*, 1999, **25**, 47; (b) I. S. Parkinson, M. K. Ward and D. N. S. Kerr, *J Clin Pathol*, 1981, **34**, 1285; (c) A. Campbell, *Nephrol Dial Transplant*, 2002, **17**, 17.

4 (a) D. Maity and T. Govindaraju, *Chem. Commun*., 2010, **46**, 4499; (b) D. Maity and T. Govindaraju, *Chem. Commun.*, 2012, **48**, 1039.

5 (a) J. Zhou, W. Shi, N. Xu and P. Cheng, *Inorg. Chem*., 2013, **52**, 8082; (b) X. Zhou, L. Li, H. Li, A. Li, T. Yanga and W. Huang, *Dalton Trans*., 2013, **42**, 12403; (c) Z. Chen, Y. Sun, L. Zhang, D. Sun, F. Liu, Q. Meng, R. Wang and D. Sun, *Chem. Commun.*, 2013, **49**, 11557.

6 (a) W. Xuan, R. Pan, Y. Cao, K. Liub and W. Wang, *Chem. Commun.*, 2012, **48**, 10669; (b) K. Jayaramulu, R. P. Narayanan, S. J. George and T. K. Maji, *Inorg. Chem*., 2012, **51**, 10089.

7 SMART (V 5.628), SAINT (V 6.45a), XPREP, SHELXTL; Bruker AXS Inc. Madison, Wisconsin, USA, 2004.

8 G. M. Sheldrick, Siemens Area Detector Absorption Correction Program, University of Göttingen, Göttingen, Germany, 1994.

9 A. Altomare, G. Cascarano, C. Giacovazzo, A. Gualaradi, *J. Appl. Cryst*., 1993, **26**, 343

10 G. M. Sheldrick, SHELXL-97, Program for Crystal Structure Solution and Refinement; University of Göttingen, Göttingen, Germany, 1997

11 A. L. Spek, *J. Appl. Cryst*., 2003, **36**, 7.

12 L. J. Farrugia, WinGX–A Windows Program for Crystal Structure Analysis, *J. Appl.Crystallogr*., 1999, **32**, 837.